The effects of thermal radiation on supersonic flow

C.A.N. Steijger

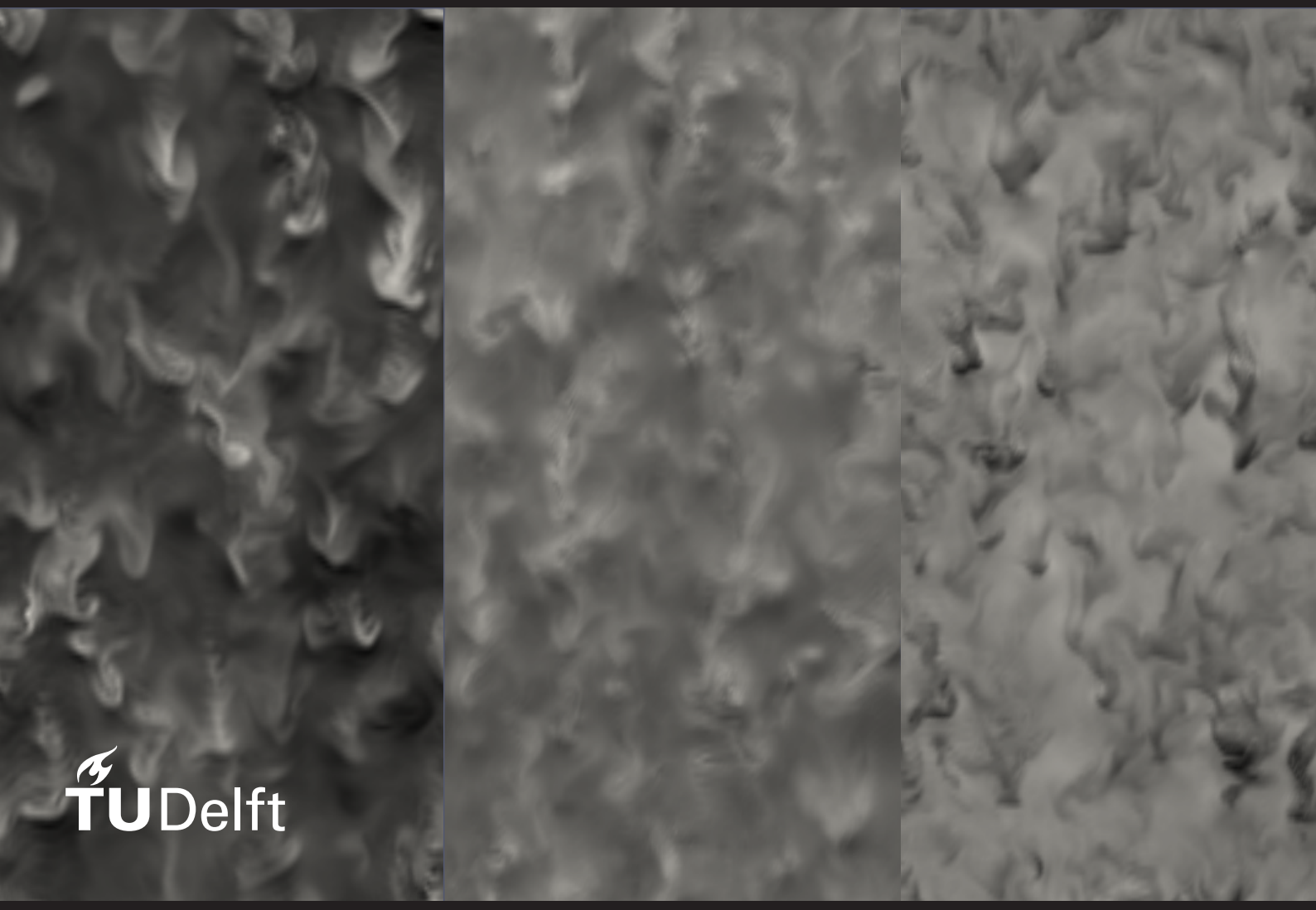

TU Delft

The effects of thermal radiation on supersonic flow

by

C.A.N. Steijger

To obtain the degree of Master of Science
at the Delft University of Technology,
to be defended publicly on Friday, November 6, 2020.

Student number:	4399153	
Project duration:	September, 2019 – November, 2020	
Thesis supervisors:	Dr. Ir. R. Pecnik,	TU Delft
	Ir. S. Silvestri,	TU Delft

An electronic version of this thesis is available at `http://repository.tudelft.nl/`.

TU Delft

Preface

This report is the result of my master Mechanical Engineering, Energy Flow and Process at the TU Delft. Here I spend my time learning subjects such as fluid dynamics and numerics, which I later applied for my thesis.

I want to thank Ir. Simone Silvestri for his effort in supporting me during my thesis. He helped me tremendously in getting familiar with the field of thermal radiation, as well as providing knowledge regarding DNS simulations.

In addition I would like to thank Dr. Ir. Rene Pecnik for his time supervising me, as well as his advice at critical points in my thesis.

I would like to thank the friends I made during my master program and without whom this experience would have been a lot less fun. In particular I would like to thank Jeroen, Jeroen, Bram, and Jesse with whom I spent many hours working on campus.

C.A.N. Steijger
Delft, November 2020

Abstract

Heat transfer via thermal radiation is a common occurrence in industry; be it in flue gas, boilers, reactors, or in supersonic combustor such as in a scramjet propulsion. Numerous studies have been done regarding the phenomena interacting with thermal radiation in different types of turbulent flows.
For compressible flows the effect of thermal radiation on the turbulent field via Turbulence Radiation Interaction (TRI) has been research to a lesser degree than for incompressible flows. Therefore, a more in-depth study on the impact of optical thickness in compressible flows should help create a better understanding regarding this.

This study consists of an investigation into the effect of thermal radiation in a non-reacting supersonic channel flow where the optical thickness of the fluid is changed. The fluid dynamics is simulated using a Direct Numerical Simulation (DNS) code for compressible turbulence and for the thermal radiation a grey-gas Finite Volume Method is used. A fictitious fluid is used with two different Planck numbers ($Pl = 0.1, 0.01$). Furthermore, for cases with $Pl = 0.01$ the constant absorption coefficient is varied between $\kappa = 1, 5, 10$.
The effects of thermal radiation on the temperature and density fields are discussed. Changing the optical thickness via the absorption coefficient shows a strong change in the behaviour of the fluctuating fields. Compressibility is shown to be affected by thermal radiations, where a stronger thermal radiation characterized by a high optical thickness and low Pl number show characteristics of an incompressible flow while being supersonic.
A model to determine the fluctuating incident radiation developed for high optical thickness incompressible flows is applied to this study as-is to investigate if the model is suited. It is shown that the assumptions made for the model, especially regarding thermal structures size, do not hold for compressible fluids and a different approach is needed.

Acronyms

cNSE	Compressible Navier-Stokes equations
DNS	Direct Numerical Simulation
EM wave	Electromagnetic wave
FANS	Favre averaged Navier-Stokes
FV	Finite Volume
LES	Large Eddy Simulation
LHS	Left-hand side
MCM	Monte Carlo Method
RANS	Reynolds averaged Navier-Stokes
RHS	Right-hand side
RTE	Radiative Transport Equation
TRI	Turbulence Radiation Interaction

Glossary

a	Speed of sound
c	Local speed of light
C_p	Thermal capacity at constant pressure
e	Internal energy
E	Emission
E_b	Black body emission
e_0	Total energy
G	Incident radiation
h	Enthalpy
I	Radiative intensity
I_b	Radiative intensity of a black body
$I_{b,\lambda}$	Spectral radiative intensity of a black body
I_λ	Spectral radiative intensity
p	Pressure
P_R	Radiative power
q	Heat flux
q_{cd}	Conductive heat flux
q_r	Radiative flux
S	Distance along given path length
T	Temperature

t	Time
u	Velocity component
u_τ	Wall friction velocity
V	Volume

Greek Symbols

β	Compressibility
κ	Absorption coefficient
κ_t	Thermal conductivity
λ	Wavelength
μ	Dynamic viscosity
ν	Kinematic viscosity
Φ_λ	Scattering phase function
Π	Pressure-strain coupling
ρ	Density
$\sigma_{\mathsf{s},\lambda}$	Scattering coefficient
τ	Viscous stress
ζ	Optical thickness

Non-dimensional Groups

Ec	Eckert number: $\frac{u^2}{C_p \Delta T}$
Ma	Mach number: $\frac{u}{a}$
Pl	Planck number: $\frac{\kappa_t T \delta}{\sigma T^4}$
Pr	Prandtl number: $\frac{\mu C_p}{\kappa_t}$
Ra	Radiation number: $\frac{\sigma T^4}{\rho u_b^3}$
Re	Reynold number: $\frac{\rho u \cdot L}{\mu}$
$Re_\tau^\star$	Semi local friction Reynold number: $\frac{\rho u_\tau^\star \cdot L}{\mu}$
Re_τ	Friction Reynold number: $\frac{\rho_w u_\tau \cdot L}{\mu_w}$

Constant variables

R	Universal gas constant, $8.3144 \frac{J}{K \cdot mol}$
σ	Stefan-Boltzmann constant, $5.670374e-8 \frac{J}{m^2 s K^4}$

Contents

Introduction

Motivation

Thermal radiation is commonly occurring in industry. Be it in flue gas, boilers, reactors, or in high altitude flight. The effects of thermal radiation on these processes have been investigated in the past both experimentally as well as numerically. It has been shown in, for example, reactive flows such as flames, that the interaction between thermal radiation and turbulence needs to be taken into account when accurate results are needed [2]. The previously mentioned supersonic flow for high altitude aviation is shown to be affected by thermal radiation [7]. The combination of thermal radiation in a supersonic flow is also found in scramjet propulsion or re-entry vehicles where accurate results are needed to prevent failure of the device.

Silvestri et al. [26] showed in his work that the optical thickness, or how much of a ray is absorbed over a given distance, has a large influence on the how the thermal radiation interacts with a turbulent flow field. While the works of Ghosh et al. [7] combines supersonic flow with thermal radiation, this was done for an optically thin flow. A study for higher optical thicknesses for supersonic flow has not yet been performed.

Studying thermal radiation can be difficult and computationally expensive. Computational methods of various degrees of accuracy and computational cost exist to approximate or simulate the effects of thermal radiation. To decrease the computational cost a situation can be approximated by a model to reduce the complexity of the problem. In his work Silvestri et al. [27] proposses a model suited for optically thick incompressible flows in order to approximate the more expensive radiative quantities.

Thesis scope

Optically thick flows have been analysed for incompressible framework, as well as for optically thin properties in compressible turbulence. In this research a lesser investigated combination is discussed; optically thick compressible flow. This is done to investigate if phenomena found in the previously mentioned situations still hold.
Furthermore, it is assessed if a model developed for approximating fluctuating radiative quantities in optically thick incompressible flow can be applied without modification to a compressible flow with a comparable optical thickness.

Thesis outline

Chapter 1 and 2 give an introduction to compressible turbulence, thermal radiation, and the interaction between the two phenomena, as well as governing equations to describe fluid and thermal radiation.

Chapter 3 describes the methodology used to investigate the effects. For both the fluid and radiation model the model validation is discussed. The differences between the cases, mainly absorption coefficient and Planck number, are briefly discussed.

The results for the different cases are compared and discussed in chapter 4. Special attention is given to the effect of thermal radiation on compressibility effects. Lastly a model is discussed that is used to determine fluctuating radiation quantities in incompressible turbulence.

A conclusion is presented in chapter 5, and recommendations are given for further investigation.

1

Theoretical background

1.1. Turbulence

A flow can be considered to be in a laminar state if it is smooth, ordered, and regular, if this is not the case it is in a turbulent state. Shear layers and differences in density can form small perturbations in the flow that are damped out by viscous forces. As the perturbations grow, a point is reached for which the viscous forces are no longer large enough to damp these perturbations and the flow transitions into a chaotic state. A method to quantify the state of a flow is by determining its Reynolds number (Re), which is defined as the ratio of inertial forces over viscous forces by:

$$Re = \frac{\rho u \mathcal{L}}{\mu}\,, \tag{1.1}$$

with $\mathcal{L}$ being a length scale, u a velocity scale, and ρ and μ are density and dynamic viscosity respectively. The value of the Reynolds number for which this transition occurs is dependent on properties of the flow and fluid, as well as the geometry of the system in which the flow resides.

Due to the chaotic nature of turbulence it is sometimes necessary to average either over space and/or time in order to investigate the characteristics of the flow through statistical quantities. A common averaging procedure is ensemble averaging which relies on using data from uncorrelated measurements of the same experiment, or multiple experiments under similar conditions. This will lead to a data-set containing measurements that are different in principle. The ensemble averages is mathematically expressed as:

$$\overline{u} = \lim_{N\to\infty} \frac{1}{N} \sum_{\alpha=1}^{N} u_\alpha\,, \tag{1.2}$$

where the index α indicates the index of the measurement in the data-set [17, ch 5].

As stated before, one of the characteristics of turbulence is its fluctuating nature. Using the averaged quantities it becomes possible to calculate a fluctuating quantity by subtracting the average from the total quantity. Two methods are mainly used to calculate fluctuating components of a flow: Reynolds averaging, and Favre averaging, the latter is used for compressible fluids when averaging quantities such as velocity or enthalpy.

The first one, Reynolds averaging, is performed by decomposing the flow into an averaged component and a fluctuating component,

$$p = \underbrace{\overline{p}}_{\text{averaged}} + \underbrace{p'}_{\text{flucuating}}\,, \tag{1.3}$$

in which p is the pressure, $\bar{\cdot}$ the average part, and $\cdot'$ the fluctuating part. The second method used, Favre averaging, is in principle similar to Reynolds averaging, where a quantity is decomposed into an averaged part and a fluctuating part. The main difference lays in averaging with density weighted

quantities:

$$u = \widetilde{u} + u'' = \underbrace{\frac{\overline{\rho u}}{\overline{\rho}}}_{\text{averaged}} + \underbrace{u' - \frac{\overline{\rho' u'}}{\overline{\rho}}}_{\text{fluctuating}}, \tag{1.4}$$

in which $\widetilde{.}$ is a Favre average, and $.''$ is a Favre fluctuation.

Turbulent flow is characterised by vortex-like structures. These vortex-like structures are referred in literature as eddies. Eddies take on different length scales meaning that throughout the flow different sizes of structures can be found. Within a turbulent flow a transfer of energy exists in which energy is transferred from larger length scale eddies into smaller length scale. This occurs when larger eddies breakup into multiple smaller eddies. This cascade process describes how larger eddies break up into smaller eddies, until the length scale of the eddy reaches the Kolmogorov length which is the smallest length scale in a turbulent flow. This length scale is defined as the length scale for which the Reynolds number equals 1 [19, ch 6]. At this length scale viscosity dissipates all kinetic energy into heat.

1.1.1. Compressible turbulence

Compressibility is thermodynamically defined as the change in volume by pressure. This can most notability be found when discussing gasses as liquids are considered incompressible. Thermodynamic compressibility is defined as:

$$\beta = -\frac{1}{V}\left(\frac{\partial V}{\partial p}\right). \tag{1.5}$$

The distinction between compressible and incompressible is determined such that β approaches 0 for incompressible fluids. This also means that almost no liquids are truly incompressible, but this is only relevant in extreme cases. A distinction in naming convention can be made between different forms of compression. Compressibility is when changes in volume can be directly associated with pressure such as defined in equation (1.5), while changes in volume due to heat transfer are called variable inertia. In a compressible turbulent flows, fluid properties such as density, and thermophysical properties such as viscosity or specific heat vary due to changes in temperature and pressure [13]. Coleman et al. [4] and Huang et al. [10] both discussed how compressibility effect in supersonic compressible flows are generated from mean property variations.

In the study by Foysi et al. [6] the compressibility effects and the mean property variation was linked to changes in the pressure-strain correlation. The pressure-strain correlation is part of the mathematical description of compressibility and is defined as:

$$\Pi_{ij} = \overline{p'(\partial_{x_j} u_i'' + \partial_{x_i} u_j'')/2}\,. \tag{1.6}$$

In this equation p' is the pressure fluctuation and the second term is the strain rate tensor of the Favre fluctuating velocity field. He found that changes to the pressure-strain correlation are not due to changes in the Reynolds number, but rather can be attributed to the difference between the mean density $\overline{\rho}$, and the density at the wall ρ_w, where a reduction in $\overline{\rho}$ causes a reduction in Π_{ij}.

1.1.2. Turbulence modelling

To understand the behaviour of a turbulent flow, two options exist for investigation: an experimental approach and a numerical approach. When focussing on the numerical approach three main methods can be distinguished: Reynolds averaged Navier-Stokes (RANS), Large Eddy Simulation (LES), and Direct Numerical Simulation (DNS). RANS, as the name implies, involves solving the Reynolds averaged equations (for more details see chapter 2), which are solved to describe the flow. This makes the use of RANS less computational expensive at the cost of the loss of detail in the microstructure of the flow. This method is often implemented in industry due to cost considerations in both time and capital.

DNS instead consists of solving the full Navier-Stokes equations, which enables capturing all the length scales of the flow. DNS requires a fine grid as all structure sizes, down to the Kolmogorov length scale, need to be simulated. This makes DNS computationally expensive and is therefore mostly used in academic or fundamental research. LES fits in between RANS and DNS as it utilizes a mix of eddy simulation and modelling. The small length scales of the flow are filtered out and replaced by a model to dissipate the energy of the large scale. Other methods for simulating fluid dynamics exist, such as the Finite Element method, and the Lattice Boltzmann method.

1.2. Thermal radiation

Radiation is one of the three modes of thermal energy transfer defined in literature. Unlike convection or conduction it does not require contact between transfer media. Due to this the length scale over which energy transfer via thermal radiation can occur is much larger than the other modes [8, ch 1].

Thermal radiation is transferred by electromagnetic waves which can be emitted, absorbed, and scattered. Emission is the collective term for all energy transferred away from a given control volume or surface. The emitted waves travel along a single direction with a specific wavelength until it interacts with either a fluid or solid. These interactions are either absorption or scattering. This is schematically shown in figure 1.1 by the labels A till D in which A denotes emission, B absorption, C out-scattering, and D in-scattering.

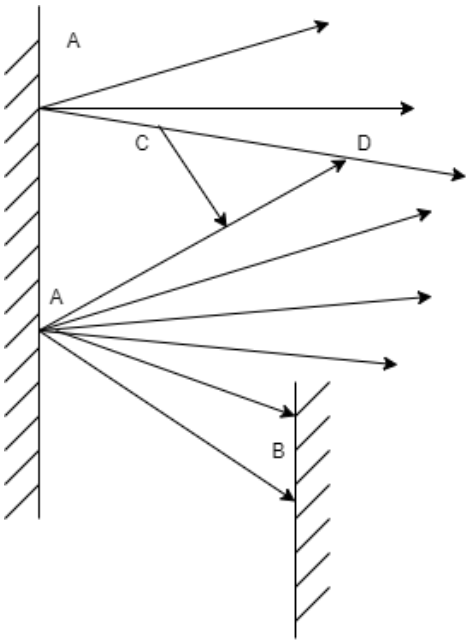

Figure 1.1: A visualization of emission (A), absorption (B), out-scattering(C), and in-scattering (D).

The amount of interactions in the medium can be expressed by the optical thickness which is defined as,

$$\zeta_\lambda = \int_0^S (\sigma_{\mathrm{s},\lambda} + \kappa_\lambda)\, dS' \,, \tag{1.7}$$

where ζ is the optical thickness, $\sigma_{\mathrm{s},\lambda}$ is the scattering coefficient, κ is the absorption coefficient, and S is the path length of the ray. The subscript $_\lambda$ refers to different wavelengths, as optical thickness is wavelength dependent. From this point $_\lambda$ will only be included when emphasis is placed on wavelength dependency. The optical thickness depends on the local properties of the medium and can be influenced by the density, where a higher density can be expected to have a higher optical thickness. When a medium has a optical thickness of $\zeta \ll 1$ it is called optically thin, and when it is $\zeta \gg 1$ it is called optically thick [8, p 37].

1.2.1. Radiation modelling

Simulating thermal radiation is computationally expensive due to the length scale over which radiation occurs. Due to this, many different methods exist with varying levels of accuracy and computational cost optimized for different applications. The two main classes of methods which are mainly discussed in literature are differential and integral methods. From the class of differential methods, three models are more commonly used: spherical harmonics (P_N), discrete ordinates (S_N), and Finite Volume (FV). With regards to the integration methods, the Monte Carlo Method (MCM) is commonly used nowadays.

Spherical harmonics write the Radiative Transport Equation (RTE) (explained in more detail in chapter 2.2) as a series of harmonic functions. When the number of harmonic functions approaches

infinite, the solution would be exact. In practice however only the series 0 till 3 are used as it becomes increasingly more difficult to solve the problem [9, ch 12]. For one-dimensional problems a so called P_1 approximation is used, in which the series up to and including 1 are used as indicated by the 1. For more complex problems P_3 approximation is used, as it was found that uneven series approximate the problem more accurately. A drawback for the method is its performance in optically thin media where it was found to be less accurate [5].

The discrete ordinates model describes thermal radiation by a set of partial differential equations for a number of angular subdomains or ordinate directions. The partial differential equations that are used to sum over the ordinate directions intensity are weighted. These weights must obey a set of rules but otherwise are free to choose. The discrete ordinates method does not conserve radiative energy and when low order variants of the methods are implemented shows discontinuities in temperature and radiative flux. The method is however relatively simple to implement.

The finite volume method works by applying the differential form of the RTE to a mesh scheme similar to those used with the discrete ordinates method. The finite volume method however, does not utilize weights to model the intensity. The main advantages over the discrete ordinates method are the local energy conservation and being able to cope with anisotropic scattering.

MCM works by ray tracing a large amount of photons until the ray is fully absorbed, and utilising the statistics of these results to simulate the radiative field. Each beam has a randomly selected azimuthal, and polar angle in addition to a random wavelength. This method allows for the usage of narrow-band spectra for any optical thickness, with high accuracy. This accuracy does come with a high computational expense. These costs can be lowered by parallelizing the ray tracing onto GPUs as shown by Silvestri and Pecnik [25], where a simulation speedup of $570\times$ was achieved on a 96^3 grid.

1.3. Turbulence-radiation interaction

The interaction of radiation and a turbulent flow has been researched extensively as its interaction can be of importance in environments such as combustion, chemical reactions, or in describing how the atmosphere is influenced by solar radiation. The coupling between thermal radiation and turbulence is highly non-linear in the relation between temperature and radiative quantity fluctuations [31]. Turbulence Radiation Interaction (TRI) can be split into two categories: The influence of the turbulent flow upon the radiation field and vice versa[7]. The first pathway has been shown to be of importance mainly to reacting flows, or for flows with a high optical thickness [3].

This part of TRI also has the most literature available, with one of the main contributors the research field on combustion. Wu et al. [31] investigated TRI in the combustion of a premixed grey gas using DNS with an MCM, and looked at the effect of optical thickness on the TRI in a thin flame. It was found that even in the case of a very thin optical thickness the emission part of TRI is not negligible. In the study by Tessé et al. [28] TRI has been shown to increases radiative power by 31% in a turbulent sooty flame. Within this study it was also concluded that the radiative heat transfer is sensitive to the integral length scale of the turbulent field. This sensitivity was said to be mostly due to absorption by turbulent structures large enough to not be considered optically thin. This is shown schematically in figure 1.2 where internal radiation transfer in turbulent structures is shown. It is also shown schematically that this is direction dependent, as structures are rarely uniform in all directions.

The second part of TRI has been researched less although in recent years this has been increasing. Zhang et al. [32] researched the effects of gas-gas and gas-wall effects on the flow under different conditions using a DNS with a MCM for low-Mach number flows. He showed that the temperature profile trough the channel does not match the expected log-law and a different scaling law is to be applied. In the research of Silvestri et al. [26] an incompressible turbulent flow was used with DNS in combination with a grey-gas model to investigate the effect of optical thickness on a channel flow. It was found that as the flow becomes more optical thick, the energy in the temperature spectra is moved away from the walls and to smaller wavenumbers, which is associated with re-absorption within larger structures. This same effect was shown in a different study by Silvestri et al. [27] when a DNS MCM simulation was used to investigate non-grey gasses in high optical thickness flows. This study proposes a way to compare TRI between non-grey and grey gas using an effective optical thickness for the non-grey gas, which is based on a turbulence based mean absorption coefficient. This is necessary as non-grey gas can have a large range for its absorption spectra.

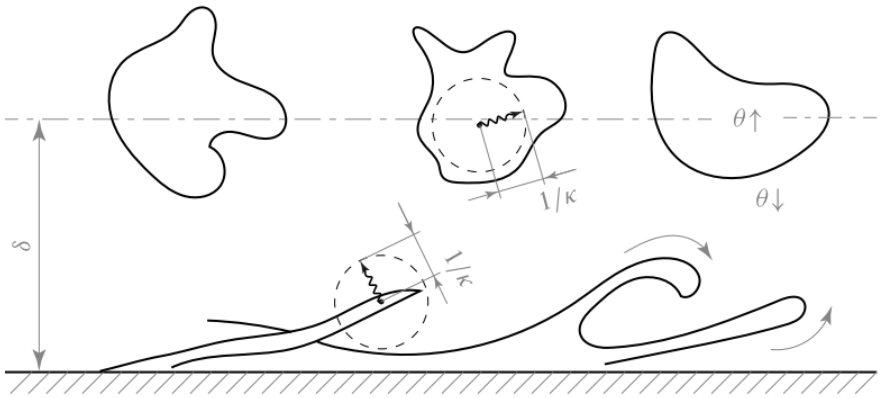

Figure 1.2: A visualisation on the effect of structure length scale to the local absorption for high optical thickness. As structures increase is size, the amount of self-radiation increases, figure adopted from the works of Silvestri et al. [26].

The work of Ghosh et al. [7] investigates TRI in supersonic channel flows for low optical thicknesses using an LES with a grey-gas model. Results found by Ghosh show similarities with studies done on incompressible fluids, being a lower mean temperature profile and temperature fluctuations. Furthermore it was shown that thermal radiation lowers the compressibility. This decrease in compressibility has been explained by the decrease in streamwise Reynolds stress due to increase in mean density. The reduction in streamwise Reynolds stress is caused by a reduction in streamwise pressure-strain correlation as shown by Foysi et al. [6].

2

Governing Equations

2.1. Governing equations and budgets

The Compressible Navier-Stokes equations (cNSE) consist of the continuity, momentum, and energy conservation equations and are given in equations (2.1) - (2.3),

$$\frac{\partial \rho}{\partial t} + \frac{\partial \rho u_j}{\partial x_j} = 0\,, \tag{2.1}$$

$$\frac{\partial \rho u_i}{\partial t} + \frac{\partial \rho u_i u_j}{\partial x_j} = -\frac{\partial p}{\partial x_i} + \frac{\partial \tau_{ij}}{\partial x_j} + \rho f_i\,, \tag{2.2}$$

$$\frac{\partial \rho e_0}{\partial t} + \frac{\partial \rho e_0 u_j}{\partial x_j} = -\frac{\partial u_j p}{\partial x_j} + \frac{\partial u_i \tau_{ij}}{\partial x_j} + \frac{\partial q_j}{\partial x_j} + \rho u_i f_i\,. \tag{2.3}$$

The shear stress τ and the heat flux in the cNSE are defined as,

$$\tau_{ij} = \mu\left[\left(\frac{\partial u_i}{\partial x_j} + \frac{\partial u_j}{\partial x_i}\right) + \frac{2}{3}\delta_{ij}\frac{\partial u_k}{\partial x_k}\right]\,, \tag{2.4}$$

$$q_j = -\kappa_t \frac{\partial T}{\partial x_j}\,, \tag{2.5}$$

for which μ is viscosity and κ_t is thermal conductivity. The total energy e_0 in equation (2.3) can be written as $\rho e_0 = \rho e + \frac{1}{2}\rho u_i^2$, where ρe is the internal energy of the flow, and $\frac{1}{2}\rho u_i^2$ the kinetic energy. It is possible to rewrite equation (2.3) in terms of enthalpy. Doing so allows the material derivative of pressure to be neglected in this equation. This is because in an open channel the thermodynamic pressure is set by atmospheric conditions and therefore does not change over time or distance [16]. To rewrite the equation the relation between enthalpy and total energy,

$$\rho e_0 = \rho h - p + \frac{1}{2}\rho u_i^2\,, \tag{2.6}$$

is substituted into equation (2.3) as shown in equation (2.7).

$$\frac{\partial \rho h}{\partial t} + \frac{\partial \rho h u_j}{\partial x_j} = +\frac{\partial u_i \tau_{ij}}{\partial x_j} + \frac{\partial q_i}{\partial x_j} + \rho u_i f_i\,. \tag{2.7}$$

2.1.1. Closure models for thermodynamic quantities

In order to close the cNSE a relation between density, temperature, and pressure is needed. This can be done using an equation of state such as the ideal gas law,

$$p = \rho n R T \,. \tag{2.8}$$

In this equation R is the gas constant, and n is the amount of gas in mol number. More complex equations of state exist to describe this relation for more complex situations. Examples are Van der Waals, Redlich-Kwong, and Peng-Robinson equation of state, all of which are cubic relations and are able to describe the state of the gas more closely in regions of high temperature or near supercritical state.

The transport properties viscosity and thermal conductivity are a function of local density and temperature [29]. These properties are usually modelled using a power law [4], Sutherland's law [15] or calculated based on experimental data [7][23].

2.2. Radiative transfer equation

The transfer of energy by thermal radiation is described by the RTE. This equation relates the change in radiative intensity along a path by emission, absorption, out-scatter, and in-scatter. The RTE is defined as:

$$\frac{1}{c}\frac{\partial I_\lambda}{\partial t} + S_j \frac{\partial I_\lambda}{\partial x_j} = \underbrace{\kappa_\lambda I_{b,\lambda}}_{\text{emission}} - \underbrace{\kappa_\lambda I_\lambda}_{\text{absorption}} - \underbrace{\sigma_{\mathsf{s},\lambda} I_\lambda}_{\text{out-scatter}} + \underbrace{\frac{1}{4\pi}\int_{\Omega_i=4\pi} \sigma_{\mathsf{s},\lambda} I_\lambda \Phi_\lambda \mathsf{d}\Omega_i}_{\text{in-scatter}} \,. \tag{2.9}$$

In this equation I is the radiative intensity, κ_λ is the absorption coefficient, and $\sigma_{\mathsf{s},\lambda}$ is the scattering coefficient along the path. The subscripts $_\lambda$ and $_b$ indicate spectral dependency and blackbody respectively. The scattering phase function Φ_λ used in the equation describes the solid angle dependency of any incoming scattered energy. The time dependent component of the left-hand side is only considered when high speed events occur, and as such is often negligible due to the speed of light in the denominator. Equation (2.9) can be simplified by two approximations: the medium being a grey gas, and the medium being purely emitting-absorbing. For the grey gas approximation it is assumed that radiative properties (absorption coefficient, scattering coefficient, and phase function) do not depend on wavelength. Doing so allows for the integration of the emission and absorption term in equation (2.9) which results in,

$$S_j \frac{\partial I}{\partial x_j} = \kappa_p I_b - \kappa_G I - \sigma_s I + \frac{\sigma_s}{4\pi}\int_{4\pi} I d\Omega \,. \tag{2.10}$$

In this equation κ_p, κ_G, and σ_s are the Planck-mean absorption coefficient, incident mean absorption coefficient, and the mean scattering coefficient respectively. The second approximation assumes that in the medium $\sigma_{\mathsf{s},\lambda} = 0$ holds. Doing so allows for the evaluation of the two absorption coefficients. As was done by Sakurai et al. [22] it is possible to state $\kappa_p \approx \kappa_G$ even when these coefficients do not describe the same quantities. By assuming the medium is isolated and with boundary temperatures close to that of the medium, it becomes possible to neglect the subscripts for the absorption coefficient. This gives the simplified total RTE,

$$S_j \frac{\partial I}{\partial x_j} = \kappa I_b - \kappa I \,. \tag{2.11}$$

Radiative flux can be determined by integrating I over all directions. Furthermore, the divergence of the radiative heat flux describes the local volumetric heat source or sink by radiative transfer. The term $\nabla I(\hat{s})\hat{s}$ from equation(2.11) is substituted to obtain equation (2.12):

$$\nabla \cdot q_r = \nabla \cdot \int_{4\pi} I(\hat{s})\hat{s} d\Omega \,. \tag{2.12}$$

Using the relation $I_b = \frac{\sigma}{\pi}T^4$, the equation can be rewritten into,

$$\nabla \cdot q_r = \underbrace{4\kappa\sigma T^4}_{\text{emission}} - \underbrace{\kappa \int_{4\pi} I d\Omega}_{\text{incident radiation}} \,. \tag{2.13}$$

The first term on the Right-hand side (RHS) is the blackbody emission integrated over all directions. The second term is the incident radiation, and is usually denoted as G.

2.3. Non dimensionalization

To have a generalised and comparable solution, it is useful to solve for non-dimensional variables. The quantities used in these equations are non-dimensionalised as,

$$u = \frac{u^*}{u_r^*}\,, \qquad x_i = \frac{x_i^*}{H^*}\,, \qquad t = \frac{t^* u_r^*}{H^*}\,, \qquad p = \frac{p^*}{u_r^* \rho_r^*}\,,$$

$$\rho = \frac{\rho^*}{\rho_r^*}\,, \qquad T = \frac{T^*}{T_r^*}\,, \qquad \zeta = \kappa^* \delta^*\,, \qquad I = I^* \frac{\pi}{\sigma T^{4,*}}\,.$$

In these relations, the subscript $_r$ denotes a reference value such as a value taken at the wall, and the superscript * denotes a dimensional value. The non-dimensional numbers Re, Pr, Pl, and Ec are written in dimensional values as:

$$Re = \frac{\rho_r^* u_r^* H^*}{\mu_r^*}\,, \qquad Pr = \frac{\mu_r^* {C_p}^*}{\kappa_{t_r}^*}\,,$$
$$M_{ps}^2 = Ec = \frac{{u_r^*}^2}{{C_p}^* T_r^*}\,, \qquad Pl = \frac{\lambda_r^*}{\sigma T_r^* H^*}\,.$$

Substituting non-dimensional quantities into equations (2.1)-(2.3) the non-dimensional Navier-Stokes equations are obtained. The conservation equations are shown in equations (2.14), with shear stress and heat flux shown in equations (2.15) and (2.16):

$$\begin{cases} \dfrac{\partial \rho^*}{\partial t^*} + \dfrac{\partial \rho^* u_j^*}{\partial x_j^*} = 0 \\ \dfrac{\partial \rho^* u_j^*}{\partial t^*} + \dfrac{\partial \rho^* u_i^* u_j^* + p^* \delta_{ij} - \tau_{ij}^*}{\partial x_j^*} = \rho^* f_i^* \\ \dfrac{\partial \rho {e_0}^*}{\partial t^*} + \dfrac{\partial \rho^* {e_0}^* u_j^* + p^* u_j^* + q_j^* - u_i^* \tau_{ij}^*}{\partial x_j^*} = \rho^* u_j^* f_j^*\,, \end{cases} \tag{2.14}$$

$$\tau_{ij}^* = \mu^* \left[\left(\frac{\partial u_i^*}{\partial x_j^*} + \frac{\partial u_j^*}{\partial x_i^*} \right) - \frac{2}{3} \delta_{ij} \frac{\partial u_k^*}{\partial x_k^*} \right]\,, \tag{2.15}$$

$$q^* = -\kappa_t \frac{\partial T^*}{\partial x_j^*}\,. \tag{2.16}$$

In equations (2.1)-(2.3) the subscript $_w$ indicates a reference value taken at the wall, and a subscript $_b$ indicates a reference value taken in the bulk of the flow. If the non-dimensional quantities are substituted into equation (2.14) the non-dimensional continuity equation is found.

$$\frac{\partial \rho^*}{\partial t^*} + \frac{\partial \rho^* u_j^*}{\partial x_j^*} = \frac{\partial \rho \rho_r^*}{\partial t \frac{H}{u_r^*}} + \frac{\partial \rho \rho_w^* u_j u_r^*}{\partial x_j H_r^*} = 0\,, \tag{2.17}$$

$$\frac{\rho_r^* u_r^*}{H_r^*} \left(\frac{\partial \rho}{\partial t} + \frac{\partial \rho u_j}{\partial x_j} \right) = 0\,. \tag{2.18}$$

Similarly the momentum equation can be found by:

$$\begin{aligned} &\frac{\partial \rho^* u^*}{\partial t^*} \frac{\partial \rho^* u_j^* u_i^*}{\partial x_j^*} = -\frac{\partial p^*}{\partial x_j^*} + \mu^* \left[\frac{\partial^2 u^*}{\partial x_j^2 *} - \frac{2}{3} \delta_{ij} \frac{\partial^2 u^*}{\partial {x_k^*}^2} \right] + \rho f_i\,, \\ &\frac{\partial \rho \rho_w^* u {u_r^*}^2}{\partial t H^*} \frac{\partial \rho \rho_w^* u_j u_r^* u_i u_r^*}{\partial x_j H^*} = -\frac{\partial p \rho_w^* {u_r^*}^2}{\partial x_j H^*} + \mu \mu_w^* \left[\frac{\partial^2 u u_r^*}{\partial x_j^2 {H^*}^2} - \frac{2}{3} \delta_{ij} \frac{\partial^2 u u_r^*}{\partial x_k {H^*}^2} \right] + \rho \rho_w^* f_i \frac{u_r^*}{H^*}\,, \end{aligned} \tag{2.19}$$

$$\frac{\partial \rho u_i}{\partial t} + \frac{\partial \rho u_i u_j}{\partial x_j} = -\frac{\partial p}{\partial x_i} + \frac{1}{Re}\frac{\partial \tau_{ij}}{\partial x_j} + \rho f_i \,. \tag{2.20}$$

And the energy equation is found by:

$$\begin{aligned}
&\frac{\partial \rho^* {e_0}^*}{\partial t^*} + \frac{\partial \rho^* u_j^* {e_0}^*}{\partial x_j^*} = -\frac{\partial p^* u_j^*}{\partial x_j^*} + \frac{\partial u_j \tau_{ij}^*}{\partial x_j^*} - \frac{\partial q_j^*}{\partial x_j^*} + \rho^* u_j^* f^* \,, \\
&\frac{\partial \rho \rho_w^* e_0 u_r^{*3}}{\partial t H^*} + \frac{\partial \rho \rho_w^* u u_r^* e_0 u_r^{*2}}{\partial x_j H^*} = -\frac{\partial u_j u_r^* p \rho_w^* u_r^{*2}}{\partial x_j H^*} + \frac{\partial u_j u_r^* \tau_{ij} \frac{u_r^* \mu_w^*}{H^*}}{\partial x_j^*} - \kappa_t \kappa_{t_w}^* \frac{\partial^2 T T^*}{\partial x_j H^{*2}} + \rho \rho_w^* u u_w^* f_i \frac{u_r^*}{H^*} \,,
\end{aligned} \tag{2.21}$$

$$\frac{\partial \rho e_0}{\partial t} + \frac{\partial \rho e_0 u_j}{\partial x_j} = -\frac{\partial u_j p}{\partial x_j} + \frac{\partial u_i \tau_{ij}}{\partial x_j} - \frac{\kappa_t}{RePrEc}\frac{\partial q_j}{\partial x_j} + \rho u_i f_i \,. \tag{2.22}$$

In the non-dimensionalised conservation equations above, three terms can be seen to be different from the conservation equations as shown in equations (2.1) - (2.3):

Shear stress,

$$\tau_{ij} = \frac{\mu}{Re}\left[\left(\frac{\partial u_i}{\partial x_j} + \frac{\partial u_j}{\partial x_i}\right) + \frac{2}{3}\delta_{ij}\frac{\partial u_k}{\partial x_k}\right] \,, \tag{2.23}$$

thermal transfer by convection,

$$q_{cd} = -\frac{\kappa_t}{RePrEc}\frac{\partial T}{\partial x_j} \,, \tag{2.24}$$

and the thermal transfer by radiation,

$$\nabla \cdot q_r = \frac{1}{RePrEcPl}\left[4\zeta T^4 - \zeta \int_{4\pi} \frac{I}{\pi} d\Omega\right] \,. \tag{2.25}$$

The term $1/\left(RePrEcPl\right)$ found in the thermal transfer by radiation is the ratio $\sigma T^4 / \left(\left(\rho u_r^2\right) u_r\right)$. Based on the quantities in this relation it appears that it is related to the ratio of radiative heat transfer over the advection of kinetic energy in the fluid.

3

Methodology

3.1. Fluid model

A DNS is used to simulate and investigate the effect of thermal radiation on compressible supersonic flow. An in-house code, as developed by Sengupta [23], is used as a starting point from which a radiation model is to be added. As discussed in chapter 2, an equation of state is needed to close the cNSE. For this the ideal gas equation is used to simplify this part of the simulation. The coupling of viscosity and thermal conductivity is achieved by implementing Sutherland's law. The non-dimensional version of which is written as,

$$\phi = \phi_r \left(\frac{T}{T_w} \right)^{0.7} . \tag{3.1}$$

In equation (3.1) ϕ_r is substituted by $\mu = 1/Re$ or $\kappa_t = 1/(EcRePr)$ for viscosity or thermal conductivity respectively. The fluid used in the simulations is a fictitious ideal grey gas. The grid is chosen to be a 192 cubic mesh of lengths $4\pi\delta \times 2\delta \times 2\pi\delta$. The mesh is uniform in stream-, and span-wise direction, to allow the use of spectral method. The simulation domain is schematically visualised in figure 3.1. The code used by Sengupta [23] clipped spectral modes in order to minimize aliasing

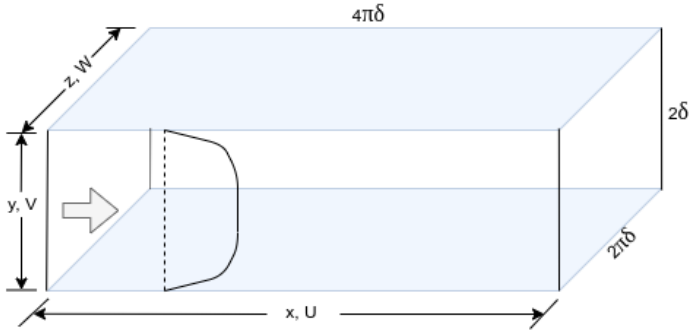

Figure 3.1: A visualization of the geometry used.

errors, which are introduced by taking derivatives of non-linear terms in the cNSE. A pseudo skew symmetric formulation, shown in equation (3.2), was used by Sengupta [23] in combination with the clipping of modes to reduce these errors. In this equation the term ϕ is velocity, enthalpy, or internal energy. This method was used for the advection terms in both momentum and energy conservation equation.

$$\frac{\partial \rho u_j \phi}{\partial x_j} = \frac{1}{2} \left(\frac{\partial \rho u_j \phi}{\partial x_j} + \rho u_j \frac{\partial \phi}{\partial x_j} + \phi \frac{\partial \rho u_j}{\partial x_j} \right) . \tag{3.2}$$

A method proposed by Kennedy and Gruber [11] and later improved upon by Pirozzoli [18] shows better results for flows with strong density variations, and one which does not require the mode clipping. For

this study a full skew symmetric formulation has been implemented as shown in equation (3.3).

$$\frac{\partial \rho u_j \phi}{\partial x_j} = \frac{1}{4}\left(\frac{\partial \rho u_j \phi}{\partial x_j} + \rho u_j \frac{\partial \phi}{\partial x_j} + \phi u_j \frac{\partial u}{\partial x_j} + \phi u_j \frac{\partial \rho}{\partial x_j} + \phi \frac{\partial \rho u_j}{\partial x_j} u_j \frac{\partial \rho \phi}{\partial x_j} + \rho \frac{\partial \phi u_j}{\partial x_j}\right). \tag{3.3}$$

In wall normal direction the mesh is stretched to increase resolution near the wall. This is done with a stretching factor (S_f) of 4 using equation (3.4) which is written for a collocated grid.

$$\begin{cases} x = \dfrac{i}{N_y} - 0.5, \text{ with } \{\, i \mid i \in \mathbb{N}, 1 \leq i \leq N_y \} \\ y_i = 1 + \dfrac{\tanh(S_f \cdot x)}{\tanh(S_f \cdot 0.5)} \\ dy_{i,c} = \dfrac{0.5 \cosh(S_f \cdot x)^2}{\tanh(0.5 \cdot S_f)}. \end{cases} \tag{3.4}$$

In equation (3.4), the index i can be offset by 0.5 to obtain the staggered grid locations. In wall normal direction a 6th order compact finite difference method is applied, developed by Lele [14], which is used for both interpolation between cell-center and wall, and for determining derivatives. As the 6th order compact derivative is meant for uniform meshes, a correction factor as shown in equation (3.5) is used. This still leaves a numerical error depending on the size of the stretch in the mesh.

$$\frac{\partial \phi}{\partial y} = \frac{\partial \phi}{\partial i}\frac{\partial i}{\partial y} = \frac{1}{dy_{i,c}}\frac{\partial \phi}{\partial i}. \tag{3.5}$$

The parallelization API open_mpi is used together with the 2DECOMP&FFT library which slices the domain into suitable parts for a parallelized job. For temporal discretization a third order Runga Kutta is used.

3.1.1. Boundary conditions

Several boundary conditions are to be set in order for the simulation to work. In span and streamwise direction a periodic boundary condition is implemented. A body forcing term is used in streamwise direction to drive the flow. This forcing term is analogous to $(-1/\rho)\partial p/\partial x$ to ensure that $\int_y \rho u dy$ is conserved, as is done in [23]. The walls of the channel are isothermal, and have a no-slip boundary condition for which the 4th order compact finite difference method is used as discussed by Boersma [1], and Sengupta [23]. The wall temperature is set to be 500 K. The reason for choosing this temperature instead of setting the wall temperature to 1000 K as Ghosh et al. [7] is because a lower temperature is easier to reach and it can therefore be assumed to be more prominent in industry. The wall is assumed to be a black body, and is fully absorbing when a radiation model is used.

3.1.2. Fluid model validation

The model is validated using previous results from literature. The model is run for an ideal gas case without radiation, for Ma 1.5, $Re = 3000$, $Pr = 0.7$, such that the results are relatable to the data of Coleman et al. [4]. A set of 84 instantaneous recordings were used to average the results every 3000 time steps.

A comparison can be seen in figures 3.2a and 3.2b. In figure 3.2a the quantities compared agree with the reference case. Figure 3.2b shows a discrepancy for the streamwise Reynolds stresses. For the spanwise and wall normal direction, the Reynolds stresses match the reference data well. Streamwise direction shows a difference, but with the stress expected to be symmetric over the centre line of the channel, which could be a problem with the reference data. Overall the model gives the expected results when comparing with literature.

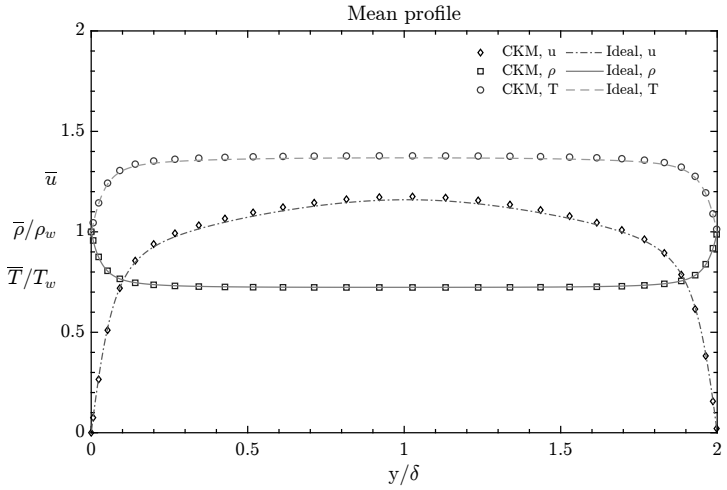

(a) Comparison between simulations from Coleman et al. [4], and present. Mean streamwise velocity, density, and temperature are compared.

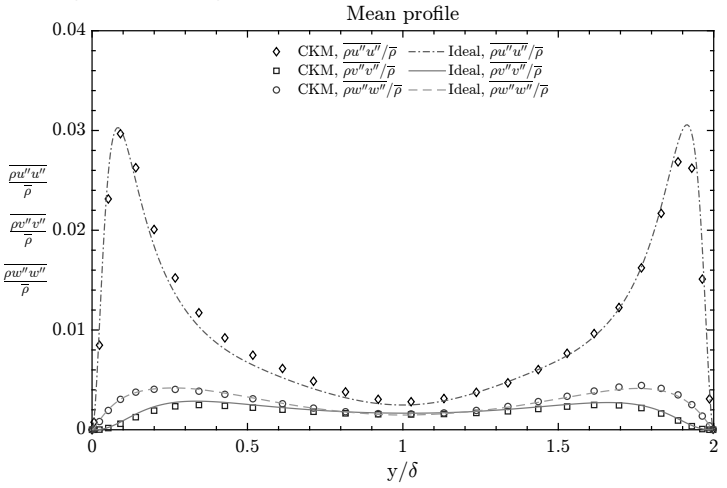

(b) Comparison between simulations from Coleman et al. [4], and present. Mean Favre averaged velocity quantities.

Figure 3.2: Comparison between simulations from Coleman et al. [4], and present.

3.2. Radiation model

The radiation model used in the study is a finite volume method using in-house code made by Silvestri et al. [26]. To include thermal radiation heat transfer into the energy equation the quantity $\partial_{x_j} q_r$ is added to the energy conservation equation. As discussed more extensively in chapter 2, the radiative heat flux is obtained via equation (3.6),

$$\frac{\partial q_r}{\partial x_j} = \zeta \left(E_b - G \right) = \zeta \left(4 I_b - \frac{1}{\pi} \int_{4\pi} I \mathrm{d}\Omega \right) . \tag{3.6}$$

In this equation ζ is the optical thickness, E_b is black body emission, G is the incident radiation, I, and I_b are radiative intensity, and radiative intensity of a black body respectively. Black body emission can be determined directly from the temperature field. It has been shown that for an effective calculation of G a finite volume method with additional grid refinements is needed.

3.2.1. Spacial discretization

A finite volume method is applied for modelling the thermal radiation due to the inherent conservation of energy of this method, and because of its relative ease of implementation compared to an MCM. To implement this, a local spherical mesh is created in each cell centre of the existing DNS grid. This is shown schematically in figure 3.3. This subgrid is composed by two angles, the polar angle and the

azimuthal angle, denoted by the θ, and ϕ respectively. Similar to Silvestri et al. [26] a CLAM scheme is used in the spacial disctretization as this has been shown to work well when applied to a turbulent channel flow.

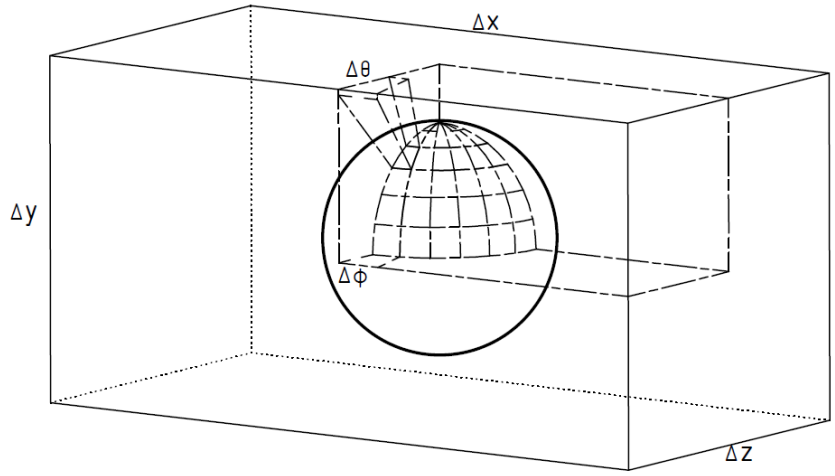

Figure 3.3: A visualization of the how the spherical mesh is laid out.

3.2.2. Model Validation

The validation of the thermal radiation model is done by comparing to an exact solution as shown by Sakurai et al. [21] for a sinusoidal temperature profile which is imposed by the function,

$$T(x) = 250 \cos\left(\frac{3\pi}{2}x\right) + 750\,. \tag{3.7}$$

By imposing the temperature profile in wall normal direction onto the fluid and executing a single radiation calculation step, a solution close to the analytical solution is expected. The initial temperature profile imposed on the fluid is shown in figure 3.4a. Figure 3.4b shows the results of the radiation model, and it can be observed that the model matches the result from the analytical solution.

A mesh resolution study was also performed in order to find a suitable mesh for the subgrid created for the model. Both polar angle and azimuthal angle are varied, and a total of 9 sets were tested. The sets 1 till 7 were tested on a grid of $N_x \times N_y \times N_z = 48 \times 96 \times 48$. Sets 8 and 9 were tested on the full grid to see the effect on computation time for these resolution. The results of these simulations are shown in table 3.1. It is concluded that a mesh of 8 in polar angle direction and 12 in azimuth direction

Table 3.1: Tested subgrid meshes for the Radiation model

Case name	N_θ	N_ϕ	**Case name**	N_θ	N_ϕ
Set1	24	16	Set6	10	8
Set2	16	8	Set7	8	12
Set3	12	8	Set8	10	8
Set4	16	6	Set9	8	16
Set5	10	6			

is a good compromise between the resolution obtained and needed computation time per radiation step.

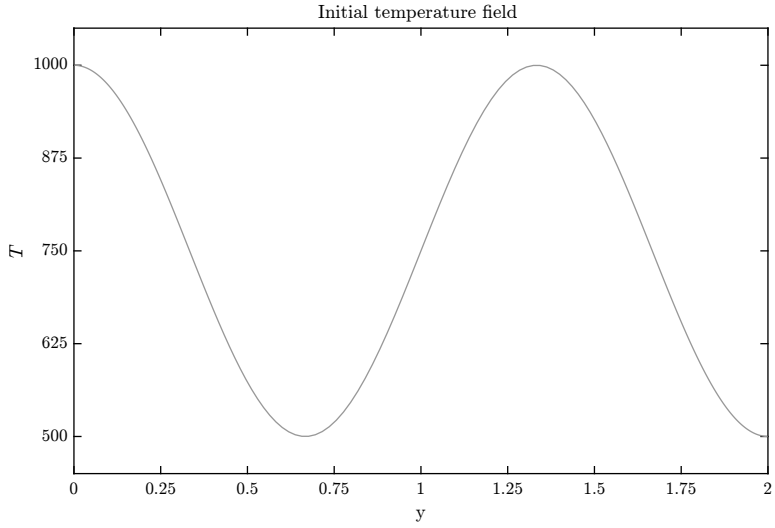

(a) Initial temperature field.

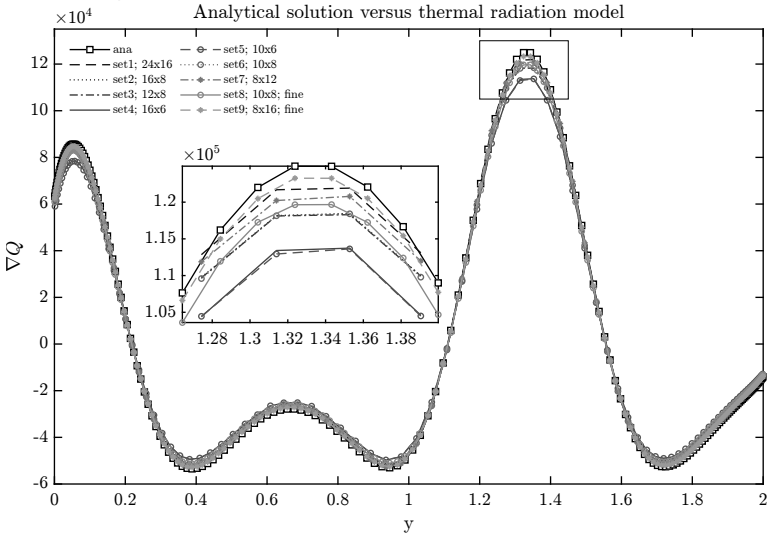

(b) Mesh resolution study for the thermal radiation model, comparing numerical results to the analytical solution.

Figure 3.4: Thermal radiation model validation and mesh resolution test.

3.3. Case selection

Only a select number of cases can be tested to investigate the effects of radiation on optically thick compressible flow as the Pl number and the absorption coefficient are varied. The Planck number,

$$Pl = \frac{\kappa_t T}{\sigma T^4 \delta}\,, \tag{3.8}$$

gives the ratio of thermal energy transferred by thermal conduction to thermal radiation, where a lower number increases the contribution of thermal radiation. The absorption coefficient quantifies the amount of radiation absorbed by the transfer medium and is linked to the optical thickness via equation (1.7).

A characteristic of supersonic channel flow simulations is that the channel height is set by the Reynolds and Mach number. Planck number uses a real length, and is thus fully constraint by the Reynolds and Mach number. In order to investigate the effects of thermal radiation on the flow, it is decided to decouple Planck number from the flow. The performance of the model was evaluated based on a set of short-run simulations where Pl was arbitrarily varied. The value of $Pl = 0.01$ was chosen as the effects of thermal radiation on the temperature field were visual after a short time. This makes it likely that after reaching convergence with the simulation that the effects of thermal radiation are

clearly noticeable. To get a broader perspective on the effects of Pl on the flow a value for Pl of 0.1 is also selected as this is an order higher than the previously selected value and should make it possible to observe a trend in behaviour.

The optical thickness base case value is chosen to match the highest value used by Silvestri et al. [26], $\zeta = 10$. To study the effect of a change in optical thickness two lower optical thicknesses are selected being $\zeta = 5$ and 1. These are chosen lower as this would be more in line with common occurrences in an industrial environment. The selected cases that are used for this research are shown in table 3.2.

Table 3.2: Simulation parameters.

Case name	Re	Ma	Pl	ζ
Ideal	3000	1.5	-	-
Pl001	3000	1.5	0.01	10
Pl01	3000	1.5	0.1	10
abs5	3000	1.5	0.01	5
abs1	3000	1.5	0.01	1

The mesh resolution for the different cases is given in table 3.3. Values given are calculated as follows:

$$\Delta_x^+ = \frac{\rho_w u_\tau dx}{\mu_w}\,, \qquad \Delta_x^\star = dx \cdot Re_\tau^\star\,.$$

In this equation the superscript $^+$ indicates wall units scaling, and the superscript * indicates semi local scaling.

Table 3.3: Mesh resolution.

Case name	Δy^+_{min}	Δy^+_{max}	Δz^+	Δx^+	Δy^*_{min}	Δy^*_{max}	Δz^*_{cl}	Δx^*_{cl}
Ideal	0.357	4.953	7.502	15.003	0.357	3.37	5.103	10.206
Pl001	0.33	4.579	6.936	13.871	0.33	3.884	5.882	11.765
Pl01	0.351	4.871	7.377	14.755	0.351	3.53	5.346	10.692
abs5	0.324	4.494	6.806	13.612	0.324	3.953	5.987	11.973
abs1	0.316	4.389	6.647	13.293	0.316	4.012	6.076	12.152

4

Results

The five cases detailed in table 3.2 are run, and results are compared. The effect on the quantities related to temperature, velocities, and compressibility are discussed.

4.1. Mean properties

The figures 4.1a, and 4.1b show the mean velocity profile in streamwise direction. Figure 4.1a shows $\overline{u}^*$ which is the steamwise velocity scaled semi-locally. Semi-local scaling is defined as:

$$u_\tau^\star = \sqrt{\frac{\tau_w}{\overline{\rho}}}\,, \qquad y^\star = \frac{y u_\tau^\star \overline{\rho}}{\overline{\mu}}\,, \qquad Re_\tau{}^\star = Re_\tau \frac{\sqrt{\overline{\rho}/\rho_w}}{\overline{\mu}/\mu_w}\,. \tag{4.1}$$

In the relations given in equation (4.1) the subscript $_w$ denotes a value taken at the wall, the superscript * denotes a value determined semi-locally, and u_τ is the wall friction velocity. For compressible flows it is found that using semi-local scaling collapses the data better than the traditionally used wall units. Furthermore, it had been shown that using Van Driest scaling collapses supersonic data better when compared to incompressible data. For Van Driest scaling first the scaling based on wall units u^+ is needed, which are defined as:

$$u^+ = \frac{u}{u_\tau}\,, \qquad u_\tau = \sqrt{\frac{\tau_w}{\rho_w}}\,, \qquad y^+ = \frac{y u_\tau \rho_w}{\mu_w}\,, \qquad Re_\tau = \frac{\rho_w u_\tau h}{\mu_w}\,. \tag{4.2}$$

For Van Driest scaling the Van Driest transformation is used which is written as,

$$u_{VD}^+ = \int_0^{\overline{u^+}} \sqrt{\frac{\overline{\rho}}{\rho_w}}\, d\overline{u}^+\,. \tag{4.3}$$

The streamwise velocity transformed as shown above is given in figure 4.1b. The mean streamwise velocity shows a reduction of velocity near the center of the channel, moving the velocity profile closer to that of an incompressible channel flow. A similar result for the change in velocity profile when the flow is affected by thermal radiation has been shown by Ghosh et al. [7]. The cases are grouped by Pl, with a smaller Pl moving the velocity profile closer the the profile from Kim et al. [12]. This trend is more clearly defined in figure 4.1a. For cases with $Pl = 0.01$ it is shown that decreasing the optical thickness increases the streamwise velocity profile.

As mentioned previously the Pl number is the ratio of convective heat transfer to radiative heat transfer. This means that in a case with a lower Pl number, relatively more heat transfer occurs by radiation than by conduction. Because the optical thickness in these cases is determined by the absorption coefficient, changing the Pl number is more a method of artificially increasing the importance of thermal radiation when comparing the thermal energy transferred by convection and radiation. This means that the Pl number is different from what the flow would be under normal circumstances. With this a direct method is created of directly enhancing the importance of thermal radiation by decreasing the relevance of thermal conduction.

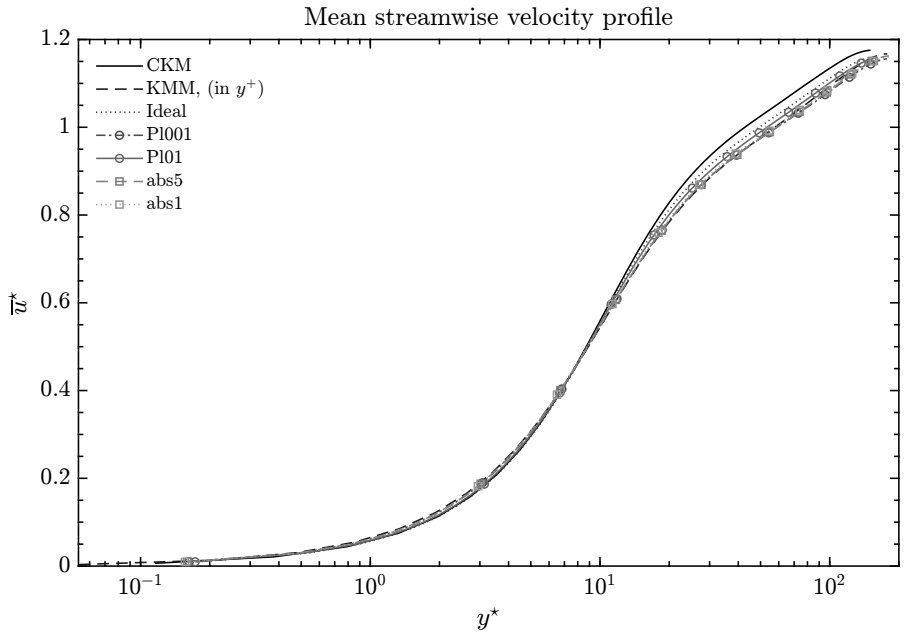

(a)

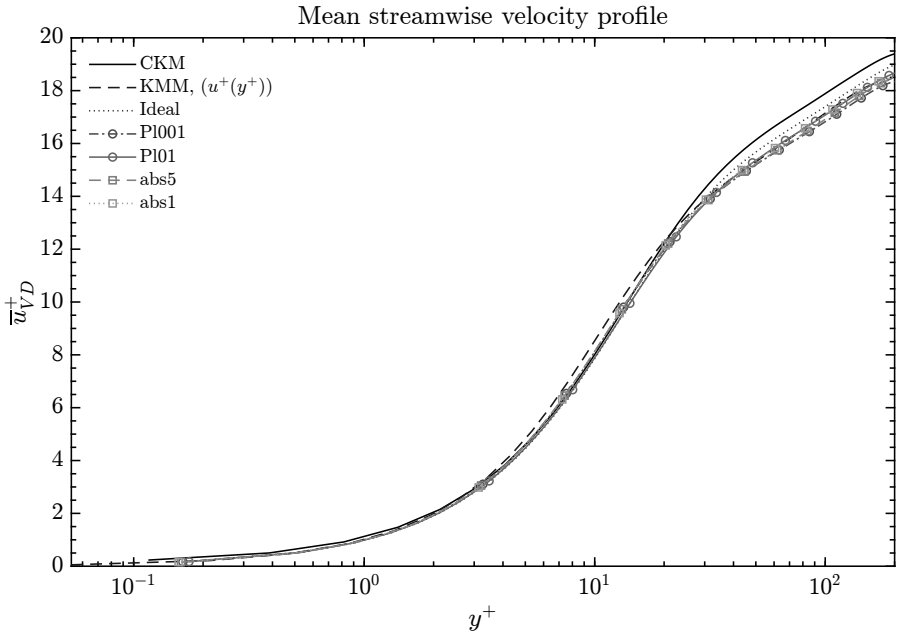

(b)

Figure 4.1: Mean streamwise velocity; figure 4.1a shows $\overline{u^+}$ as a function of $y^\star$ and figure 4.1b shows $\overline{u^{VD}}$ as a function of y^+; Both figures are compared to the data from Coleman et al. [4] and Kim et al. [12].

Velocity fluctuations for streamwise, spanwise, and wall-normal direction are shown in figures 4.2a, 4.2b, and 4.2c respectively. The data is normalized by u_τ and given as root mean square. Streamwise fluctuations shows a decrease in amplitude, when the effective radiation is increased. The effect of optical thickness becomes greater closer to the center-line of the channel as it is observed that higher fluctuations occur for flows with a lower optical thickness. Spanwise velocity fluctuations shows a change around $y^\star = 10$ for the cases with $Pl = 0.01$ as the gradient decreases around this point. Similar behaviour is seen with wall-normal velocity fluctuations. A lower optical thickness decreases velocity fluctuation.

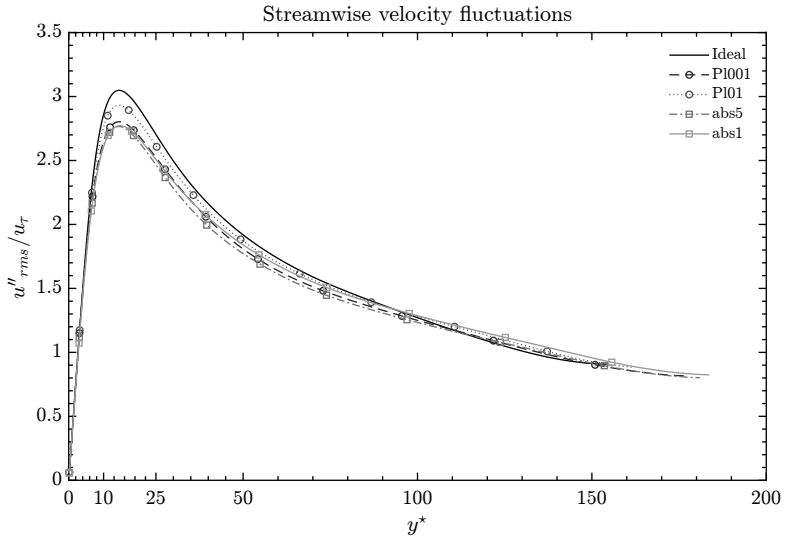

(a)

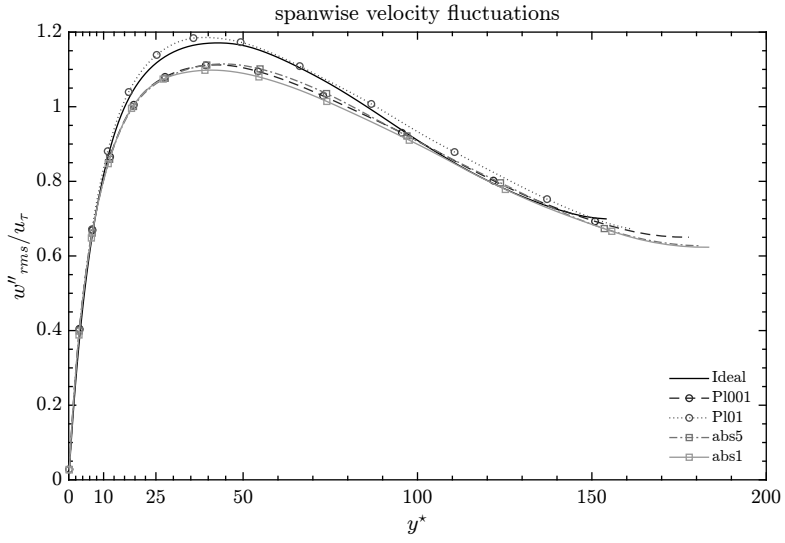

(b)

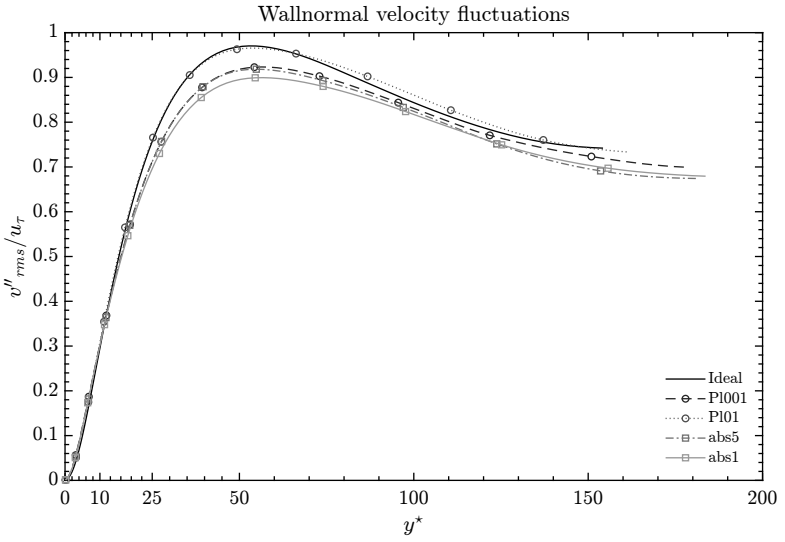

(c)

Figure 4.2: Streamwise and spanwise Velocity fluctuations, figure 4.2a shows u''_{rms}/u_τ, figure 4.2b w''_{rms}, and wall-normal velocity fluctuations in figure 4.2c as v''_{rms}; all as a function of $y^\star$.

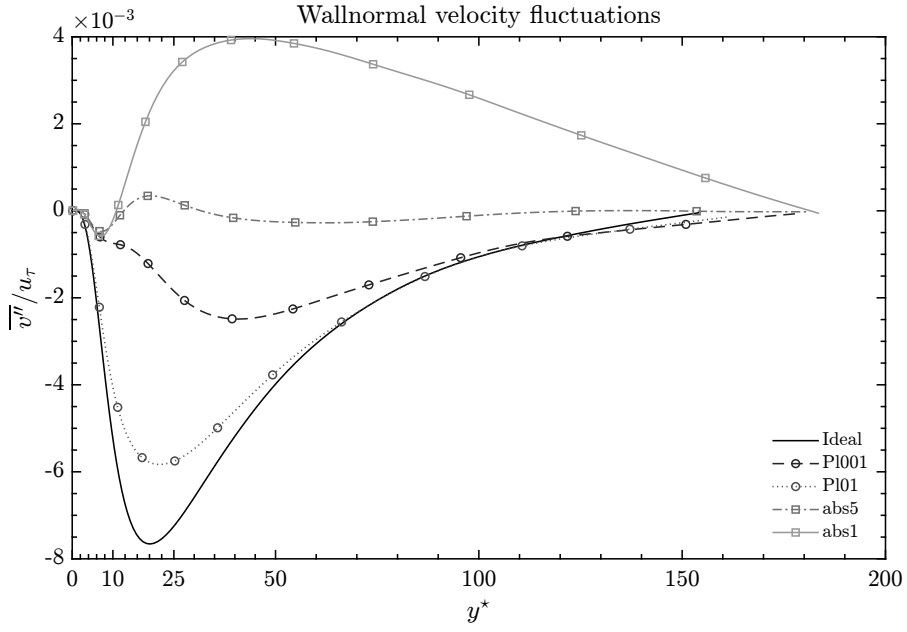

(a)

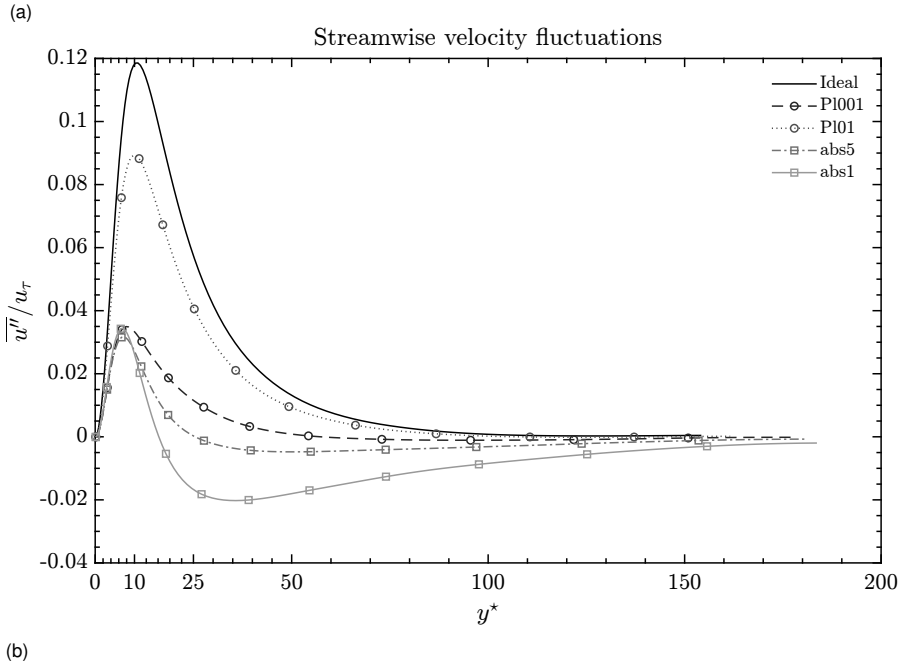

(b)

Figure 4.3: Wall-normal velocity fluctuations, shown in figure 4.3a as $\overline{v''}$ and in figure 4.3b as $\overline{u''}$, both as a function of $y^\star$.

Figures 4.3a and 4.3b show the Reynolds averaged Favre velocity fluctuations. For wall-normal fluctuations a shallower gradient is found that has shifted closer to the wall for a lower Pl. Decreasing optical thickness shows a flip in sign for the velocity fluctuations. Similar to wall-normal direction, streamwise velocity fluctuations has a decrease in gradient and a region for which a sign flip occurs. This change in sign for the velocity fluctuations means that the following must be true:

$$\begin{aligned} &\overline{v''} > 0\,, \\ &\overline{v''} = -\frac{\overline{\rho' v'}}{\overline{\rho}}\,, \\ &\overline{\rho' v'} < 0\,. \end{aligned} \tag{4.4}$$

This can mean two things, either density fluctuations or velocity fluctuations change sign due to the effect of radiation. This can be determined by investigating the Reynolds stresses. In the figures 4.4a, 4.4b, and 4.4c it is shown that the profiles given do not change sign. To explain this behaviour further a closer look is given to turbulent flow behaviour close to the wall, in particular to coherent structures. Coherent structures near the wall have been found to have a set of characteristics, as summarised by Robinson [20]. So called slow moving streaks are found close to the wall at around $y^+ = 7$ and slowly rise. At around $y^+ = 10$ these streaks eject away from the wall, taking high density fluid away from the wall. This space left by the upwards moving streak is filled by fast moving, low density streaks that sweep down. This process still holds for flows with radiation as $\overline{\rho u'' v''}$ shows no change in behaviour. This means that the only way for $\overline{v''} > 0$ to be valid is for $\rho' < 0$, which in turns means that streaks ejecting contain low density fluid. Density fluctuations being the term that switches sign is also the logical quantity to do so, as it would otherwise suggest that u' and v' both needed to switch sign to preserve Reynolds stress R_{xy} meaning that high speed streaks could be found near the wall, which is counter intuitive with a no-slip boundary condition.

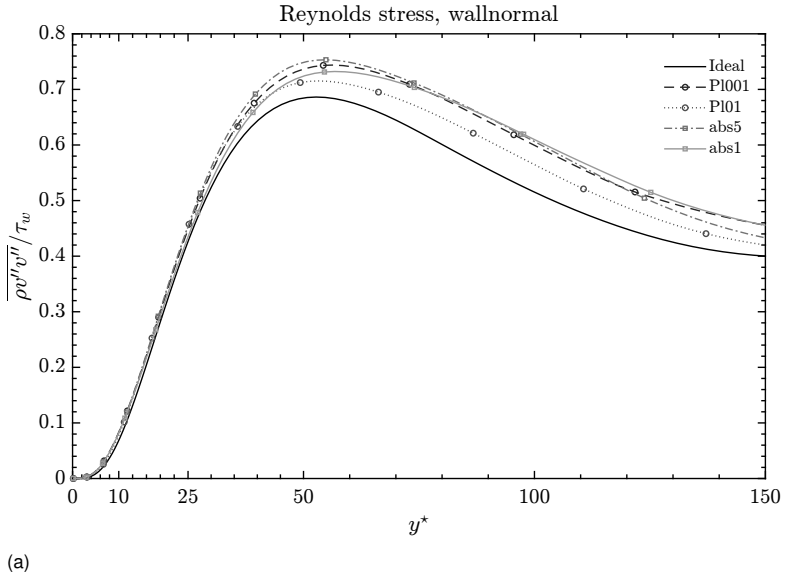

(a)

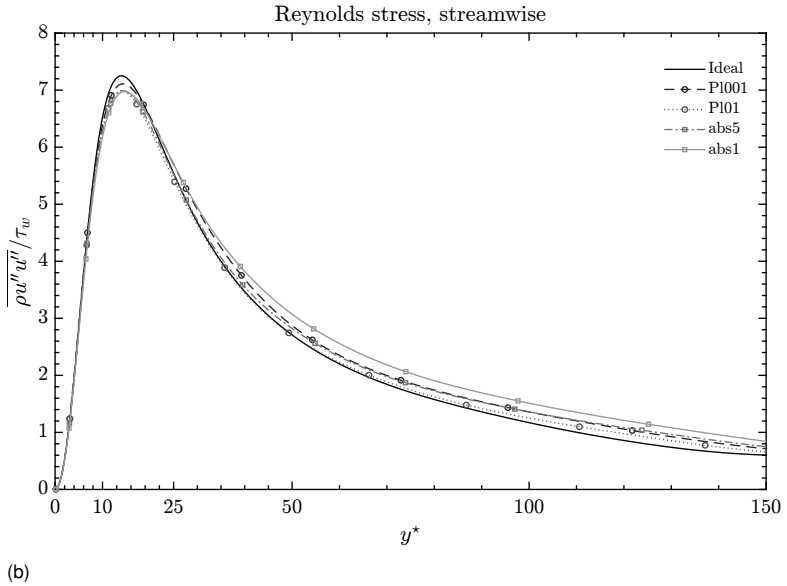

(b)

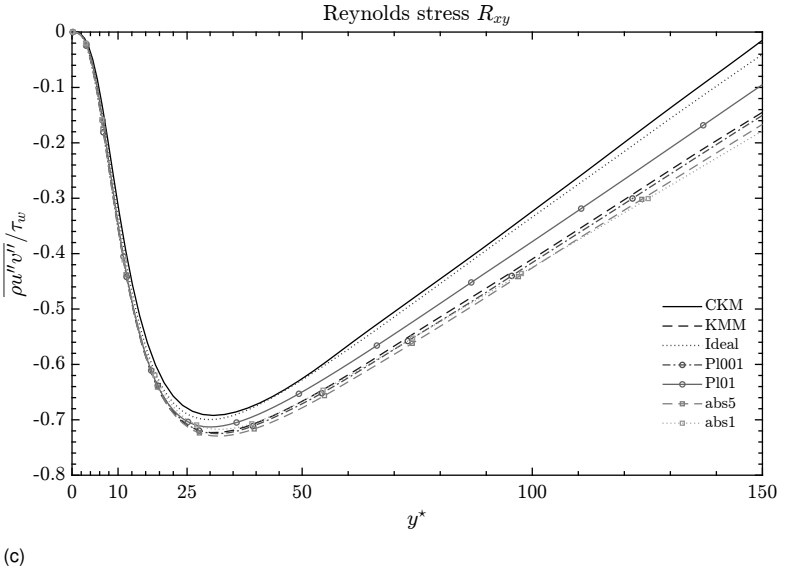

(c)

Figure 4.4: Reynolds stress, shown in figure 4.4a as $\overline{\rho v'' v''}$, in figure 4.4b as $\overline{\rho u'' u''}$, and in figure 4.4c as $\overline{\rho u'' v''}$, all as function of $y^\star$. The data in figure 4.4c is compared to data from Coleman et al. [4] and Kim et al. [12].

The Reynolds stress in streamwise direction shows a decreases in magnitude, for which cases are grouped by Pl number. Optical thickness does not show an apparent effect in this region. Near the center-line of the channel the case Pl01 remains similar to the Ideal case until around $y^\star = 80$ after which it increases. For the cases where $Pl = 0.01$ it can be observed that a reduction in optical thickness increases the Reynolds stress.

In wall-normal direction an increase in Reynolds stress is found when Pl increases. Decreasing optical thickness from 10 to 5 increases the stress, with a slightly steeper gradient. When optical thickness is lowered further however, it shows an opposite effect, with a more shallow gradient. This results in a lower stress which simultaneously is shifted further away from the wall. Reynolds stress R_{xy} in figure 4.4c is compared to both data from Coleman et al. [4] and Kim et al. [12] with which it can be shown that the Reynold stress profiles behaves more closely to those found in incompressible turbulence as the relevance of radiation is increased. The case Pl001 more closely resembles to the profile from Kim, while the cases abs5 and abs1 show an even lower Reynolds stress.

The mean density profile is shown in figure 4.5, normalised by ρ_w. The mean temperature is shown in figure 4.6, and is normalized by T_w. Temperature and density are related to each other by the ideal gas law. As the relevance of radiation is increased, the gradient is lowered for both quantities. As the optical thickness is lowered an inflection point becomes apparent around $y^\star = 11$. This location coincides with the location where high levels of turbulent production and dissipation occur. It can be seen that the temperature drops in the center of the channel. This is likely due to the increase in length scale of thermal radiation as optical thickness is lowered. As the length scale increases the energy transfer can occur over larger distances. Due to this it becomes possible for fluid located beyond $y^\star = 11$ to transfer thermal energy to the colder fluid near the wall. For the case of abs1 this leads to a temperature profile in which the maximum is not found in the channel center. Due to the previously mentioned coupling the same phenomena can be seen for density where fluid is denser in the center than around $y^\star = 11$.

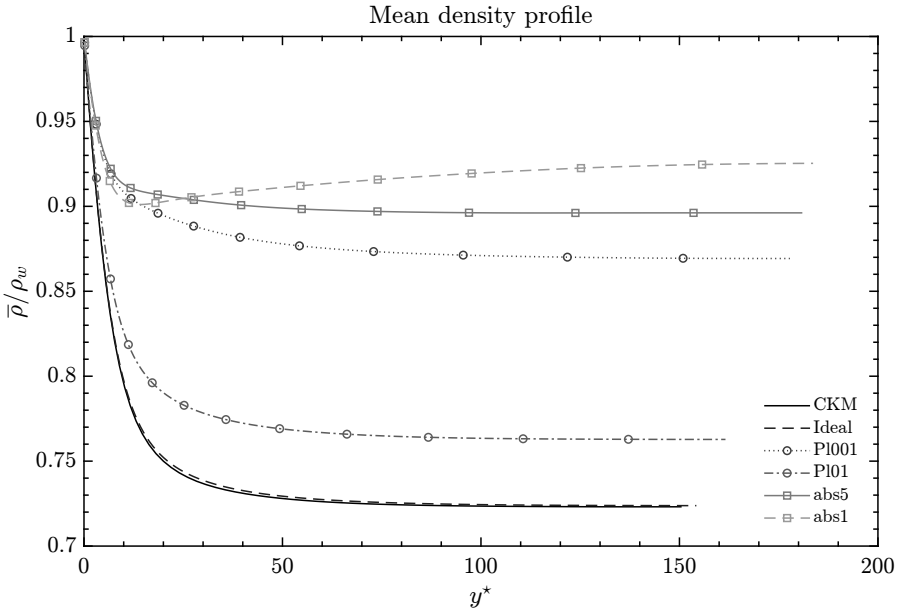

Figure 4.5: $\overline{\rho}/\rho_w$ as a function of $y^\star$.

Temperature and density fluctuations are shown in the figures 4.7a, and 4.7b. Density is normalized by τ_w. Temperature fluctuation is normalized by the friction temperature which is defined as:

$$T_\tau = \frac{q_w^{cd}}{C_p \rho u_\tau} \,. \tag{4.5}$$

For the chosen nondimensionalization, C_p is chosen constant and equal to:

$$C_p = \frac{1}{\gamma - 1} \,. \tag{4.6}$$

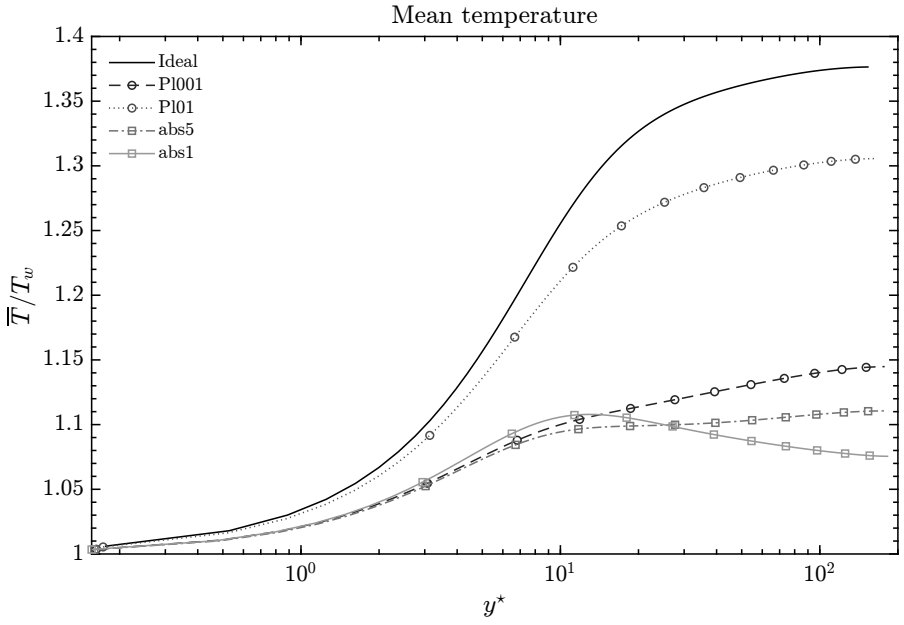

Figure 4.6: $\overline{T}/T_w$ as a function of $y^\star$.

For both the temperature and density fluctuations it is the case that as Pl decreases, the maximum moves closer to the wall and reduces. For temperature, decreasing optical thickness shows an increase in gradient close to the wall. The reduction in fluctuations, and the inflection point around $y^\star = 11$ for the case abs1 are the result of emission which functions as a sink term. The behaviour of density fluctuations can be explained similarly to the behaviour of temperature fluctuations.

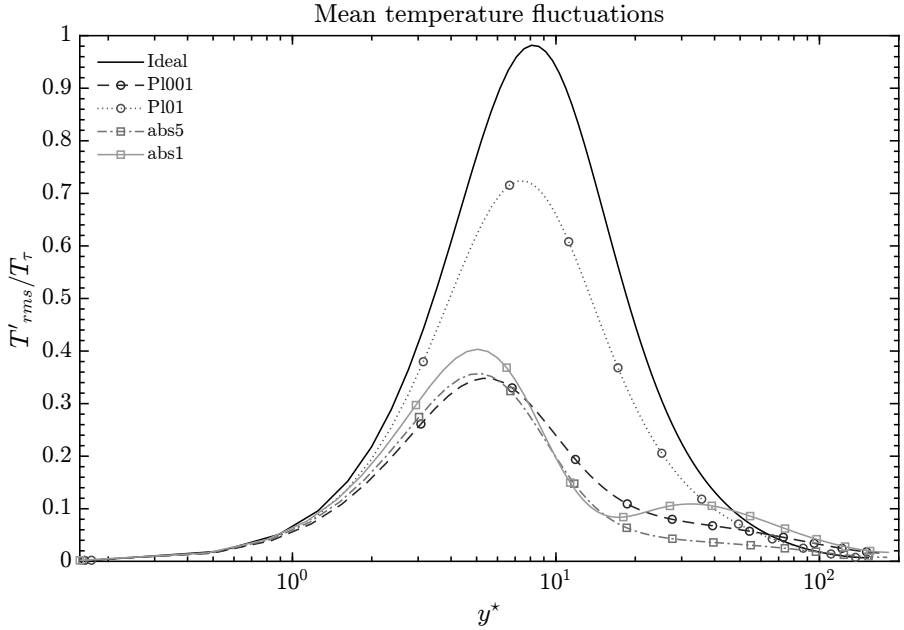

(a)

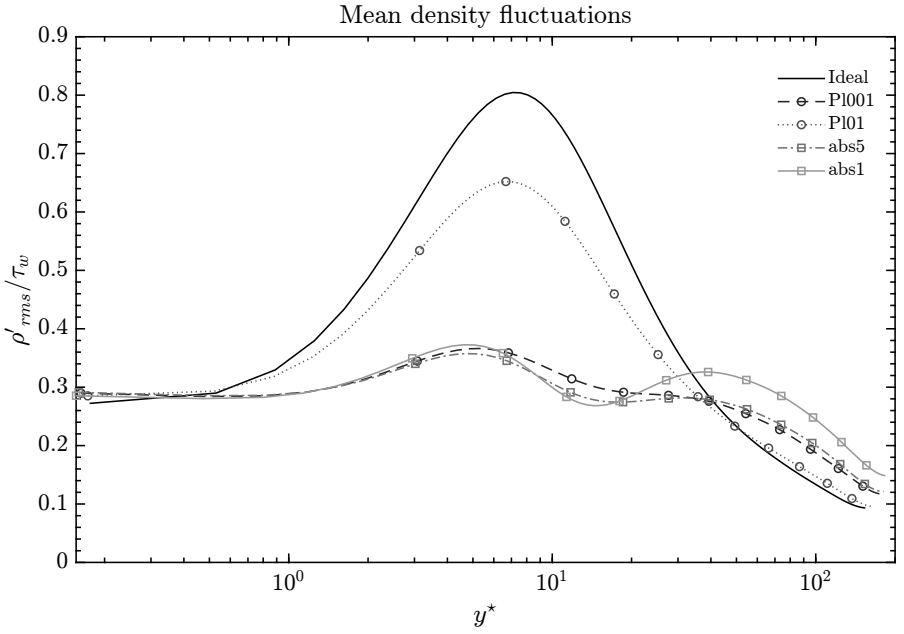

(b)

Figure 4.7: Temperature fluctuations T'_{rms}/T_τ shown in figure 4.7a and density fluctuations ρ'/τ_w in 4.7b, both as a function of $y^\star$.

Radiative power (P_R) is defined as a combination of emission and incident radiation:

$$\overline{P_R} = \nabla \cdot \overline{q_r} = \kappa \overline{E} - \kappa \overline{G} \,. \tag{4.7}$$

For normalization of the radiative quantities, the radiation-based frictional temperature $T_\tau^\dagger$, as defined by Zhang et al. [32], is used. The term is defined as:

$$\begin{aligned} T_\tau^\dagger &= \left(\overline{q_{cd}}_w - \int_0^y \nabla \cdot q_r dy \right) / \left(\overline{\rho} C_p u_\tau \right) \\ &= \frac{\overline{q_{cd}}_w - \overline{q_r}_w}{\overline{\rho} C_p u_\tau} \\ &= \frac{\overline{q^\dagger}}{\overline{\rho} C_p u_\tau} \,, \end{aligned} \tag{4.8}$$

for which the conductive heat flux q_{cd}, the turbulent heat flux $\overline{\rho}\widetilde{v''h''}$, and the radiative heat flux are summed to form the radiation-based heat flux $\overline{q^\dagger}$. This normalization method does not give the desired result in every case in which quantities are compared, but works better than using the unmodified frictional temperature. Friction temperature itself is obtained by replacing the numerator in equation (4.8) by $q_{cd,w}$. For the normalization of budget terms Vicquelin et al. [30] proposes the use of

$$\frac{\overline{q^\dagger}^2}{\overline{\mu}} \,.$$

The profiles for both normalization quantities is shown in the figures 4.8a, and 4.8b.

Shown in the figures 4.9a, 4.9b, and 4.9c are the mean incident radiation, emission, and radiative power respectively, with the quantities given without normalization. The gradient of mean incident radiation shows a decrease as optical thickness is decreased. This is similar to the effect observed for incompressible flow by Silvestri et al. [26]. Mean emission shares its profile with mean temperature as it is directly proportional. Radiative power increases with both a decrease in Pl and in increase in optical thickness, similar to the effects seen previously in literature.

Emission fluctuations can be seen in figure 4.10b and decrease as the Pl is lowered. Furthermore both the change in Pl as well as κ show the maximum fluctuations shifting closer to the wall. Fluctuating incident radiation is observed to drop in magnitude by lowering Pl, and κ. Lowering the optical thickness has been seen to lower incident radiation by for instance Silvestri et al. [26]. Fluctuating radiative power is written as

$$\overline{\nabla Q'^2} = \kappa^2 \left[\overline{E'^2} + \overline{G'^2} - \overline{2E'G'} \right] \,, \tag{4.9}$$

and is shown in figure 4.10a. Comparing to the changes in magnitude for the mean radiative power, it is interesting to note that the radiative power fluctuations of the abs1 case are lower than the Pl01 case. This is due to the increase of emission fluctuations in the abs1 case by temperature fluctuations which peak around $y^\star = 12$ as shown previously. As incident radiation does not increase around this location, it leaves the fluctuating radiative power lower compared to other cases.

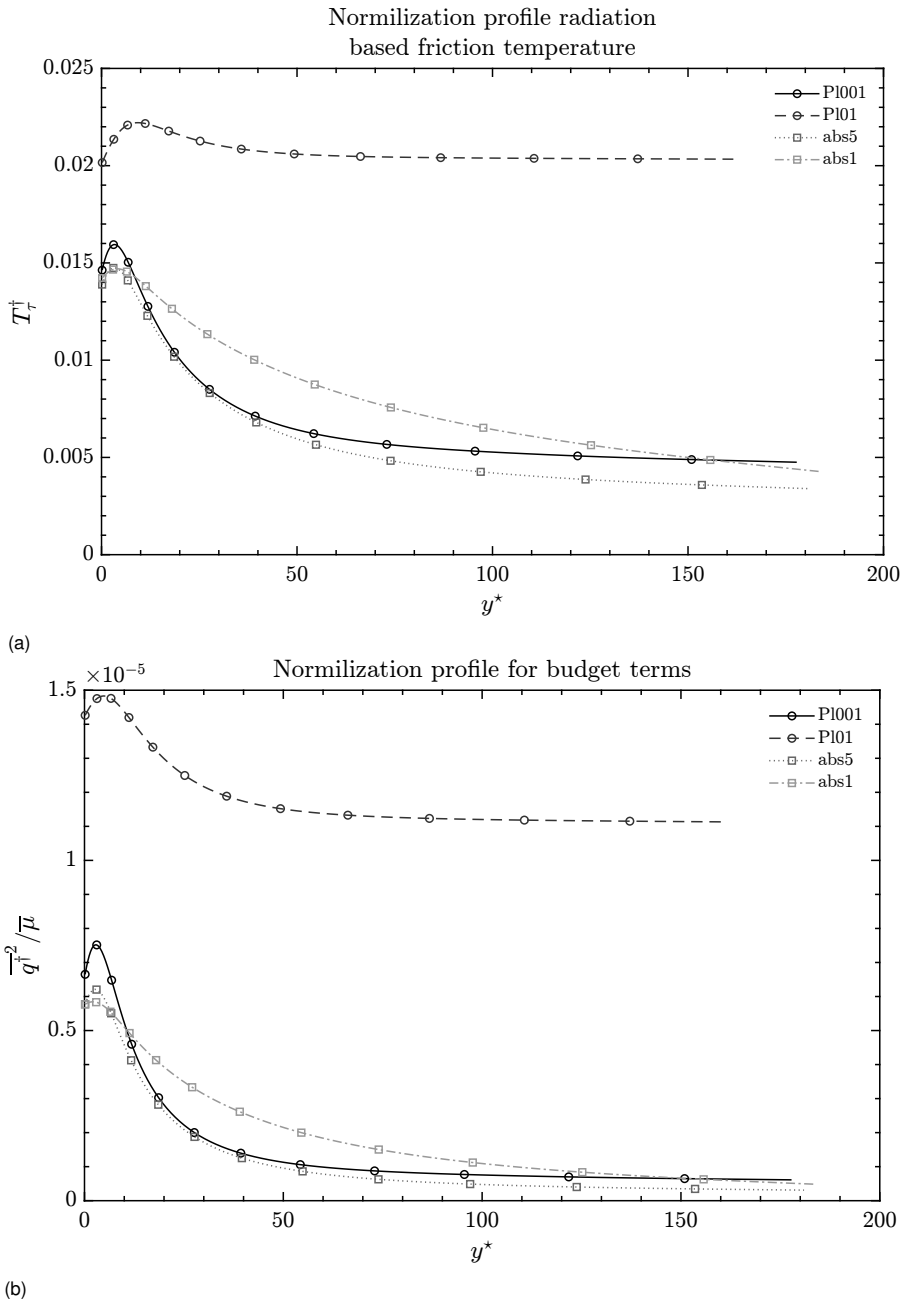

Figure 4.8: Radiation based friction temperature $T_\tau^\dagger$ shown in figure 4.8a and normalization profile for budget terms $\overline{q^\dagger}^2/\overline{\mu}$ in 4.8b, both as a function of $y^\star$.

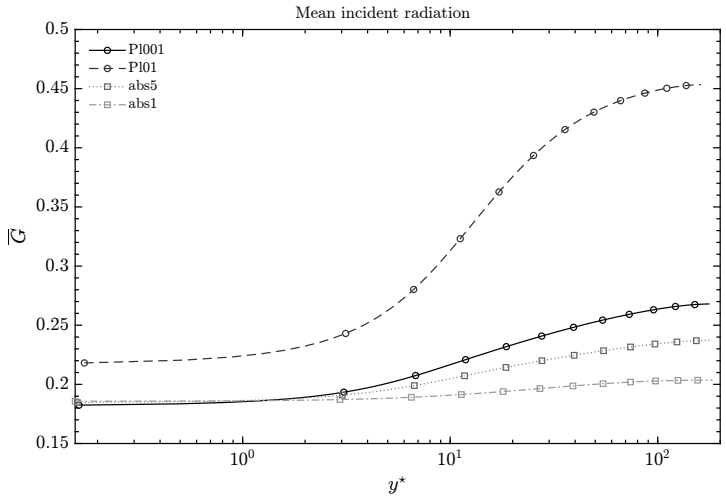

(a)

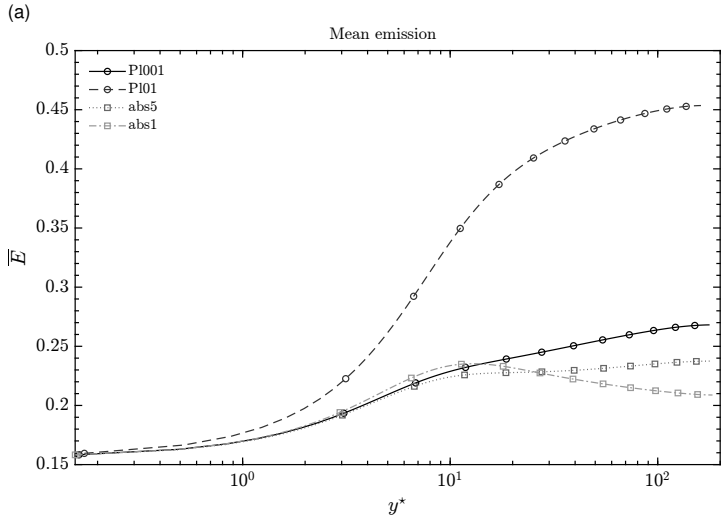

(b)

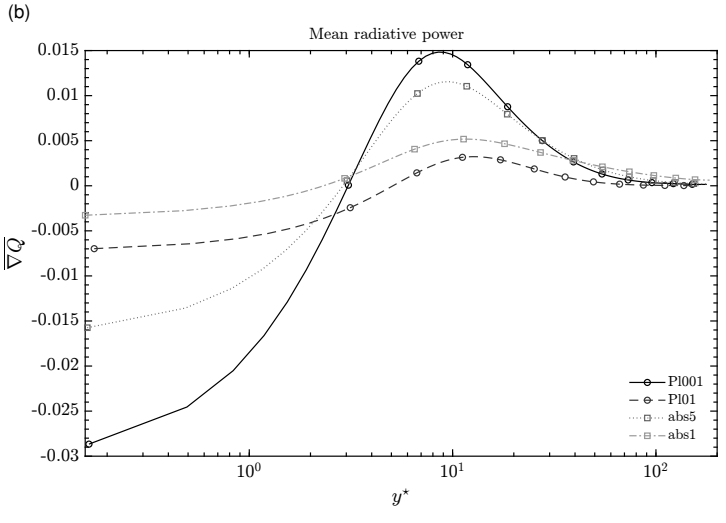

(c)

Figure 4.9: Figure 4.9a shows the mean incident radiation $\overline{G}$, figure 4.9b shows the mean emission $\overline{E}$, and figure 4.9c shows the mean radiative power $\overline{\nabla Q}$, all as a function of $y^\star$.

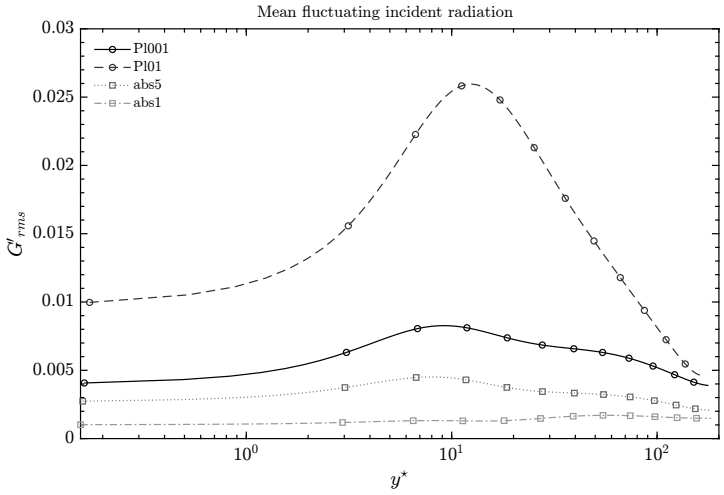

(a)

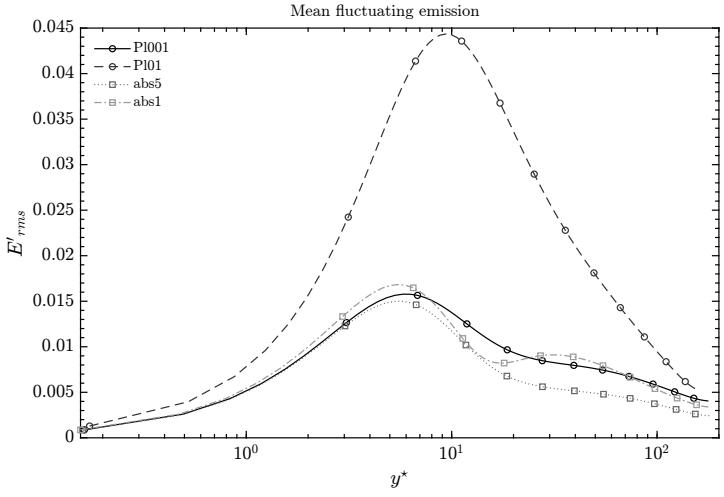

(b)

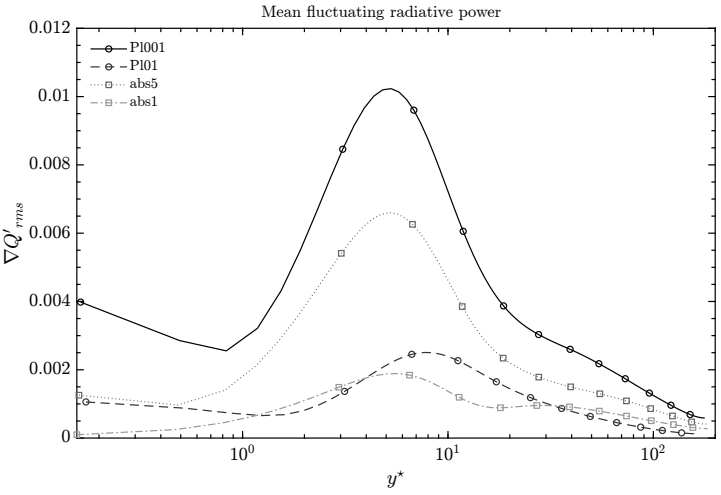

(c)

Figure 4.10: Figure 4.10a shows the mean fluctuating incident radiation $G'_{rms}/T_\tau^\dagger$, figure 4.10b shows mean fluctuating emission $E'/T_\tau^\dagger$, and figure 4.10c shows the mean fluctuating radiative power $\nabla Q'_{rms}/T_\tau^\dagger$, all as a function of $y^\star$.

Mean pressure and mean pressure fluctuations are normalized by p_w and τ_w respectively, and are shown in figures 4.11a, and 4.11b. The effect of increasing the relative importance of radiation is clearly visible in mean pressure, as relatively speaking a large increase in the near wall gradient is found. Consequently a lower magnitude for mean pressure can be observed for both Pl numbers used. Near wall pressure fluctuations increase with the changes when decreasing both Pl and κ are lowered. This change in magnitude goes paired with a shift of the maximum closer to the wall. In figure 4.11b an intersection point can be identified after which results from cases affected by radiation are found to have lower pressure fluctuations. In the work of Ghosh et al. [7] it is shown that the pressure fluctuation is lower for radiative cases over nearly the entire channel height. It should be noted that this was done for a low optical thickness flow.

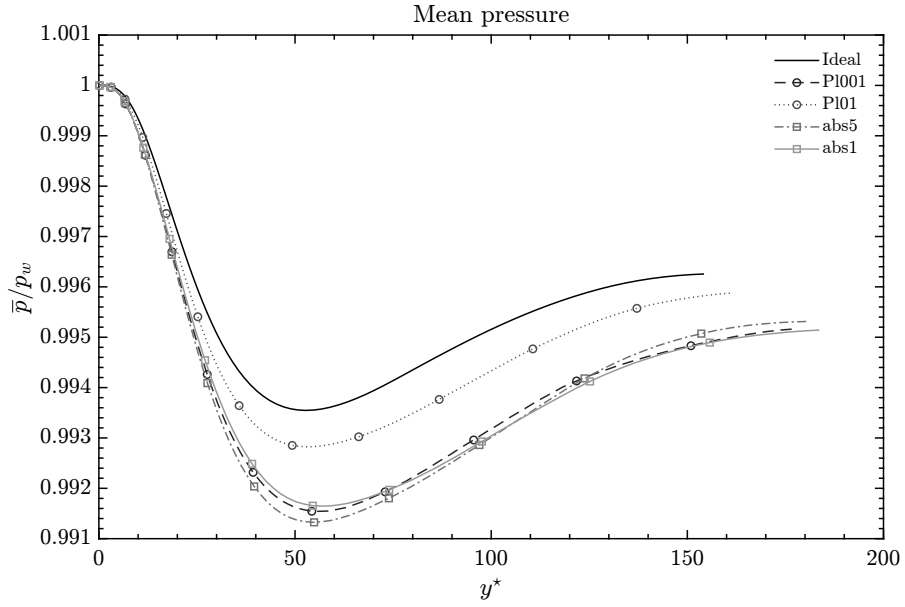

(a)

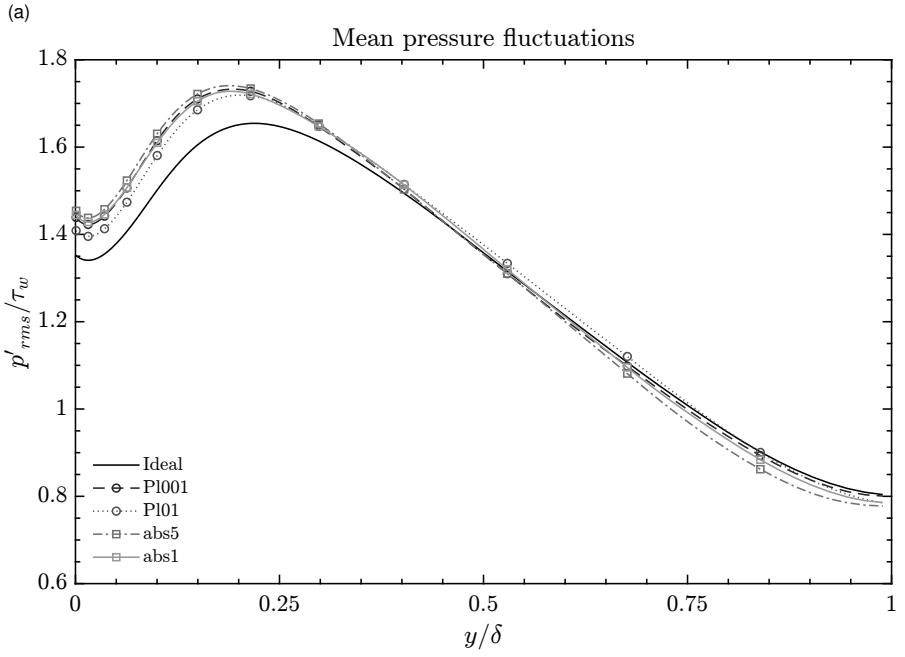

(b)

Figure 4.11: Mean pressure fluctuations fluctuations $\overline{p}/\tau_w$ as a function of $y^\star$ shown in figure 4.11a, and as a function of $y/2\delta$ in figure 4.11b.

4.2. Effect of thermal radiation on temperature

The turbulent heat flux in wall-normal direction is given in figure 4.12a. A similarity in profile with v'' can be seen across all cases. Although not shown, this similarity remains even when the quantity is not normalized by the friction temperature. Both enthalpy fluctuations and mean density increase the gradient of the turbulent heat flux near the wall. In streamwise direction, figure 4.12b, it can be seen that as optical thickness is lowered a reversal of the transfer direction is found. This is in agreement with the results found for temperature and density fluctuations.

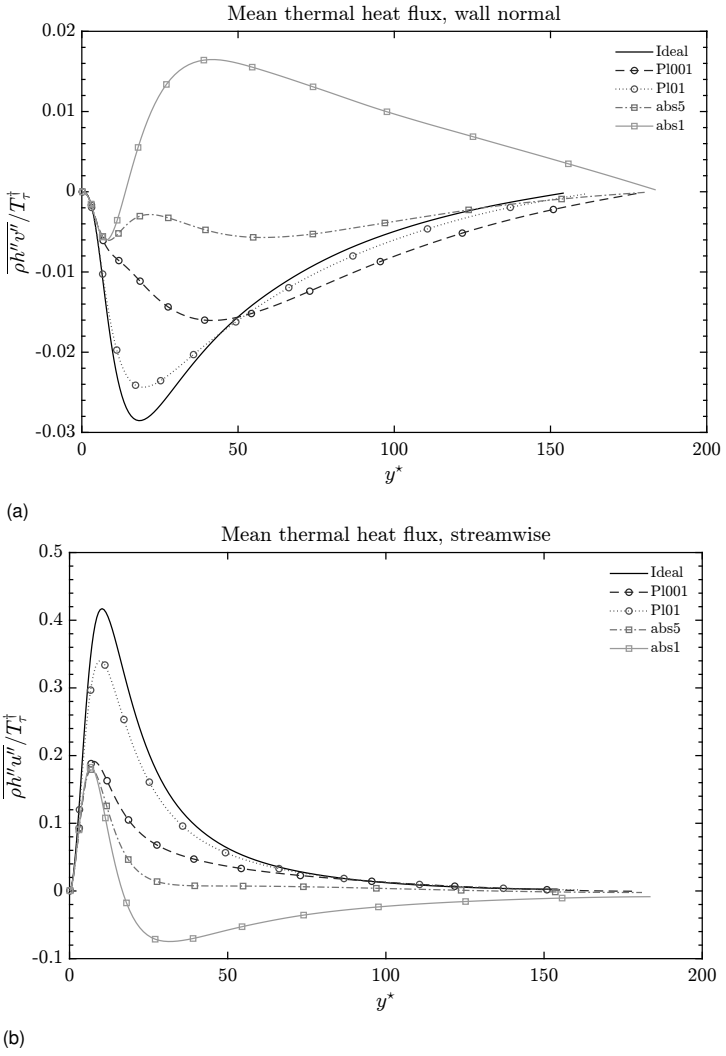

Figure 4.12: Mean turbulent heat flux in wall-normal direction $\overline{\rho v'' h'}$ shown in figure 4.12a and streamwise direction $\overline{\rho u'' h'}$ shown in figure 4.12b, both as a function of $y^\star$.

To further investigate the effect of radiation on temperature, the enthalpy variance budget is discussed. The enthalpy variance budget is derived in appendix A and is defined as:

$$\underbrace{-\overline{\rho u_j'' h''}\,\widetilde{\frac{\partial h}{\partial x_j}}}_{\mathcal{P}} + \underbrace{\frac{\partial \overline{h'' u_j' \tau_{ij}'}}{\partial x_j}}_{\mathcal{T}_w} + \underbrace{\frac{\partial \overline{h'' q_j}}{\partial x_j}}_{\mathcal{T}_q} - \underbrace{\frac{\partial \overline{\frac{1}{2}\rho u_j'' h'' h''}}{\partial x_j}}_{\mathcal{T}_t} + \underbrace{\overline{h''}\,\overline{\frac{\partial \tau_{ij} u_j}{\partial x_j}}}_{\mathcal{M}_w} + \underbrace{\overline{h''}\,\overline{\frac{\partial q_j}{\partial x_j}}}_{\mathcal{M}_q} - \underbrace{\overline{u_j' \tau_{ij}' \frac{\partial h''}{\partial x_j}}}_{\mathcal{D}_w} - \underbrace{\overline{q_j' \frac{\partial h''}{\partial x_j}}}_{\mathcal{D}_q} = 0\,. \tag{4.10}$$

The individual terms in equation (4.10) denote:

- $\mathcal{P}$, production.
- $\mathcal{T}_w$, transport by work fluctuations.
- $\mathcal{T}_q$, molecular diffusion.
- $\mathcal{T}_t$, transport by turbulent fluctuations.
- $\mathcal{M}_w$, mass transport by work.
- $\mathcal{M}_q$, molecular mass transport.
- $\mathcal{D}_w$, dissipation by work fluctuations.
- $\mathcal{D}_q$, molecular dissipation.

The quantity q in equation (4.10) represents total heat flux, and can be decomposed into conduction and radiation heat flux with,

$$q = q_{cd} + q_r \,. \tag{4.11}$$

This means that the three heat flux terms in the budget can be expended into:

$$\begin{aligned}
\frac{\partial \overline{h'' q_j}}{\partial x_j} &= \frac{\partial \overline{h'' q_{cdj}}}{\partial x_j} + \frac{\partial \overline{h'' q_{rj}}}{\partial x_j} \,, \\
\overline{q_j' \frac{\partial h''}{\partial x_j}} &= \overline{q_{cd_j}' \frac{\partial h''}{\partial x_j}} + \overline{q_{r_j}' \frac{\partial h''}{\partial x_j}} \,, \\
\overline{h''} \overline{\frac{\partial q_j}{\partial x_j}} &= \overline{h''} \overline{\frac{\partial q_{cdj}}{\partial x_j}} + \overline{h''} \overline{\frac{\partial q_{rj}}{\partial x_j}} \,.
\end{aligned} \tag{4.12}$$

Important note
Because of the size of the data of an individual quantity in a DNS, it is infeasible to save down a large selection of quantities. Therefore it is common practice to save down a minimal number of quantities, and post-processing is used to calculate all the other quantities.
For the simulations performed for this thesis, data for the incident radiation and radiative power have been saved down in addition to e_0, ρ and the three velocity directions. At a later stage it was discovered that radiative flux should have been saved down in all three separate directions in addition to this. Because of this, not all budget terms can be retrieved as obtaining a flux in a specific direction from a divergence is not possible.
This means that from the expansion of the heat flux terms as shown in equation 4.12, only the radiation term from the last line can be determined. Any use of q henceforth is based on conduction only unless otherwise specified.

The production shown in figure 4.13 decreases as Pl is lowered. Simultaneously the maximum moves closer to the wall. A decrease in optical thickness shows an increase in gradient both before and after the maximum.

For the cases with $Pl = 0.01$ a second local maximum can be found in production further away from the wall. The additional production for the case Pl001 is centred around $y^\star = 37$ which coincides with the higher magnitude of $\overline{\rho u'' h''}$. The difference in behaviour between the cases abs5 and abs1 can partly be explained by temperature fluctuations and the second maximum found with these for the case abs1 as shown in figure 4.7a. This maximum occur around the same location $y^\star = 30$ as this second maximum.

Transport terms by work, turbulent and molecular fluctuations are shown in figures 4.14a, 4.14b, and 4.14c respectively. The graph for viscous transport indicates an insufficient amount of snapshots were used to determine this quantity for flows affected by radiation. Because of this it is difficult to draw strong conclusions for this particular quantity and is chosen not to be shown.

For turbulent transport a reduction in the first near wall peak is found for a reduction of Pl. It is also found that a reduction in optical thickness increases turbulent transport again. This reduction and shift of turbulent transport is linked to the change in production. A second reduction in magnitude is found between $y^\star = 7$ and 11, for which a larger shift towards the wall is found.

The effect of optical thickness is also more clearly defined in this second peak with a larger value for ζ reducing the magnitude to a larger degree. The sharper gradient after the third peak around $y^\star = 15$ is a result of the change in temperature fluctuations that has been shown previously. For molecular transport, the near wall gradient increases with an increase in effective radiation transfer. Around $y^\star = 11$ a local maximum exist for flows affected by radiation which coincides with the inflection point found for temperature.

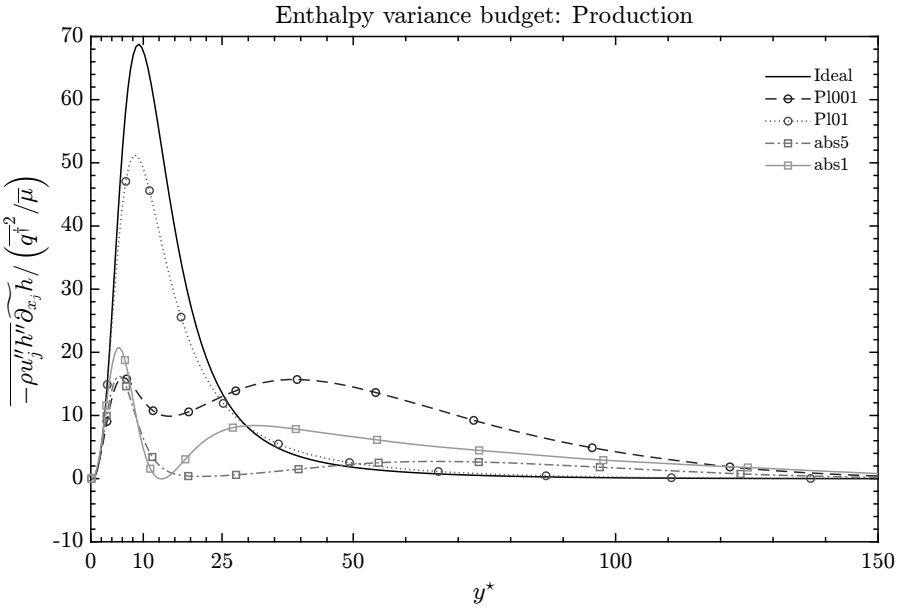

Figure 4.13: Production of enthalpy variance, normalized by $\overline{q^\dagger}^2/\overline{\mu}$, and as function of $y^\star$.

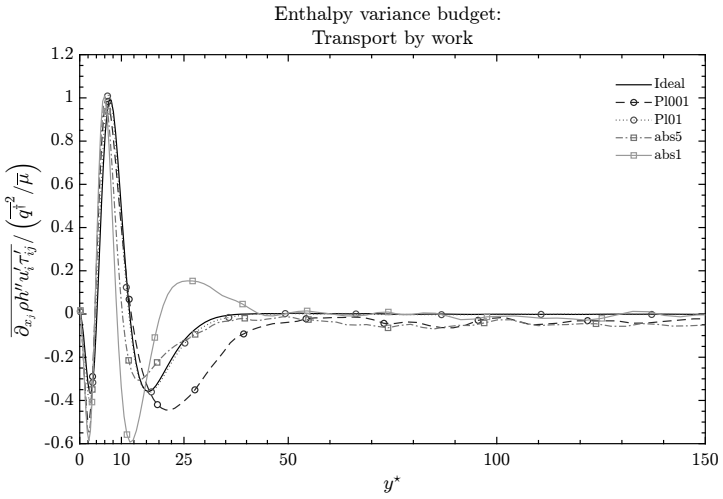

(a)

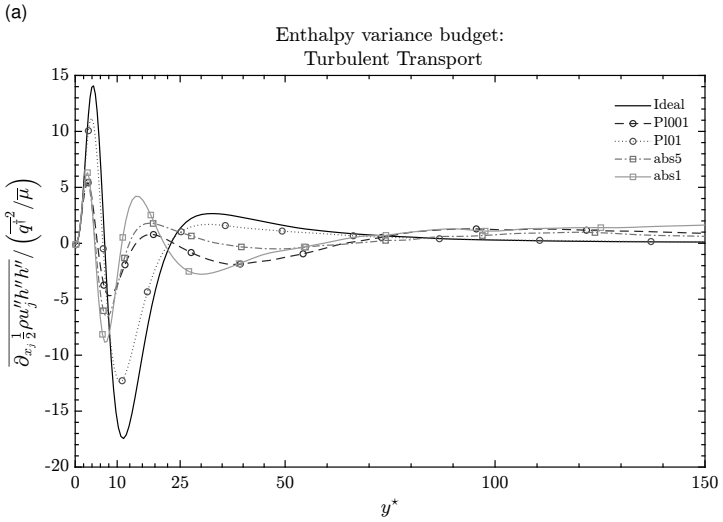

(b)

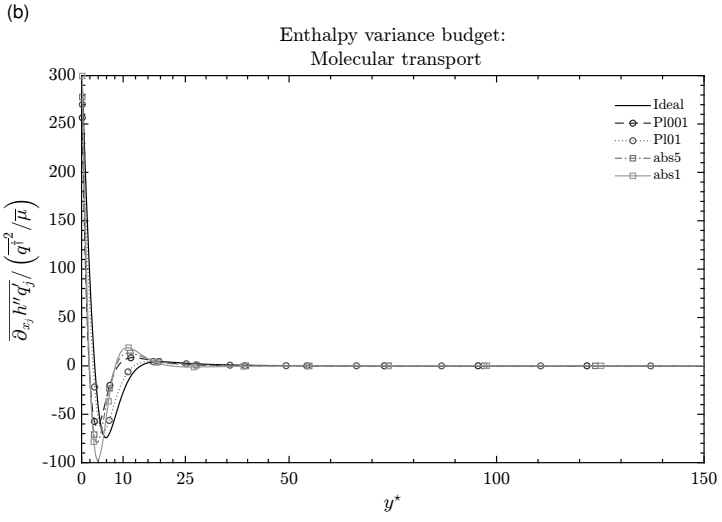

(c)

Figure 4.14: (A), Transport by mean fluctuating work $\partial_{x_j}\overline{h''u_j'\tau_{ij}'}$. (B) transport by mean turbulent fluctuations $\partial_{x_j}\overline{\frac{1}{2}\rho u_j''h''h''}$. (C) Molecular transport by conduction $\partial_{x_j}\overline{h''q_j}$. All normalized by $\overline{q^\dagger}^2/\overline{\mu}$, and as function of $y^\star$.

Near wall dissipation by work shows a shift to negative dissipation, meaning that energy is added to the enthalpy variance budget as optical thickness is lowered as can be seen in figure 4.16. Dissipation by conduction is shown in 4.16c. Similar to the graph shown for molecular transport a lack of data for radiative flux makes it that the values are based solely on conduction.

It should be noted that the magnitude value shown for this quantity is expected to be larger than production because the contribution by radiation is not taken into account. To show that it is not due to the normalization used production, molecular transport and turbulent transport are shown without normalization for de Ideal case in figure 4.15.

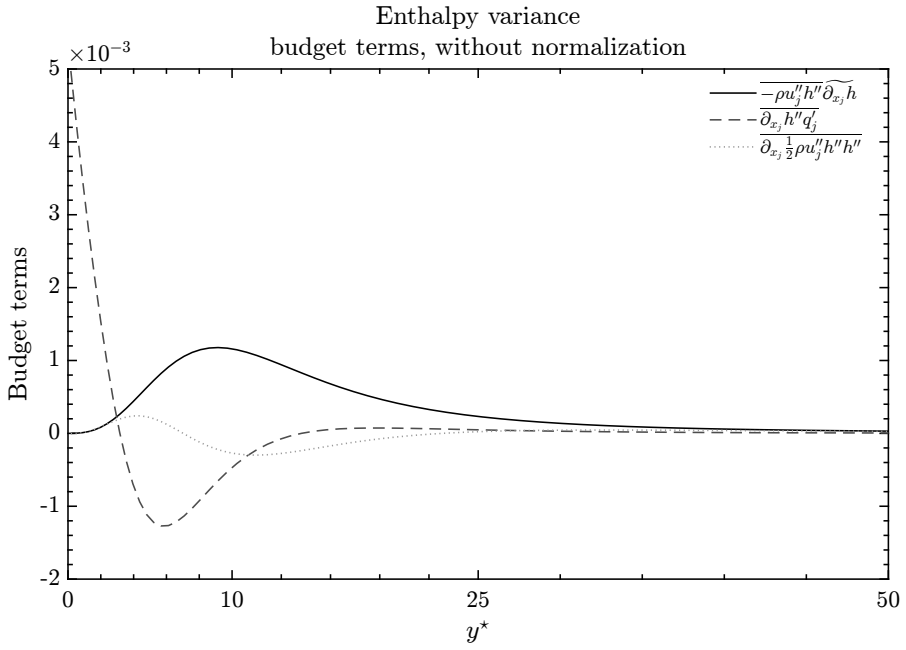

Figure 4.15: Production of enthalpy variance.

The mass transport by molecular forces is shown in the figures 4.16d, and 4.16e. The contribution by conduction decreases in magnitude as the Pl number is decreased with the decrease in mean temperature in the channel. As optical thickness is lowered for the case abs1, an increase in mass transfer is observed. This occurs around the same location as the increase of temperature fluctuations. The contribution by radiation is given in figure 4.16e. Most notable for this term is the second local maximum for the case abs1, for which temperature fluctuations is the most likely cause.

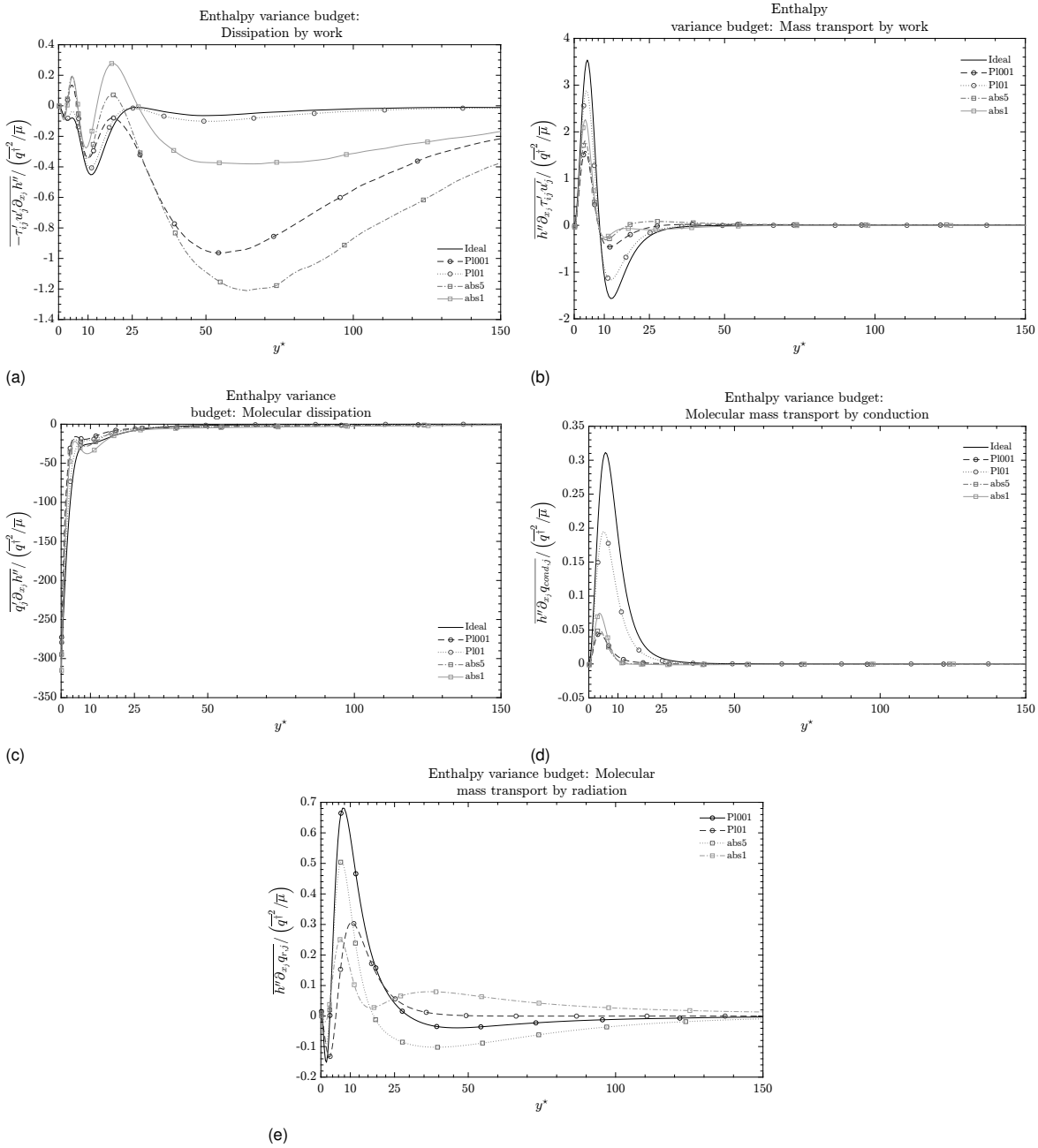

Figure 4.16: (A), Dissipation by work $\overline{u_j' \tau_{ij}' \partial_{x_j} h''}$. (B) Mass transport by work $\overline{h''}\,\overline{\partial_{x_j} \tau_{ij} u_j}$. (C) Molecular dissipation by conduction $\overline{q_j' \partial_{x_j} h''}$. (D) Molecular mass transport by conduction $\overline{h''}\,\overline{\partial_{x_j} q_j}$. (E) Molecular mass transport by radiation $\overline{h''}\,\overline{\partial_{x_j} q_j}$. All normalized by $\overline{q^\dagger}^2/\overline{\mu}$, and as function of $y^\star$.

4.3. Effect of thermal radiation on velocity

Foysi et al. [6] has shown that for flows of higher Ma numbers, the $Re_\tau^\star$ increases. For flows affected by radiation the local Ma number is shown in figure 4.17a to increase with a decreasing optical thickness. It can also be observed that $Re_\tau^\star$ increases in the center of the channel as is visualised in figure 4.17b.

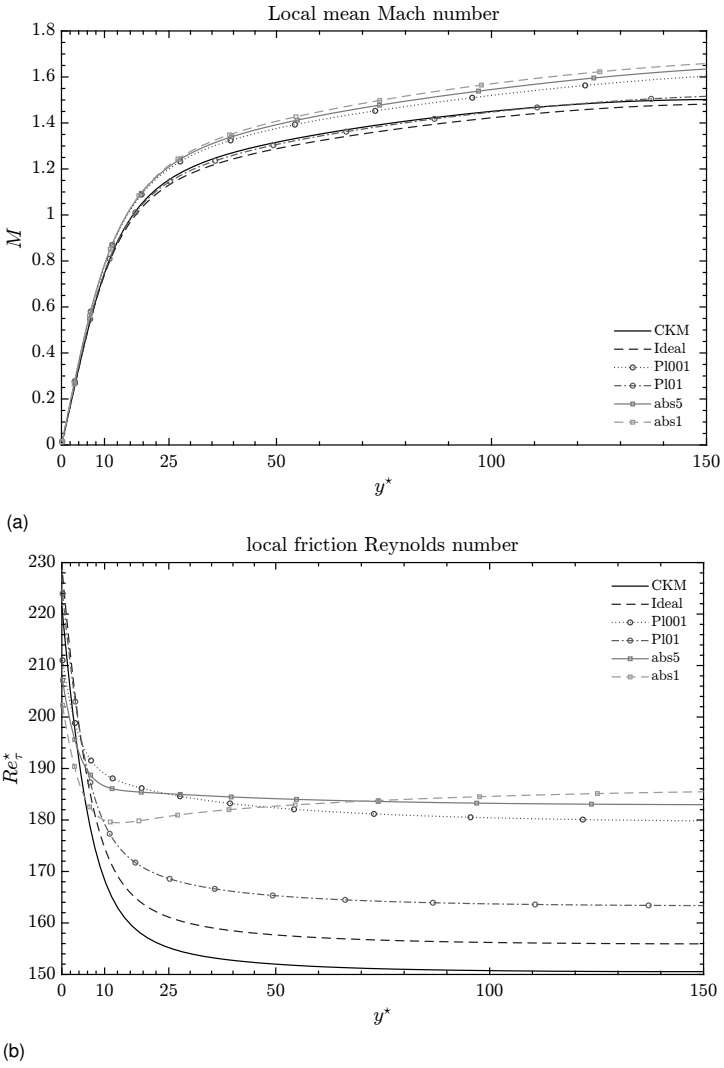

Figure 4.17: (A), Local mean Ma number $\overline{u}/\sqrt{\overline{T}}$. (B) Local friction Reynolds number, $(\rho u_\tau^\star \cdot L)/\mu$, both as a function of $y^\star$.

4.3.1. Kinetic energy budget

The turbulent kinetic energy budget is derived in appendix A and is defined as:

$$\underbrace{-\overline{\rho u_j'' u_i''}\,\widetilde{\frac{\partial u_i}{\partial x_j}}}_{\mathcal{P}} \underbrace{-\overline{\frac{\partial \frac{1}{2}\rho u_j'' u_i'' u_i''}{\partial x_j}}}_{\mathcal{T}_t} \underbrace{-\overline{\frac{\partial u_i'' p'}{\partial x_i}}}_{\mathcal{T}_p} \underbrace{+\overline{\frac{\partial u_i'' \tau_{ij}'}{\partial x_j}}}_{\mathcal{T}_v} \underbrace{+\overline{u_i''}\,\overline{\frac{\partial p}{\partial x_i}}}_{\mathcal{C}_{k1}} \underbrace{+\overline{u_i''}\,\overline{\frac{\partial \tau_{ij}}{\partial x_j}}}_{\mathcal{C}_{k2}} \underbrace{+\overline{p'\frac{\partial u_k''}{\partial x_k}}}_{\mathcal{C}_{k3}} \underbrace{-\overline{\tau_{ij}'\frac{\partial u_i''}{\partial x_j}}}_{\mathcal{D}} = 0\,. \quad (4.13)$$

The individual terms in equation (4.13) denote:

- $\mathcal{P}$, production.
- $\mathcal{T}_p$, pressure transport.
- $\mathcal{T}_t$, turbulent transport.
- $\mathcal{T}_v$, viscous transport.

- $\mathcal{C}_{k1}$, pressure mass transport.
- $\mathcal{C}_{k2}$, viscous mass transport.
- $\mathcal{C}_{k3}$, pressure-velocity coupling.
- $\mathcal{D}$, dissipation.

Turbulent kinetic energy production is shown in figure 4.18a. As the optical thickness is lowered a small increase in production is found. Both turbulent transport and viscous transport (figures 4.18b, and 4.18c) increase as a result of the increase in production as more energy is distributed in the flow. Dissipation (figure 4.19a) shows a clear increase based on the effective radiation transfer. Results are grouped by Pl number, while changing the optical thickness only shows a small, near wall effect. Pressure transport (figure 4.19b) increases in magnitude with the decrease in Pl number. Data for pressure transport after $y^\star = 25$ does not hold value as the graph shows effects of insufficient amount of measurements used to obtain this term. The compressibility term shown in figure 4.19c is written as defined in the works of Morinishi et al. [15]:

$$\begin{aligned}
\mathcal{C}_k &= -\mathcal{C}_1 + \mathcal{C}_2 + \mathcal{C}_3\,, \\
&= -\overline{u_j''}\overline{\frac{\partial p}{\partial x_j}} + \overline{u_i''}\overline{\frac{\partial \tau_{ij}}{\partial x_j}} + \overline{p'\frac{\partial u_k''}{\partial x_k}}\,, \\
&= -\overline{v''}\overline{\frac{\partial p}{\partial y}} + \overline{u_i''}\overline{\frac{\partial \tau_{iy}}{\partial y}} + \overline{p'\frac{\partial u_k''}{\partial x_k}}\,.
\end{aligned} \tag{4.14}$$

Very close to the wall compressibility shows a steep gradient change before it decreases again. The magnitude of compressibility both decreases and moves closer to the wall when comparing the Ideal, Pl01, and Pl001 case. When optical thickness is lowered a reversal of the contribution of compressibility to the turbulent kinetic budget is found.

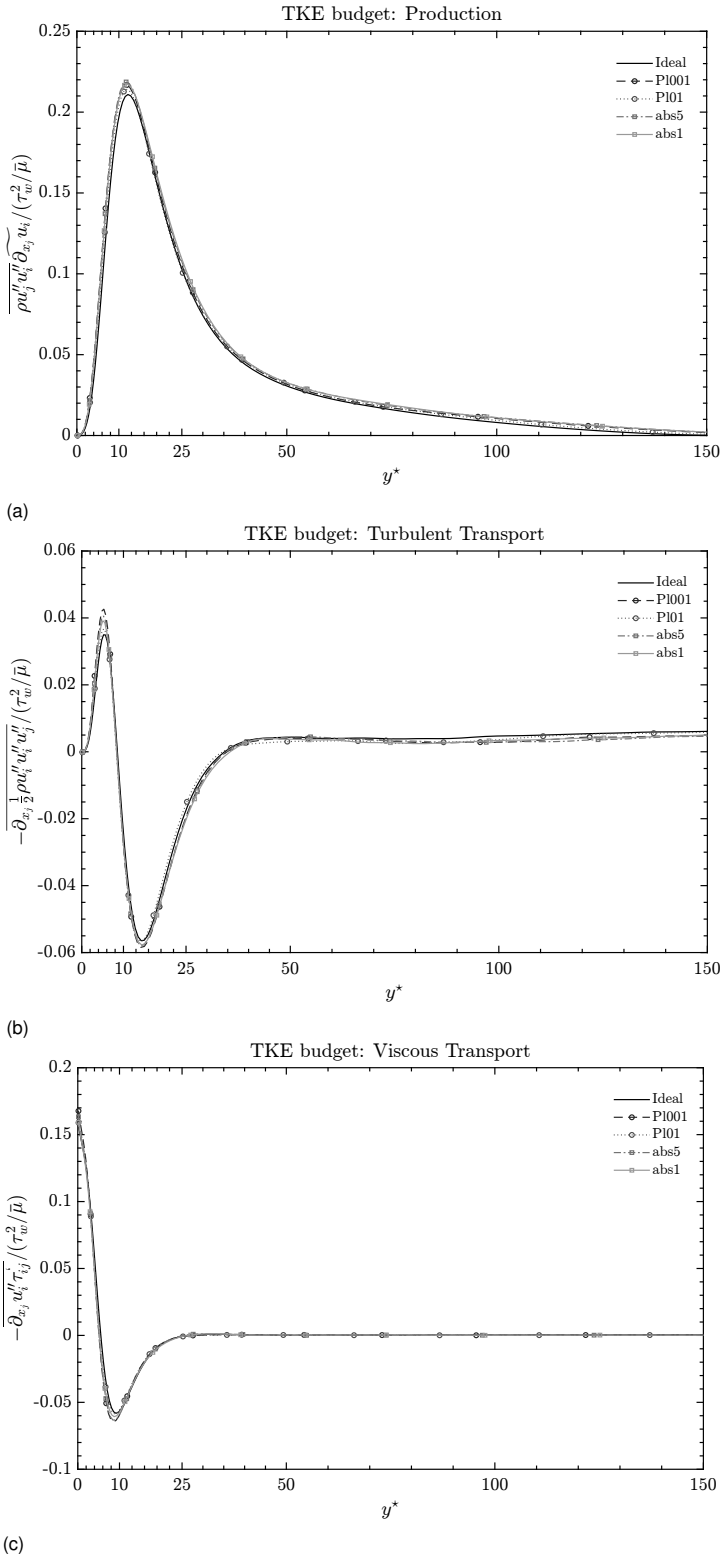

Figure 4.18: (A), Turbulent kinetic energy production. (B) Turbulent transport. (C) Viscous transport. All as a function of $y^\star$ and normalized by $u_\tau{}^\star$.

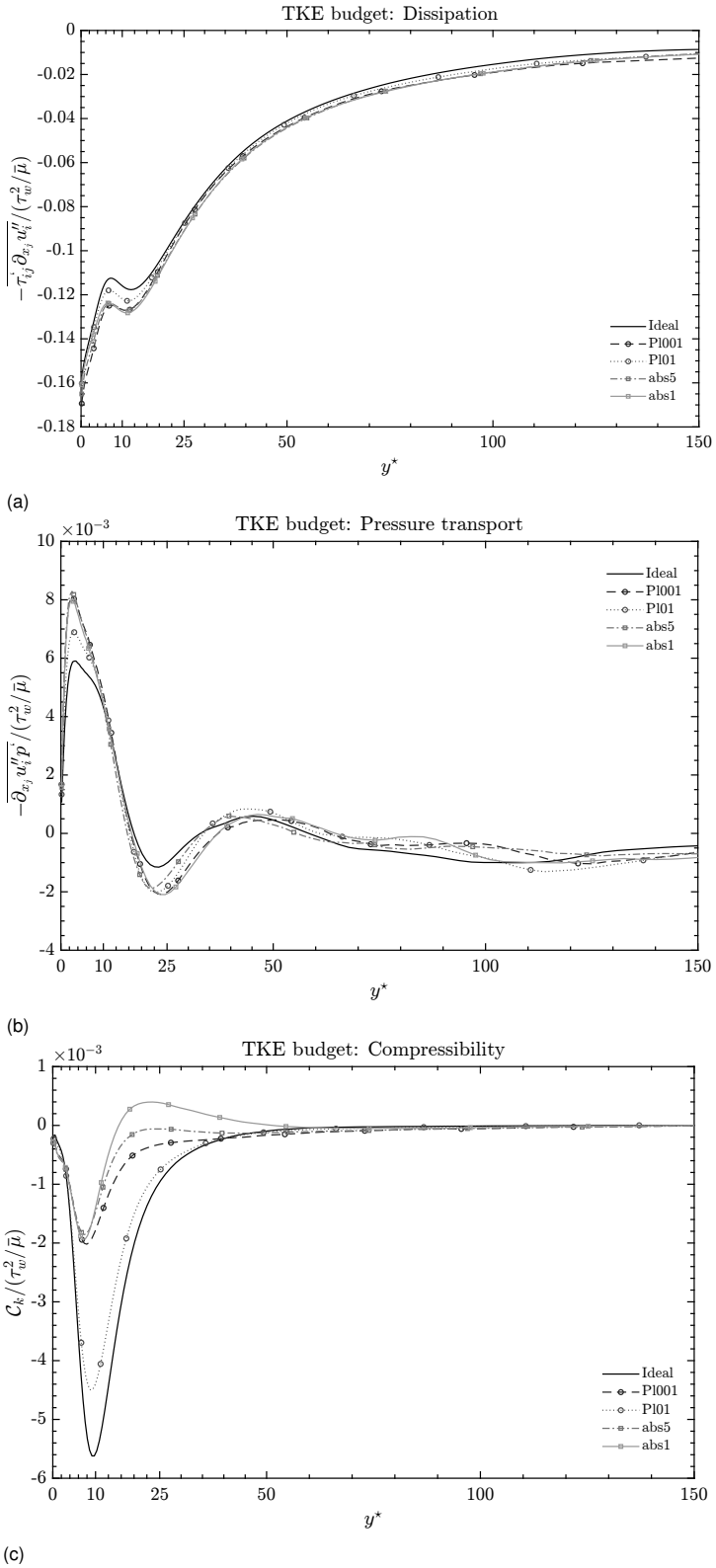

Figure 4.19: (A), Dissipation. (B) Pressure transport. (C) Compressibility. All as a function of $y^\star$ and normalized by ${u_\tau}^\star$.

4.3.2. Thermal energy budgets

The turbulent heat flux budget is derived in appendix A and is defined as:

$$
\begin{aligned}
0 = & \underbrace{-\overline{h''\rho u_j''}\widetilde{\frac{\partial u_j}{\partial x_j}}}_{\mathcal{P}_v} \underbrace{-\overline{\rho u_j'' u_i''}\widetilde{\frac{\partial h}{\partial x_j}}}_{\mathcal{P}_h} - ... \\
& \underbrace{\overline{\frac{\partial \rho u_j'' u_i'' h''}{\partial x_j}}}_{\mathcal{T}_t} \underbrace{-\overline{\frac{\partial p' h''}{\partial x_i}}}_{\mathcal{T}_p} \underbrace{+\overline{\frac{\partial \tau_{ij}' h''}{\partial x_j}}}_{\mathcal{T}_v} \underbrace{+\overline{\frac{\partial \tau_{ij}' u_j' u_i''}{\partial x_j}}}_{\mathcal{T}_w} \underbrace{+\overline{\frac{\partial u_i'' q_j'}{\partial x_j}}}_{\mathcal{T}_q} - ... \\
& \underbrace{\overline{q' \frac{\partial u_i''}{\partial x_j}}}_{\mathcal{D}_q} \underbrace{-\overline{\tau_{ij}' \frac{\partial h''}{\partial x_j}}}_{\mathcal{D}_v} \underbrace{-\overline{\tau_{ij}' u' \frac{\partial u_i''}{\partial x_j}}}_{\mathcal{D}_w} \underbrace{+\overline{p' \frac{\partial h''}{\partial x_i}}}_{\mathcal{D}_p} - ... \\
& \underbrace{\overline{h''}\,\overline{\frac{\partial p}{\partial x_i}}}_{\mathcal{M}_p} \underbrace{+\overline{h''}\,\overline{\frac{\partial \tau_{ij}}{\partial x_j}}}_{\mathcal{M}_v} \underbrace{+\overline{u_i''}\,\overline{\frac{\partial \tau_{ij} u_j}{\partial x_j}}}_{\mathcal{M}_w} \underbrace{+\overline{u_i''}\,\overline{\frac{\partial q_j}{\partial x_j}}}_{\mathcal{M}_q} .
\end{aligned}
\tag{4.15}
$$

The individual terms in equation (4.15) denote:

- $\mathcal{P}_v$, production by velocity.
- $\mathcal{P}_h$, production by enthalpy.
- $\mathcal{T}_t$, turbulent transport.
- $\mathcal{T}_p$, pressure transport.
- $\mathcal{T}_v$, viscous transport.
- $\mathcal{T}_w$, work transport.
- $\mathcal{T}_q$, molecular transport.
- $\mathcal{D}_q$, molecular dissipation.
- $\mathcal{D}_v$, viscous dissipation.
- $\mathcal{D}_w$, dissipation by work.
- $\mathcal{D}_p$, pressure dissipation.
- $\mathcal{M}_p$, mass transport by pressure.
- $\mathcal{M}_v$, viscous mass transport.
- $\mathcal{M}_w$, mass transport by work.
- $\mathcal{M}_q$, molecular mass transport.

Similarly to the budget of enthalpy variation, the heat flux term can be expended into a conduction and a radiation transfer part as shown in equation (4.11).

The budget for turbulent heat flux $\overline{\rho u'' h''}$ is shown term by term, grouped in production, transport, dissipation, and mass transport in the figures 4.20, 4.21, 4.22, and 4.23 respectively. The non-zero production term from this budget, production by enthalpy, takes its shape from the gradient of enthalpy.

Graphs for the turbulent transport and transport by work are shown for completion, but are not discussed as the effects of insufficient averaging is more severe than in previous cases. Viscous transport shown in figure 4.21b shows a steeper gradient for cases with a $Pl = 0.01$. It is also found that the magnitude increases as optical thickness is lowered. Figure 4.21d displays the molecular transport term based on conduction. With temperature fluctuations shifting towards the wall, transport by conduction follows. Both viscous transport and molecular transport show an shift towards the wall. The magnitude of the near wall extremes increases with a decrease in optical thickness. Transport by pressure is shown in figure 4.21e and shows a decrease in gradient in the near wall region for flows with a higher effective radiation transfer.

Dissipation is shown in figures 4.22a till 4.22e. The viscous dissipation and molecular dissipation profiles show similarities in their general shape. Both quantities have a positive maximum close to the wall followed by a minima that increases in magnitude as the optical thickness is lowered. It is notable that when Pl is higher the profile for both quantities closely matches the profile of a case without radiation present. The profile for dissipation by work is shown, but with the remark that the non-normalised quantity is of $\mathcal{O}(10^{-5})$, and can be neglected. Dissipation by pressure shown in figure 4.22d, shows a steep gradient near the wall. It can be seen that the near-wall magnitude is very large compared to production, which is partly due to the normalization used. This can be seen by comparing to a non-normalized profile as shown in figure 4.22e.

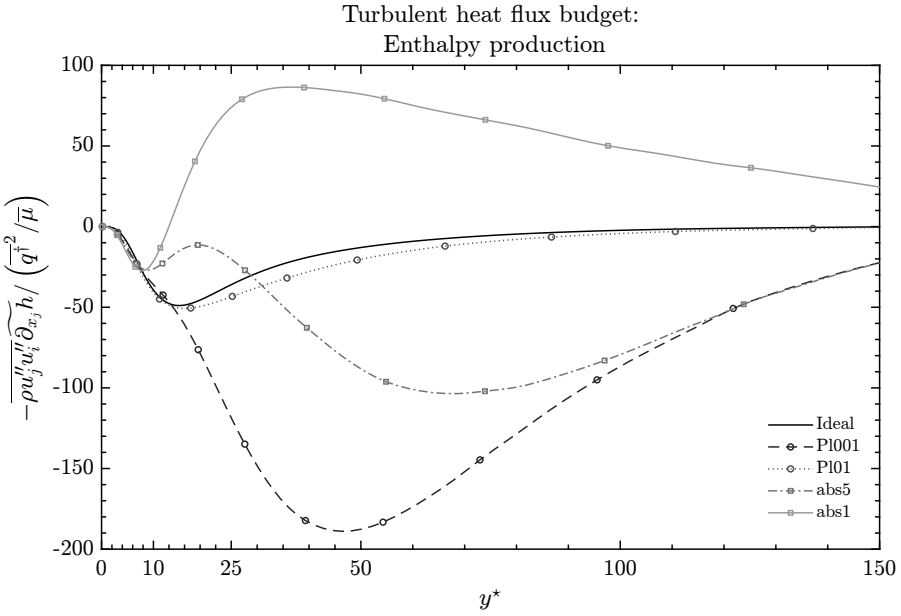

Figure 4.20: Enthalpy production, as function of $y^\star$ and normalized by $\overline{q^\dagger}^2/\overline{\mu}$.

Mass transport terms are shown in the figures 4.23a till 4.23d. Molecular mass transport as shown in figures 4.23a and 4.23b respectively. The results for the cases in which $Pl = 0.01$ for conduction deviate significantly from the Ideal case, for which no good explanation can be found. The results for molecular mass transport by radiation shows results for which it can be questioned if this is shown correctly. Mass transport by pressure is shown in figure 4.23c. As has been shown previously with terms involving pressure, a shift towards the wall is observed in addition to a decrease in magnitude as optical thickness is lowered. For this quantity specifically, it can be shown that as optical thickness is lowered the pressure term takes energy away from the budget, until the optical thickness becomes low enough for denser structures to be ejected as discussed in section 4.1. Mass transport by viscous stress is shown in figure 4.23d. Close to the wall a steep negative gradient is found that decreases as with a decrease in Pl. A decrease in optical thickness increases the magnitude. Mass transport by work is negligible and is not discussed.

The observations from the budgets can be summarised as:

- For turbulent kinetic energy it was found that the terms most affected are dissipation and compressibility. This is likely due to the closer ties with the temperature field via pressure and viscosity. It was found that compressibility decreased with an increase in optical thickness, which is the same trend seen for temperature fluctuations.
- The enthalpy variance budget showed larger changes due to the effect of radiation transfer than the terms of the turbulent kinetic energy budget. Enthalpy variance production shows a large decrease and a shift to the wall as optical thickness is lowered. A increase in production closer to the center of the channel is found for the Pl001 case, which coincides with the shift in maxima for the term $\overline{\rho u'' h''}$. Other terms of the budget move with the production and generally show a shift towards the wall.
- The turbulent heat flux budget production shows a large change in magnitude based on the optical thickness of the flow. The inflection point observed with temperature fluctuations around $y^\star = 11$ is also observable in the production for cases with $Pl = 0.01$. The change in optical thickness also changes the magnitude of the change in gradient around the inflection point at this location.

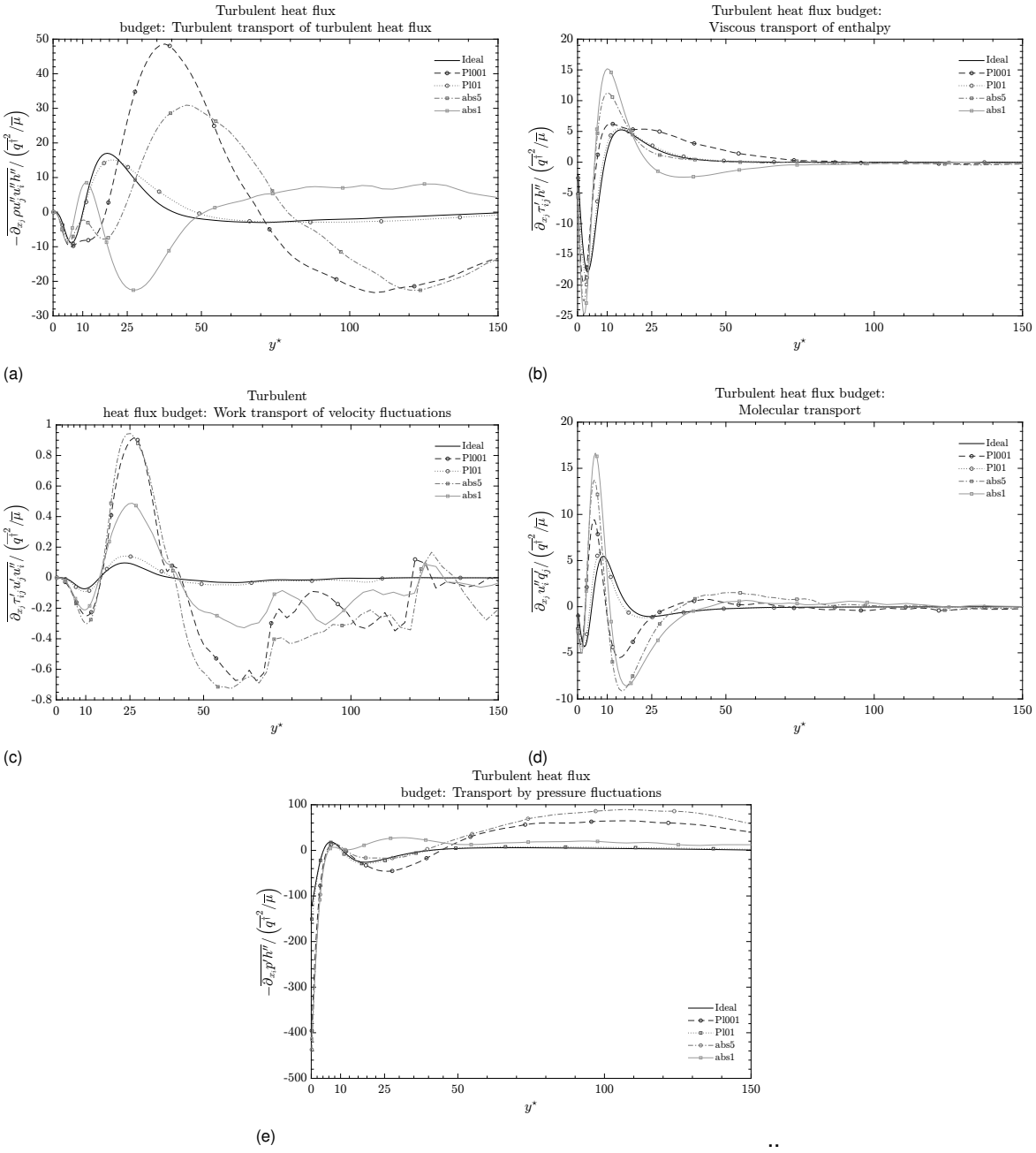

Figure 4.21: (A), Turbulent transport. (B) Viscous transport. (C) Transport by work. (D) Molecular transport by conduction. (E) Pressure transport. All as a function of $y^\star$ and normalized by $\overline{q^\dagger}^2/\overline{\mu}$.

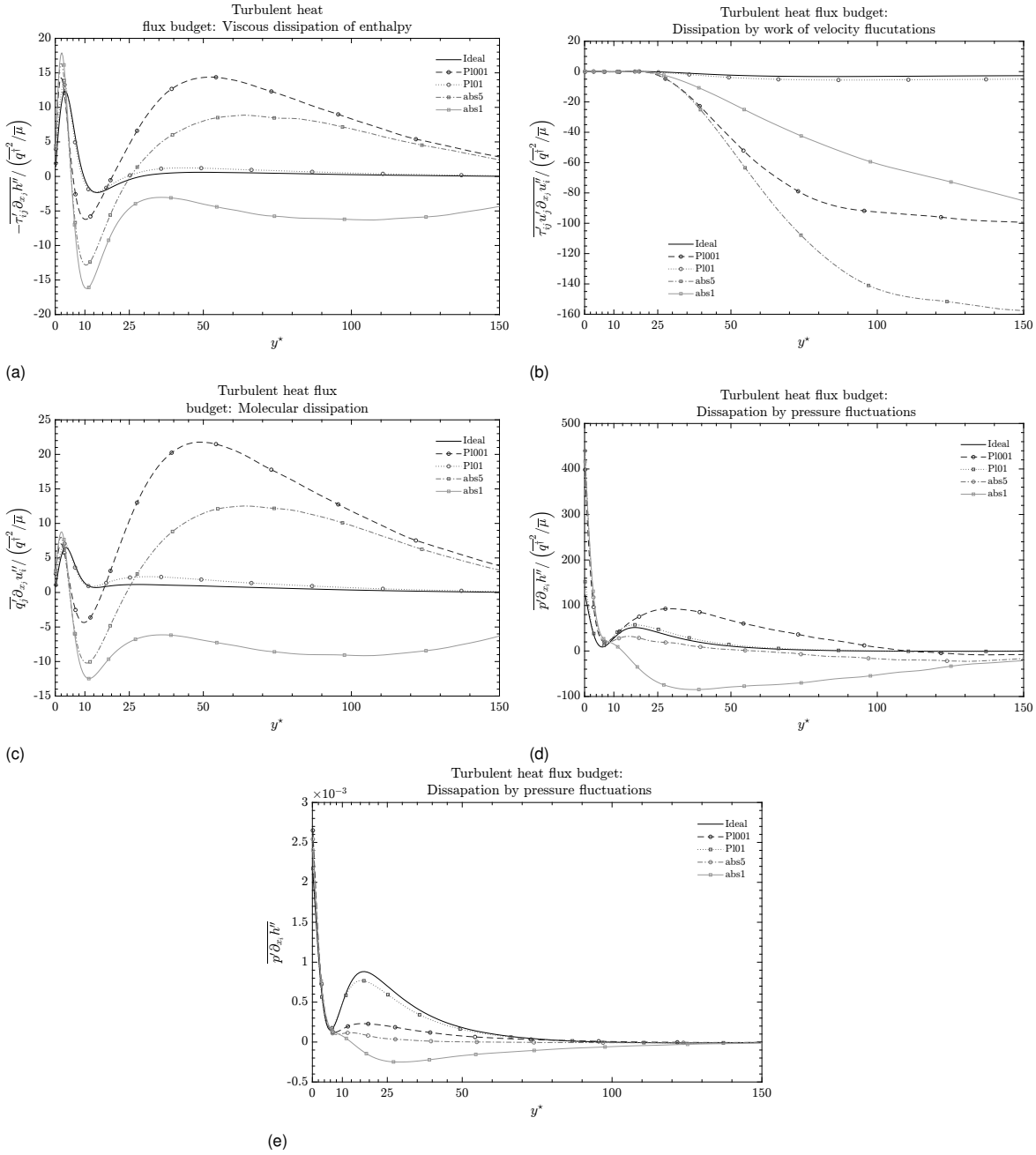

Figure 4.22: (A) Viscous dissipation of enthalpy. (B) Dissipation of velocity by work. (C) Molecular dissipation of enthalpy by conduction. (D) dissipation of enthalpy by pressure. (E) dissipation of enthalpy by pressure. All as a function of $y^\star$, and the figures A till D are normalized by $\overline{q^\dagger}^2/\overline{\mu}$.

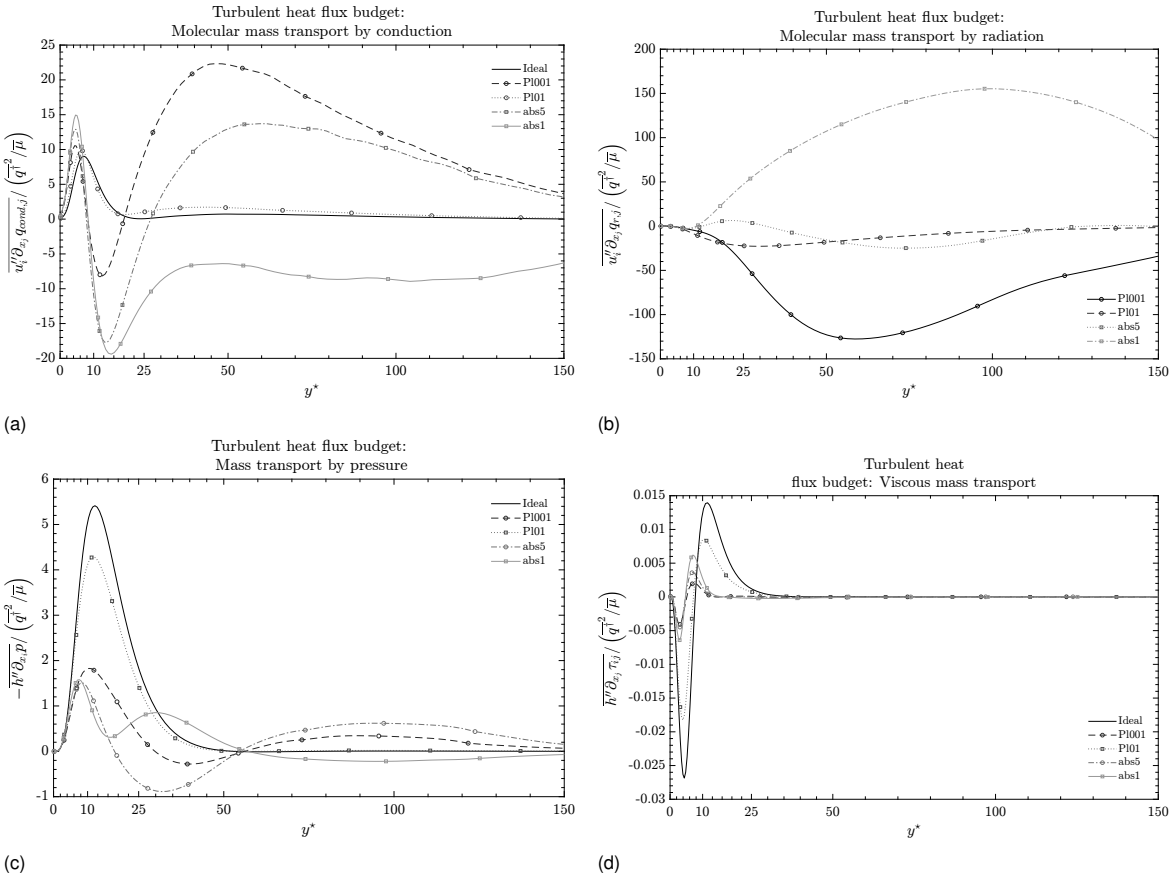

Figure 4.23: (A) Molecular mass transport based on conduction. (B) Molecular mass transport based on radiation. (C) viscous mass transport. (D) mass transport by pressure. All as a function of $y^\star$ and normalized by $\overline{q^\dagger}^2/\overline{\mu}$.

4.4. Effect of thermal radiation on compressibility

As defined previously in equation (4.14) the description for compressibility consists of three terms, of which one has previously been discussed. In figure 4.24 the total compressibility, and the three largest contributors to this total are given. As can be seen from the figures, the largest term in equation (4.14) is $\mathcal{C}_3$. Steeper gradients can be found near the wall for all cases in which radiation transfer occurred, as well as a shift towards the wall for cases with $Pl = 0.01$. This movement towards the wall is consistent with previously mentioned terms and can be linked to the shift by $\mathcal{C}_2$.

The drop in magnitude by radiation can be explained by considering that the viscosity term is directly coupled to the temperature by the closure relation given in equation (3.1). This relation means that the drop observed for mean temperature can be expected to be found in viscosity profile. Similarly it can be expected that the change in gradient as is visualised in figure 4.25 behaves similarly when comparing the different cases. The slope is shown not to change under the effect of radiation, however the gradient does move closer to the wall.

Ghosh et al. [7] discusses the phenomena where the absence of change in Reynolds stress production (as shown in figure 4.18a) in combination with a reduction in streamwise pressure-strain correlation would lead to a reduction of Reynolds stress in streamwise production. As shown in figure 4.26c a reduction in streamwise pressure-strain is found, as well as a reduction in streamwise Reynolds stress figure 4.4c. This energy redistribution can also be seen by the increase in pressure-strain in the other directions, acknowledging that a redistribution of energy takes place from the streamwise direction towards the directions of both span, and wall-normal.

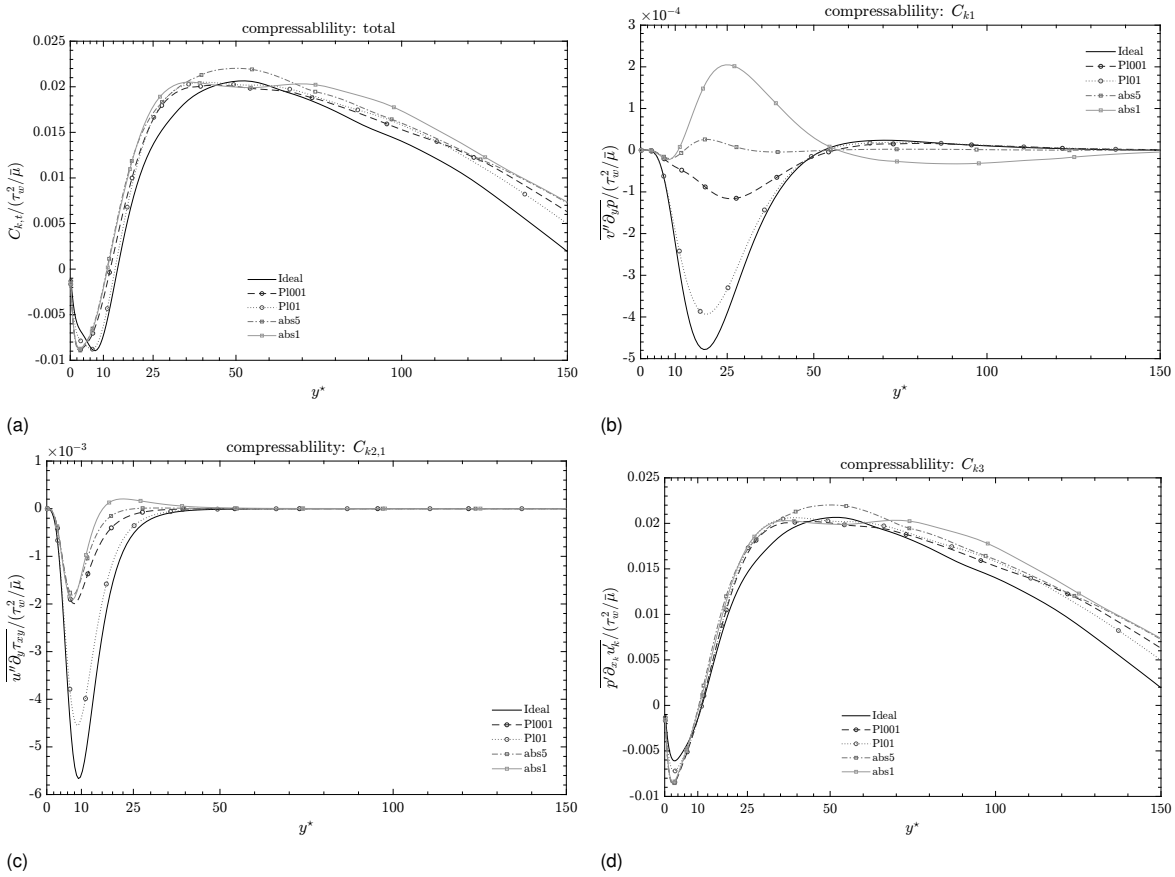

Figure 4.24: (A) Total compressibility $\mathcal{C}_k$, (B) $\mathcal{C}_{1,2}$ (C) $\mathcal{C}_{2,2}$ (D) $\mathcal{C}_3$. All as a function of $y^\star$ and normalized by $\overline{\tau_w}^2/\overline{\mu}$.

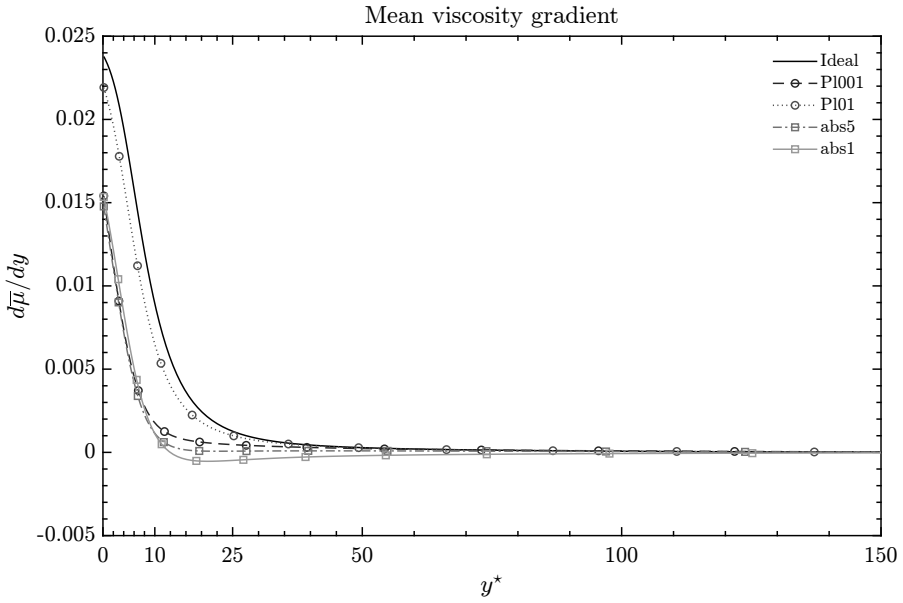

Figure 4.25: Viscosity gradient as function of $y^\star$

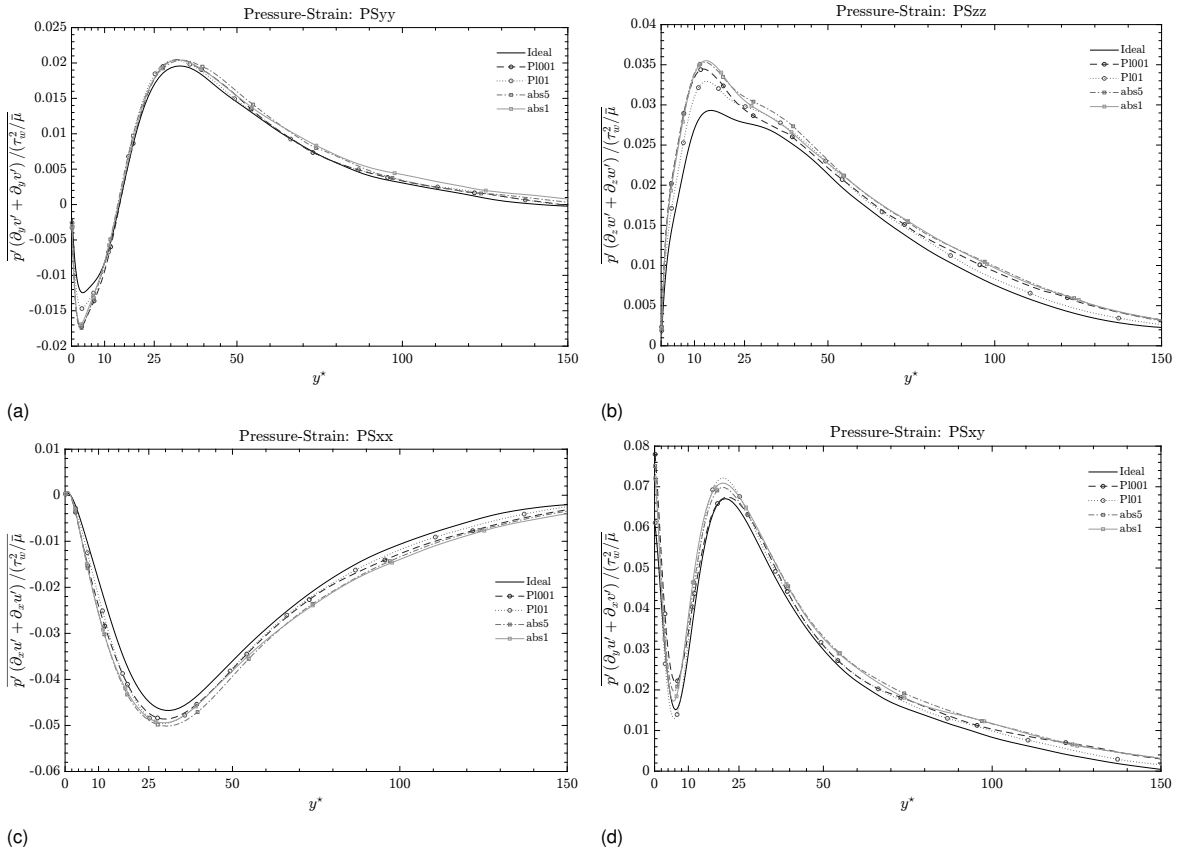

Figure 4.26: Pressure strain (A) PS_{yy}. (B) PS_{zz}. (C) PS_{xx}. (D) PS_{xy}. All as a function of $y^\star$ and normalized by $\overline{\tau_w}^2/\overline{\mu}$.

Shown in the figures 4.27a till 4.27d is the Reynolds stress anisotropy which is defined as:

$$b_{ij} = \overline{\rho u_i'' u_j''} / \overline{\rho u_k'' u_k''} - \delta_{ij}/3\,. \tag{4.16}$$

The wall-normal Reynolds stress anisotropy shown in figure 4.27a shows that the effects of radiation are minimal with the cases abs5, and abs1 shifting a small amount towards an incompressible profile, while the other cases coincide. A larger effect can be observed for spanwise and streamwise direction where a lower Pl number or lower optical thickness moves the profile closer to that of a incompressible case. This increase in Reynolds stress anisotropy has also been observed by Ghosh et al. [7] which was linked to the redistribution of energy by pressure-strain under the effect of radiation.

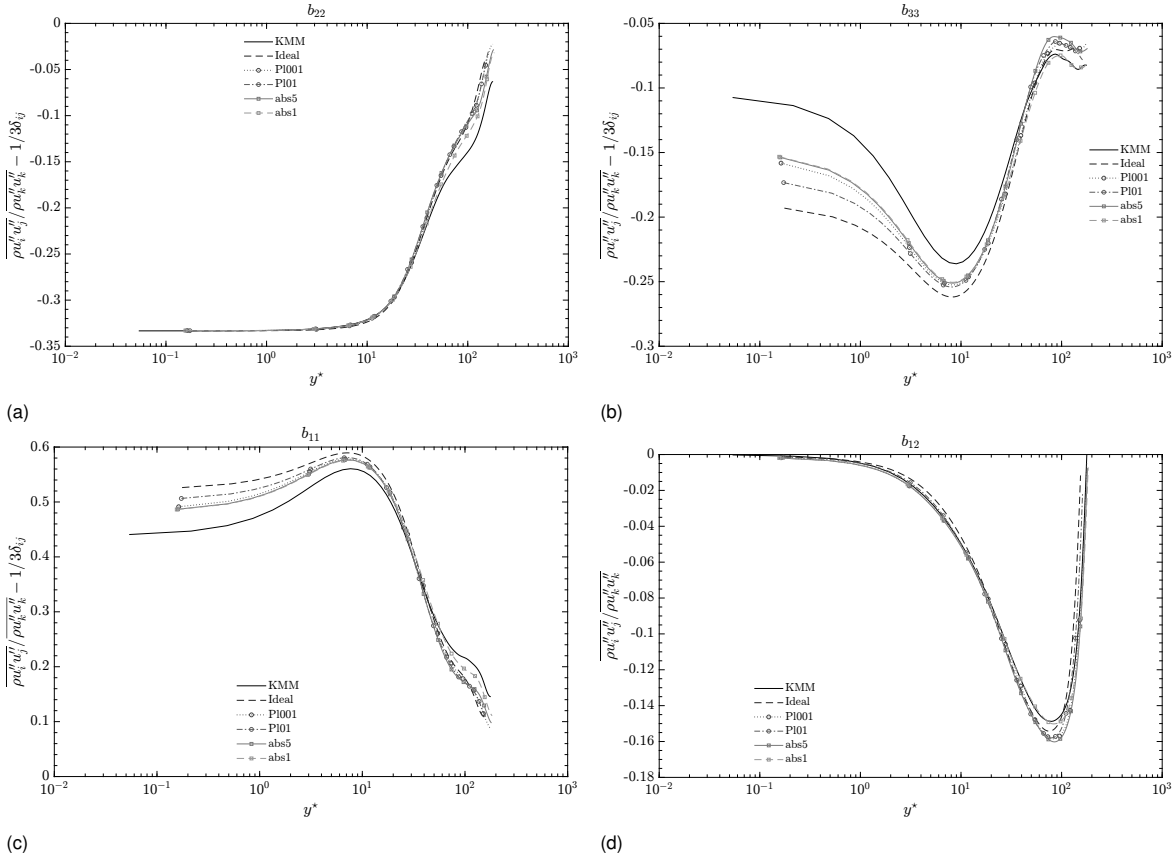

Figure 4.27: Reynolds stress anisotropy (A) b_{22}. (B) b_{33}. (C) b_{11}. (D) b_{12}. Where applicable as function of $y^\star$ and compared to data from Kim et al. [12].

4.5. Modelling thermodynamic quantities

Determining the effect of thermal radiation is computationally expensive. A method of lowering the cost is by utilizing a model that takes in the temperature field and directly gives the resulting fluctuating incident radiation field. This field is more expensive to determine than emission. In recent work by Silvestri et al. [27] a method is proposed that estimates fluctuating radiation quantities to a reasonable degree for incompressible fluids with a high optical thickness.

4.5.1. Approximating fluctuating radiative quantities

Emission fluctuations are defined as:

$$E' = E - \overline{E} \tag{4.17}$$

$$= 4T^4 - \overline{4T^4}\,. \tag{4.18}$$

Substituting in the Reynolds decomposition for temperature to write $f_{E'}$ which is the first order approximation of emission fluctuations,

$$E' = 4\left(T+T'\right)^4 - 4\overline{\left(T+T'\right)^4} \tag{4.19}$$

$$= \left[4\overline{T}^4 + 16\overline{T}^3T' + 24\overline{T}^2T'^2 + 16\overline{T}T'^2 + 4T'^4\right] - ... \left[4\overline{T^4} + 16\overline{T^3}\,\overline{T'} + 24\overline{T^2}\,\overline{T'^2} + 16\overline{T}\,\overline{T'^2} + 4\overline{T'^4}\right] \tag{4.20}$$

$$= 16\overline{T}^3T' + 24\overline{T}^2\left(T'^2 - \overline{T'^2}\right) + 16\overline{T}^2\left(T'^3 - \overline{T'^3}\right) + 4\left(T'^4 - \overline{T'^4}\right) \tag{4.21}$$

$$f_{E'} = 16\overline{T}^3T' \,. \tag{4.22}$$

For a approximating the fluctuating incident radiation first an average length scale for the energy containing temperature structures is to be defined. This length scale is defined as:

$$\omega_c = \left[\underbrace{\left(\frac{\int_0^\infty \omega_x S_T(\omega_x) d\omega_x}{\overline{T'^2}} \right)^2}_{\text{lengthscale in streamwise}} + \underbrace{\left(\frac{\int_0^\infty \omega_z S_T(\omega_z) d\omega_z}{\overline{T'^2}} \right)^2}_{\text{lengthscale in spanwise}} + \underbrace{\left(\frac{\overline{\kappa}}{\log(10)} \right)^2}_{\text{mean radiation path length}} \right]^{\frac{1}{2}} . \tag{4.23}$$

In this equation ω_x and ω_z are wavenumbers in streamwise and spanwise direction respectively, and S_T is the spectrum of temperature fluctuations. This equation can be written with the assumptions that incident radiation fluctuations emerge from an unbounded domain with no walls present and anisotropic temperature structures are only accounted for by the turbulent flow. Doing so allows for Fourier transformation in wall-normal direction. Using ω_c incident radiation fluctuations can be written as:

$$G' \approx G'_* = \frac{\overline{\kappa}}{\omega_c} \arctan\left(\frac{\omega_c}{\overline{\kappa}}\right) f_{E'} \,. \tag{4.24}$$

In figure 4.28 the modelled fluctuating incident radiation is compared to the values obtained from DNS. It can be seen that for the cases in which $\kappa = 10$ reasonable fit is found from $y^\star = 25$ onward. Near the wall the model overestimates the magnitude of G'. As the optical thickness is lowered, the difference between the model and the DNS data becomes larger. This is different from incompressible fluids, where the model has been shown to work for $\kappa = 1$ and up.

The difference between model and DNS does not change significantly when a Favre averaged term or Favre fluctuating term is used in equations (4.23) and (4.24), as shown in figure 4.29. This implies that the problem with the model is more likely caused by the assumptions made for ω_c. Currently it is suspected that the anisotropic temperature structure assumption is most likely not applicable for compressible flows. This assumption is based on the changes found in the compressibility of the fluid which will affect the shape of structures in the inner region. Furthermore the change of sign for density fluctuations, and the coupling with temperature fluctuations by the equation of state is expected to play a role.

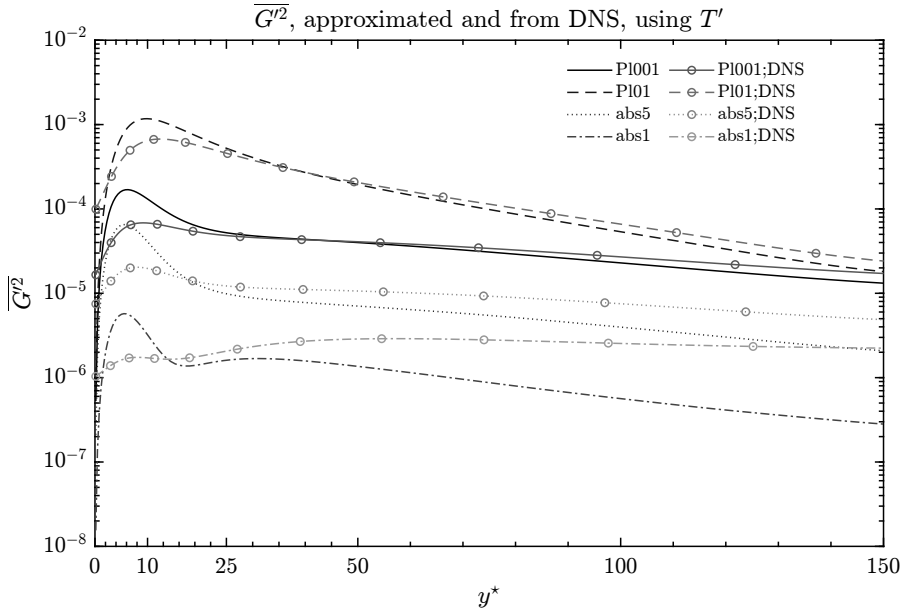

Figure 4.28: A comparison between the modelled fluctuating incident radiation based on temperature fluctuations and those obtained from DNS, as a function of $y^\star$.

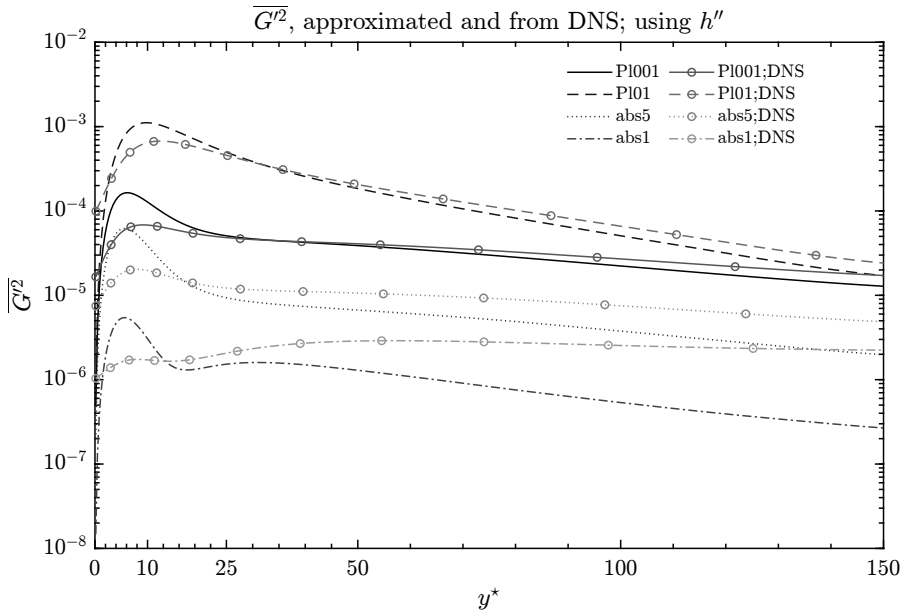

Figure 4.29: A comparison between the modelled fluctuating incident radiation based on enthalpy Favre fluctuations and those obtained from DNS, as a function of $y^\star$.

5

Conclusion and recommendations

5.1. Conclusion

In this thesis, a study of the effects of thermal radiation on a compressible turbulent channel flow has been performed. The effect on the temperature and density field for varying levels of effective thermal radiation transfer and optical thickness have been shown within a fictitious grey-gas. The results show that when optical thickness is varied, trends in behaviour can be shown to exist for various quantities.

It was found that under circumstances where thermal radiation is of high relevance and the flow is of a low Pl number, cold, denser turbulent structures are ejected away from the wall if the optical thickness is low enough. With this phenomena it was found that quantities affected by density fluctuations change sign, changing the behaviour of terms in budgets such as the creation of a region where compressibility adds to the turbulent kinetic energy budget.
The results found by Ghosh et al. [7] regarding the change in compressibility due to the effects of thermal radiation in optically thin flows were found to be present in optically thick flows. For incident radiation, emission, and their combination radiative power, phenomena described by Silvestri [24] for optically thick incompressible flow, were found to show similarities with the behavioural trends in compressible flow.

It has been shown that the model used to approximate incident radiation fluctuations in incompressible turbulent flow does not give the desired result. For high optical thickness ($\zeta = 10$) a reasonable approximation is found, while for flow with a lower optical thickness ($\zeta = 1$) a large over-prediction is found near the wall, and an under-prediction in the channel centre. This is likely due to the assumption made for the temperature structures in the inner layer of the flow.
While this assumption is needed in the derivation of the model, it is the author's believe that due to compressibility this assumption is too great and no longer valid. This is supported with the change in the compressibility terms due to TRI.

5.2. Recommendations

The results obtained during this study are largely discussed from a top-level perspective. An in-depth research in which 2-point correlations and spectra are used to describe the relation between TRI, and thermal and velocity structures is recommended. It is also recommended that the assumptions used to derive the model for fluctuating radiation quantities in incompressible flows are re-evaluated if the model were to be adapted for compressible flows.
Furthermore, it was found that the scaling of quantities in this study was not without problems. Scaling provided by literature does not always give the desired result of a near collapse of the data. It is therefore recommended to look into a method of scaling non-local properties.

A

Derivation of the turbulent energy budgets

Several turbulent budgets are to be derived: turbulent heat flux $\partial_t \overline{\rho u'' h''}$, turbulent kinetic energy $\partial_t \overline{\rho u''^2}$, and temperature variance $\partial_t \overline{\rho h''^2}$. In this chapter the derivations of these budgets are discussed.

As the governing equations describe a compressible flow, both Reynolds averaging and Favre averaging is used. For the derivations of the budgets the following rules are used:

1. Start from the non-conservative forms of the conservation equations.
2. Favre average as: $u = \widetilde{u} + u''$,
3. Reynolds average as: $\phi = \bar{\phi} + \phi'$,
4. $\overline{\rho u''} = 0$, and $\overline{\phi'} = 0$,
5. $\partial (a \cdot b \cdot c) = a \cdot b \partial (c) + a \cdot c \partial (b) + b \cdot c \partial (a)$,
6. $a \partial (b) = \partial (a \cdot b) - b \partial (a)$,

The procedure for deriving one of the budgets listed above, which have the form $\overline{\rho x'' y''}$, one starts from:

$$\overline{x" \cdot \mathrm{CE}(\rho y) + y'' \cdot \mathrm{CE}(\rho x) + x'' y'' \cdot \mathrm{CE}(\rho)}\,. \tag{A.1}$$

In which CE stands for conservation equation. The budget equation for turbulent heat flux for example requires using the conservation of momentum, energy (in enthalpy form), and continuity.

A.1. Thermal heat flux budget

Starting point for the derivation of the budget is the non-conservative form of the momentum, energy, and mass conservation equations, and multiplied with fluctuating terms to obtain the form as shown in equation (A.1). The conservation equations are shown in equation (A.2), and are in for top to bottom the mass, momentum, and energy conservation equation.

$$\begin{aligned} & h'' u_i'' \cdot \left(\frac{\partial \rho}{\partial t} + \frac{\partial \rho u_j}{\partial x_j} \right), \\ & h'' \cdot \left(\frac{\partial \rho u_i}{\partial t} + \frac{\partial \rho u_j u_i}{\partial x_j} + \frac{\partial p \delta_{ij}}{\partial x_j} - \frac{\partial \tau_{ij}}{\partial x_j} \right), \\ & u_i'' \cdot \left(\frac{\partial \rho h}{\partial t} + \frac{\partial \rho u_j h}{\partial x_j} + \frac{\partial q}{\partial x_j} - \frac{\partial \tau_{ij} u_j}{\partial x_j} \right). \end{aligned} \tag{A.2}$$

Starting with the temporal derivative in the thermal heat flux budget, the multiplication as shown in

equation (A.1) is written as:

$$\overline{\underbrace{u_i'' h'' \cdot \frac{\partial \rho}{\partial t}}_{\text{continuity}} + \underbrace{\rho h'' \cdot \frac{\partial (\widetilde{u_i} + u_i'')}{\partial t}}_{\text{momentum}} + \underbrace{\rho u_i'' \cdot \frac{\partial (\widetilde{h} + h'')}{\partial t}}_{\text{energy}}} .$$

When the partial derivatives are expended the terms containing a quantity that is Favre averaged drops to zero as per rule 4. The term remaining are:

$$\overline{u_i'' h'' \cdot \frac{\partial \rho}{\partial t}} + \overline{\rho h'' \cdot \frac{\partial u_i''}{\partial t}} + \overline{\rho u_i'' \cdot \frac{\partial h''}{\partial t}} = \overline{\frac{\partial \rho h'' u_i''}{\partial t}} .$$

These remaining terms can as shown above be rewritten as per rule 5.

The advection term starts by writing the terms in the form of eqaution (A.1), and expanding the terms as per rule 2:

$$\overline{\underbrace{u_i'' h'' \cdot \frac{\partial \rho (\widetilde{u_j} + u_j'')}{\partial x_j}}_{\text{continuity}} + \underbrace{\rho (\widetilde{u_j} + u_j'') h'' \cdot \frac{\partial (\widetilde{u_i} + u_i'')}{\partial x_j}}_{\text{momentum}} + \underbrace{\rho (\widetilde{u_j} + u_j'') u_i'' \cdot \frac{\partial (\widetilde{h} + h'')}{\partial x_j}}_{\text{energy}}} .$$

Expanding all the terms results in:

$$\begin{aligned}
&\overline{h'' \rho \left(\widetilde{u_j} + u_j''\right) \frac{\partial \left(\widetilde{u_i} + u_i''\right)}{\partial x_j} + u_i'' \rho \left(\widetilde{u_j} + u_j''\right) \frac{\partial \left(\widetilde{h} + h''\right)}{\partial x_j} + h'' u_j'' \frac{\partial \left(\rho \widetilde{u_j} + u_j''\right)}{\partial x_j}} \\
&= \underbrace{\overline{h'' \rho \widetilde{u_j} \frac{\partial \widetilde{u_i}}{\partial x_j}}}_{1} + \underbrace{\overline{h'' \rho \widetilde{u_j} \frac{\partial u_i''}{\partial x_j}}}_{2} + \underbrace{\overline{h'' \rho u_j'' \frac{\partial \widetilde{u_i}}{\partial x_j}}}_{3} + \underbrace{\overline{h'' \rho u_j'' \frac{\partial u_i''}{\partial x_j}}}_{4} + \ldots \\
&\quad \underbrace{\overline{u_i'' \rho \widetilde{u_j} \frac{\partial \widetilde{h}}{\partial x_j}}}_{5} + \underbrace{\overline{u_i'' \rho \widetilde{u_j} \frac{\partial h''}{\partial x_j}}}_{6} + \underbrace{\overline{u_i'' \rho u_j'' \frac{\partial \widetilde{h}}{\partial x_j}}}_{7} + \underbrace{\overline{u_i'' \rho u_j'' \frac{\partial h''}{\partial x_j}}}_{8} + \ldots \\
&\quad \underbrace{\overline{h'' u_i'' \frac{\partial \rho \widetilde{u_j}}{\partial x_j}}}_{9} + \underbrace{\overline{h'' u_i'' \frac{\partial \rho u_j''}{\partial x_j}}}_{10} = \\
&= \underbrace{\overline{\frac{\partial u_i'' h'' u_j''}{\partial x_j}}}_{4,8,10} + \underbrace{\overline{\frac{\partial u_i'' h'' \rho \widetilde{u_j}}{\partial x_j}}}_{2,6,9} + \underbrace{\overline{h'' \rho u_j'' \frac{\partial \widetilde{u_i}}{\partial x_j}}}_{3} + \underbrace{\overline{u_i'' \rho u_j'' \frac{\partial \widetilde{h}}{\partial x_j}}}_{7} .
\end{aligned} \tag{A.3}$$

The terms numbered 1 and 5 are zero as per rule 4. The term resulting from combining 2, 6, and 9 is part of the material derivative of the budget term that is derived here and is equal to 0. With the left hand side derived, the four terms on the right side remain. Which are pressure:

$$\begin{aligned}
&-\overline{h'' \frac{\partial \left(\overline{p} + p'\right)}{\partial x_j}} \\
&\quad = -\overline{\frac{\partial h'' p}{\partial x_i}} + p \overline{\frac{\partial h''}{\partial x_i}} - \overline{\frac{\partial p' h''}{\partial x_i}} + p' \overline{\frac{\partial h''}{\partial x_i}} .
\end{aligned} \tag{A.4}$$

viscous stress:

$$\begin{aligned}
&\overline{h'' \frac{\partial \left(\overline{\tau_{ij}} + \tau_{ij}'\right)}{\partial x_j}} \\
&\quad = \overline{\frac{\partial \overline{\tau_{ij}} h''}{\partial x_j}} - \overline{\tau_{ij} \frac{\partial h''}{\partial x_j}} + \overline{\frac{\partial \tau_{ij}' h''}{\partial x_j}} - \overline{\tau_{ij}' \frac{\partial h}{\partial x_j}''} .
\end{aligned} \tag{A.5}$$

work:

$$\begin{aligned}&\overline{u_i''\frac{\partial\left(\overline{\tau_{ij}}+\tau_{ij}'\right)\left(\overline{u_j}+u_j'\right)}{\partial x_j}}\\=&\frac{\partial\overline{\tau_{ij}u_ju_i''}}{\partial x_j}-\overline{\tau_{ij}u_j\frac{\partial u_i''}{\partial x_j}}+\overline{\frac{\partial\tau_{ij}'u_j'u_i'}{\partial x_j}}-\overline{\tau_{ij}'u_j'\frac{\partial u_i''}{\partial x_j}}\,.\end{aligned}\tag{A.6}$$

and thermal flux:

$$\begin{aligned}&\overline{u_i''\frac{\partial\left(\overline{q_j}+q_j'\right)}{\partial x_j}}\\&=\overline{\frac{\partial u_i''q_j'}{\partial x_j}}-\overline{q_j'\frac{\partial u_i''}{\partial x_j}}+\overline{u''}\,\overline{\frac{\partial q_j}{\partial x_j}}\,.\end{aligned}\tag{A.7}$$

For all four terms listed above rule 5 is applied. When all components of the budget are combined the following is found:

$$\begin{aligned}0=&\underbrace{-\overline{h''\rho u_j''}\,\widetilde{\frac{\partial u_j}{\partial x_j}}}_{\mathcal{P}_v}-\underbrace{\overline{\rho u_j''u_i''}\,\widetilde{\frac{\partial h}{\partial x_j}}}_{\mathcal{P}_h}-...\\&\underbrace{\overline{\frac{\partial\rho u_j''u_i''h''}{\partial x_j}}}_{\mathcal{T}_t}-\underbrace{\overline{\frac{\partial p'h''}{\partial x_i}}}_{\mathcal{T}_p}+\underbrace{\overline{\frac{\partial\tau_{ij}'h''}{\partial x_j}}}_{\mathcal{T}_v}+\underbrace{\overline{\frac{\partial\tau_{ij}'u_j'u_i''}{\partial x_j}}}_{\mathcal{T}_w}+\underbrace{\overline{\frac{\partial u_i''q_j'}{\partial x_j}}}_{\mathcal{T}_q}-...\\&\underbrace{\overline{q'\frac{\partial u_i''}{\partial x_j}}}_{\mathcal{D}_q}-\underbrace{\overline{\tau_{ij}'\frac{\partial h''}{\partial x_j}}}_{\mathcal{D}_v}-\underbrace{\overline{\tau_{ij}'u'\frac{\partial u_i''}{\partial x_j}}}_{\mathcal{D}_w}+\underbrace{\overline{p'\frac{\partial h''}{\partial x_i}}}_{\mathcal{D}_p}-...\\&\underbrace{\overline{h''}\,\overline{\frac{\partial p}{\partial x_i}}}_{\mathcal{M}_p}+\underbrace{\overline{h''}\,\overline{\frac{\partial\tau_{ij}}{\partial x_j}}}_{\mathcal{M}_v}+\underbrace{\overline{u_i''}\,\overline{\frac{\partial\tau_{ij}u_j}{\partial x_j}}}_{\mathcal{M}_w}+\underbrace{\overline{u_i''}\,\overline{\frac{\partial q_j}{\partial x_j}}}_{\mathcal{M}_q}\,.\end{aligned}\tag{A.8}$$

The individual terms in equation (A.8) denote:

- $\mathcal{P}_v$, production by velocity.
- $\mathcal{P}_h$, production by enthalpy.
- $\mathcal{T}_t$, turbulent transport.
- $\mathcal{T}_p$, pressure transport.
- $\mathcal{T}_v$, viscous transport.
- $\mathcal{T}_w$, work transport.
- $\mathcal{T}_q$, molecular transport.
- $\mathcal{D}_q$, molecular dissipation.
- $\mathcal{D}_v$, viscous dissipation.
- $\mathcal{D}_w$, dissipation by work.
- $\mathcal{D}_p$, pressure dissipation.
- $\mathcal{M}_p$, mass transport by pressure.
- $\mathcal{M}_v$, viscous mass transport.
- $\mathcal{M}_w$, mass transport by work.
- $\mathcal{M}_q$, molecular mass transport.

A.2. Thermal variance budget

The budget for thermal variance is derived using the conservation equations for mass, and two equations for energy and multiplying it with the terms to obtain $\rho h'' h''$:

$$\begin{aligned} & h''h'' \cdot \left(\frac{\partial \rho}{\partial t} + \frac{\partial \rho u_j}{\partial x_j} \right) , \\ & h'' \cdot \left(\frac{\partial \rho h}{\partial t} + \frac{\partial \rho u_j h}{\partial x_j} + \frac{\partial q}{\partial x_j} - \frac{\partial \tau_{ij} u_j}{\partial x_j} \right) , \\ & h'' \cdot \left(\frac{\partial \rho h}{\partial t} + \frac{\partial \rho u_j h}{\partial x_j} + \frac{\partial q}{\partial x_j} - \frac{\partial \tau_{ij} u_j}{\partial x_j} \right) . \end{aligned} \tag{A.9}$$

Starting from the temporal derivative it can be written for enthalpy variance, the multiplication as shown in A.1 is written as:

$$\overline{\underbrace{h''h'' \cdot \frac{\partial \rho}{\partial t}}_{\text{continuity}} + \underbrace{\rho h'' \cdot \frac{\partial (\widetilde{h} + h'')}{\partial t}}_{\text{energy}} + \underbrace{\rho h'' \cdot \frac{\partial (\widetilde{h} + h'')}{\partial t}}_{\text{energy}}} .$$

When the partial derivatives are expended, the terms containing a quantity that is Favre averaged drops to zero as per rule 4. The term remaining are rewritten using rule 5:

$$\overline{h''h'' \cdot \frac{\partial \rho}{\partial t}} + \overline{\rho h'' \cdot \frac{\partial h''}{\partial t}} + \overline{\rho h'' \cdot \frac{\partial h''}{\partial t}} = \overline{\frac{\partial \rho h'' h''}{\partial t}} .$$

The advection term starts by writing the terms in the form of equation (A.1), and expanding the terms as per rule 2:

$$\overline{\underbrace{\rho(\widetilde{u_j} + u_j'')h'' \cdot \frac{\partial (\widetilde{h} + h'')}{\partial x_j}}_{\text{energy}} + \underbrace{\rho(\widetilde{u_j} + u_j'')h'' \cdot \frac{\partial (\widetilde{h} + h'')}{\partial x_j}}_{\text{energy}} + \underbrace{h''h'' \cdot \frac{\partial \rho(\widetilde{u_j} + u_j'')}{\partial x_j}}_{\text{continuity}}} .$$

Expanding all the terms results in:

$$\begin{aligned} & \overline{\rho(\widetilde{u_j} + u_j'')h'' \cdot \frac{\partial (\widetilde{h} + h'')}{\partial x_j} + \rho(\widetilde{u_j} + u_j'')h'' \cdot \frac{\partial (\widetilde{h} + h'')}{\partial x_j} + h''h'' \cdot \frac{\partial \rho(\widetilde{u_j} + u_j'')}{\partial x_j}} \\ & = \underbrace{\overline{\rho \widetilde{u_j} h'' \frac{\partial h''}{\partial x_j}}}_{1} + \underbrace{\overline{\rho u_j'' \frac{\partial h''}{\partial x_j}}}_{2} + \underbrace{\overline{\rho u_j'' \frac{\partial \widetilde{h}}{\partial x_j}}}_{3} + ... \\ & \quad \underbrace{\overline{\rho \widetilde{u_j} h'' \frac{\partial h''}{\partial x_j}}}_{4} + \underbrace{\overline{\rho u_j'' \frac{\partial h''}{\partial x_j}}}_{5} + \underbrace{\overline{\rho u_j'' \frac{\partial \widetilde{h}}{\partial x_j}}}_{6} + ... \\ & \quad \underbrace{\overline{h''h'' \frac{\partial \rho \widetilde{u_j}}{\partial x_j}}}_{7} + \underbrace{\overline{h''h'' \frac{\partial \rho u_j''}{\partial x_j}}}_{8} \\ & = \underbrace{\overline{\frac{\partial \rho \widetilde{u_j} h'' h''}{\partial x_j}}}_{1,4,7} + \underbrace{\overline{\frac{\partial \rho u_j'' h'' h''}{\partial x_j}}}_{2,5,8} + \underbrace{\overline{2 \rho u_j'' h''} \widetilde{\frac{\partial h}{\partial x_j}}}_{3,6} . \end{aligned} \tag{A.10}$$

During the steps shown in equation (A.10) the terms resulting in 0 due to rule 3 have been left out. The terms 1, 4, and 7 can be combined by rule 4 as can be done for the terms annotated 2, 5, and 8. The

term created by combining 1,4, and 7 is part of the material derivative of the budget and together with the temporal component derived previously results in a 0.
The RHS terms from both energy equations, work and thermal flux can be expended next by:

$$\begin{aligned}&\overline{2\,h''\frac{\partial\left(\overline{\tau_{ij}}+\tau'_{ij}\right)\left(\overline{u_j}+u'_j\right)}{\partial x_j}}\\ =&2\left[\overline{h''}\frac{\partial\overline{u_j\tau_{ij}}}{\partial x_j}+\overline{\frac{\partial h''u'_j\tau'_{ij}}{\partial x_j}}-\overline{u'_j\tau'_{ij}\frac{\partial h''}{\partial x_j}}\right].\end{aligned} \tag{A.11}$$

$$\begin{aligned}&\overline{2\,h''\frac{\partial\left(\overline{q_j}+q'_j\right)}{\partial x_j}}\\ =&\,2\left[\overline{\frac{\partial h''_i q'_j}{\partial x_j}}-\overline{q'_j\frac{\partial h''}{\partial x_j}}+\overline{h''}\,\overline{\frac{\partial q_j}{\partial x_j}}\right].\end{aligned} \tag{A.12}$$

Combining all terms, and dividing by 2 gives the enthalpy variance budget:

$$\underbrace{-\overline{\rho u''_j h''}\,\widetilde{\frac{\partial h}{\partial x_j}}}_{\mathcal{P}}+\underbrace{\frac{\partial\overline{h''u'_j\tau'_{ij}}}{\partial x_j}}_{\mathcal{T}_w}+\underbrace{\frac{\partial\overline{h''q_j}}{\partial x_j}}_{\mathcal{T}_q}-\underbrace{\frac{\partial\overline{\frac{1}{2}\rho u''_j h''h''}}{\partial x_j}}_{\mathcal{T}_t}+\underbrace{\overline{h''}\,\overline{\frac{\partial\tau_{ij}u_j}{\partial x_j}}}_{\mathcal{M}_w}+\underbrace{\overline{h''}\,\overline{\frac{\partial q_j}{\partial x_j}}}_{\mathcal{M}_q}-\underbrace{\overline{u'_j\tau'_{ij}\frac{\partial h''}{\partial x_j}}}_{\mathcal{D}_w}-\underbrace{\overline{q'_j\frac{\partial h''}{\partial x_j}}}_{\mathcal{D}_q}=0\,. \tag{A.13}$$

The individual terms in equation (A.13) denote:

- $\mathcal{P}$, production.
- $\mathcal{T}_w$, transport by work fluctuations.
- $\mathcal{T}_q$, molecular diffusion.
- $\mathcal{T}_t$, transport by turbulent fluctuations.
- $\mathcal{M}_w$, mass transport by work.
- $\mathcal{M}_q$, molecular mass transport.
- $\mathcal{D}_w$, dissipation by work fluctuations.
- $\mathcal{D}_q$, molecular dissipation.

A.3. Turbulent kinetic energy budget

The budget for turbulent kinetic energy is derived using the conservation equations for mass, and two times the equation for momentum and multiplying it with the terms to obtain $\rho u''_i u''_i$:

$$\begin{aligned}&u''_i u''_j\cdot\left(\frac{\partial\rho}{\partial t}+\frac{\partial\rho u_j}{\partial x_j}\right),\\ &u''_i\cdot\left(\frac{\partial\rho u_i}{\partial t}+\frac{\partial\rho u_j u_i}{\partial x_j}+\frac{\partial p\delta_{ij}}{\partial x_j}-\frac{\partial\tau_{ij}}{\partial x_j}\right),\\ &u''_j\cdot\left(\frac{\partial\rho u_i}{\partial t}+\frac{\partial\rho u_j u_i}{\partial x_j}+\frac{\partial p\delta_{ij}}{\partial x_j}-\frac{\partial\tau_{ij}}{\partial x_j}\right).\end{aligned} \tag{A.14}$$

Starting from the temporal derivative it can be written for turbulent kinetic energy, the multiplication as shown in equation (A.1) is written as:

$$\underbrace{\overline{u''_i u''_j\cdot\frac{\partial\rho}{\partial t}}}_{\text{continuity}}+\underbrace{\overline{\rho u''_j\cdot\frac{\partial(\widetilde{u_i}+u''_i)}{\partial t}}}_{\text{momentum}}+\underbrace{\overline{\rho u''_i\cdot\frac{\partial(\widetilde{u_j}+u''_j)}{\partial t}}}_{\text{momentum}}.$$

When the partial derivatives are expended, the terms containing a quantity that is Favre averaged drops to zero as per rule 4. The term remaining are rewritten using rule 5:

$$\overline{u''_i u''_j\cdot\frac{\partial\rho}{\partial t}}+\overline{\rho u''_j\cdot\frac{\partial u''_i}{\partial t}}+\overline{\rho u''_i\cdot\frac{\partial u''_j}{\partial t}}=\overline{\frac{\partial\rho u''_i u''_j}{\partial t}}\,.$$

The advection term starts by writing the terms in the form of equation (A.1), and expanding the terms as per rule 2:

$$\overline{\underbrace{u_i'' u_j'' \frac{\partial \rho(\widetilde{u_k} + u_k'')}{\partial x_k}}_{\text{momentum}} + \underbrace{u_i'' \rho(\widetilde{u_k} + u_k'') \frac{\partial u_j''}{\partial x_k}}_{\text{momentum}} + \underbrace{u_j'' \rho(\widetilde{u_k} + u_k'') \frac{\partial u_i''}{\partial x_k}}_{\text{continuity}}} .$$

Expanding all the terms results in:

$$\begin{aligned}
&\overline{u_i'' u_j'' \frac{\partial \rho(\widetilde{u_k} + u_k'')}{\partial x_k} + u_i'' \rho(\widetilde{u_k} + u_k'') \frac{\partial u_j''}{\partial x_k} + u_j'' \rho(\widetilde{u_k} + u_k'') \frac{\partial u_i''}{\partial x_k}} \\
&= \underbrace{\overline{u_i'' u_j'' \frac{\partial \rho \widetilde{u_k}}{\partial x_k}}}_{1} + \underbrace{\overline{u_i'' u_j'' \frac{\partial u_k'' \rho}{\partial x_k}}}_{2} + + \underbrace{\overline{\rho u_i'' \widetilde{u_k} \frac{\partial u_j''}{\partial x_k}}}_{3} + \dots \\
&\quad \underbrace{\overline{u_i'' \rho u_k'' \frac{\partial \widetilde{u_j}}{\partial x_k}}}_{4} + \underbrace{\overline{u_i'' \rho u_k'' \frac{\partial u_j''}{\partial x_k}}}_{5} + \underbrace{\overline{u_j'' \rho \widetilde{u_k} \frac{\partial u_i''}{\partial x_k}}}_{6} + \dots \\
&\quad \underbrace{\overline{u_j'' \rho u_k'' \frac{\partial \widetilde{u_i''}}{\partial x_k}}}_{7} + \underbrace{\overline{u_j'' \rho u_k'' \frac{\partial u_i''}{\partial x_k}}}_{8} \\
&= \underbrace{\overline{\frac{\partial \rho \widetilde{u_k} u_i'' u_j''}{\partial x_k}}}_{1,3,6} + \underbrace{\overline{\frac{\partial \rho u_k'' u_i'' u_j''}{\partial x_k}}}_{2,5,8} + \underbrace{\overline{\rho u_k'' u_j''} \frac{\widetilde{\partial u_i}}{\partial x_k}}_{4,7} .
\end{aligned} \tag{A.15}$$

During the steps shown in equation (A.15) the terms resulting in 0 due to rule 3 have been left out. The terms 1, 3, and 6 can be combined by rule 4 as can be done for the terms annotated 2, 5, and 8. The term created by combining 1,4, and 7 is the advection part of the material derivative of the budget and together with the temporal component derived previously results in a 0. The two terms from the RHS can be expanded as shown below, with pressure expended as:

$$\begin{aligned}
&\overline{-u_i'' \frac{\partial \left(\overline{p} + p'\right)}{\partial x_j}} \\
&\quad = -\overline{u_i''} \overline{\frac{\partial p}{\partial x_i}} - \overline{\frac{\partial p' u_i''}{\partial x_i}} + \overline{p' \frac{\partial u_i''}{\partial x_i}} .
\end{aligned} \tag{A.16}$$

And viscous stress as:

$$\begin{aligned}
&\overline{u_i'' \frac{\partial \left(\overline{\tau_{ij}} + \tau_{ij}'\right)}{\partial x_j}} \\
&= \overline{u_i''} \overline{\frac{\partial \tau_{ij}}{\partial x_j}} + \overline{\frac{\partial \tau_{ij}' u_i''}{\partial x_j}} - \overline{\tau_{ij}' \frac{\partial u''}{\partial x_j}_i} .
\end{aligned} \tag{A.17}$$

All terms can be collected after which all subscripts $_j$ are written as $_i$, followed by $_k$ to $_j$. Doing so give the budget for turbulent kinetic energy:

$$\underbrace{-\overline{\rho u_j'' u_i''} \frac{\widetilde{\partial u_i}}{\partial x_j}}_{\mathcal{P}} - \underbrace{\overline{\frac{\partial \frac{1}{2} \rho u_j'' u_i'' u_i''}{\partial x_j}}}_{\mathcal{T}_t} - \underbrace{\overline{\frac{\partial u_i'' p'}{\partial x_i}}}_{\mathcal{T}_p} + \underbrace{\overline{\frac{\partial u_i'' \tau_{ij}'}{\partial x_j}}}_{\mathcal{T}_v} + \underbrace{\overline{u_i''} \overline{\frac{\partial p}{\partial x_i}}}_{\mathcal{C}_{k1}} + \underbrace{\overline{u_i''} \overline{\frac{\partial \tau_{ij}}{\partial x_j}}}_{\mathcal{C}_{k2}} + \underbrace{\overline{p' \frac{\partial u_k''}{\partial x_k}}}_{\mathcal{C}_{k3}} - \underbrace{\overline{\tau_{ij}' \frac{\partial u_i''}{\partial x_j}}}_{\mathcal{D}} = 0 . \tag{A.18}$$

The individual terms in equation (A.18) denote:

- $\mathcal{P}$, production.
- $\mathcal{T}_t$, turbulent transport.
- $\mathcal{T}_p$, pressure transport.
- $\mathcal{T}_v$, viscous transport.
- $\mathcal{C}_{k1}$, pressure mass transport.
- $\mathcal{C}_{k2}$, viscous mass transport.
- $\mathcal{C}_{k3}$, pressure-velocity coupling.
- $\mathcal{D}$, dissipation.

Bibliography

[1] Bendiks Jan Boersma. A 6th order staggered compact finite difference method for the incompressible Navier-Stokes and scalar transport equations. Journal of Computational Physics, 230 (12):4940–4954, 2011. ISSN 10902716. doi: 10.1016/j.jcp.2011.03.014. URL http://dx.doi.org/10.1016/j.jcp.2011.03.014.

[2] P. J. Coelho. Numerical simulation of the interaction between turbulence and radiation in reactive flows. Progress in Energy and Combustion Science, 33(4):311–383, 2007. ISSN 03601285. doi: 10.1016/j.pecs.2006.11.002.

[3] Pedro J. Coelho. Turbulence-radiation interaction: From theory to application in numerical simulations. 2010 14th International Heat Transfer Conference, IHTC 14, 8(March):251–270, 2010. doi: 10.1115/IHTC14-23339.

[4] G.N. Coleman, J. Kim, and R. D. Moser. A numerical study of turbulent supersonic isothermal-wall channel flow. Journal of Fluid Mechanics, 305:159–183, 1995. ISSN 14697645. doi: 10.1017/S0022112095004587.

[5] Daniel Deshmukh, Kshitij and Modest, Michael and Haworth. Higher-order spherical harmonics to model radiation in direct numerical simulation of turbulent reacting flows. An International Journal of Computational Thermal Sciences, 1, 2009. doi: 10.1615/ComputThermalScien.v1.i2.60.

[6] H. Foysi, S. Sarkar, and R. Friedrich. Compressibility effects and turbulence scalings in supersonic channel flow. Journal of Fluid Mechanics, 509(509):207–216, 2004. ISSN 00221120. doi: 10.1017/S0022112004009371.

[7] S. Ghosh, R. Friedrich, M. Pfitzner, Chr Stemmer, B. Cuenot, and M. El Hafi. Effects of radiative heat transfer on the structure of turbulent supersonic channel flow. Journal of Fluid Mechanics, 677:417–444, 2011. ISSN 00221120. doi: 10.1017/jfm.2011.92.

[8] John R. Howell, M. Pinar Mengüç, and Robert Siegel. Thermal radiation heat transfer, sixth edition. CRC press, 2015. ISBN 9781498757744.

[9] John R. Howell, M. Pinar Mengüç, and Robert Siegel. Thermal Radiation Heat Transfer. CRC press, 6th edition, 2016. ISBN 978-1-4665-9326-8.

[10] P.G. Huang, G.N. Coleman, and P. Bradshaw. Compressible turbulent channel flows: DNS results and modelling. Journal of Fluid Mechanics, 305:185–218, 1995. doi: https://doi.org/10.1017/S0022112095004599J.

[11] Christopher A. Kennedy and Andrea Gruber. Reduced aliasing formulations of the convective terms within the Navier-Stokes equations for a compressible fluid. Journal of Computational Physics, 227(3):1676–1700, 2008. ISSN 10902716. doi: 10.1016/j.jcp.2007.09.020.

[12] John Kim, Parviz Moin, and Robert Moser. Turbulence statistics in fully developed channel flow at low reynolds number. Journal of Fluid Mechanics, 177:133–166, 1987. ISSN 14697645. doi: 10.1017/S0022112087000892.

[13] S. Lele. Compressibility Effects on Turbulence. Annual Review of Fluid Mechanics, 26(1):211–254, 1994. ISSN 00664189. doi: 10.1146/annurev.fluid.26.1.211.

[14] Sanjiva K. Lele. Compact finite difference schemes with spectral-like resolution. Journal of Computational Physics, 103(1):16–42, 1992. ISSN 10902716. doi: 10.1016/0021-9991(92)90324-R.

[15] Y. Morinishi, S. Tamano, and K. Nakabayashi. Direct numerical simulation of compressible turbulent channel flow between adiabatic and isothermal walls, volume 502. 2004. ISBN 0022112003007. doi: 10.1017/S0022112003007705.

[16] F. Nicoud. Conservative High-Order Finite-Difference Schemes for Low-Mach Number Flows. Journal of Computational Physics, 158(1):71–97, 2000. ISSN 00219991. doi: 10.1006/jcph.1999.6408.

[17] Frans T.M. Nieuwstadt, Bendiks J. Boersma, and Jerry Westerweel. Turbulence: Introduction to theory and applications of turbulent flows. 2016. ISBN 9783319315997. doi: 10.1007/978-3-319-31599-7.

[18] Sergio Pirozzoli. Generalized conservative approximations of split convective derivative operators. Journal of Computational Physics, 229(19):7180–7190, 2010. ISSN 10902716. doi: 10.1016/j.jcp.2010.06.006. URL http://dx.doi.org/10.1016/j.jcp.2010.06.006.

[19] Stephen B. Pope. Turbulent Flows. Cambridge University print, 2000. ISBN 9780521598866. doi: 10.1201/9780203750384-13.

[20] Stephen K. Robinson. Coherent motions in the turbulent boundary layer. Annual Review of Fluid Mechanics, 23(1):601–639, 1991. ISSN 00664189. doi: 10.1146/annurev.fl.23.010191.003125.

[21] Atsushi Sakurai, Tae Ho Song, Shigenao Maruyama, and Hyun Keol Kim. Comparison of radiation element method and discrete ordinates interpolation method applied to three-dimensional radiative heat transfer. JSME International Journal, Series B: Fluids and Thermal Engineering, 48(2):259–264, 2005. ISSN 13408054. doi: 10.1299/jsmeb.48.259.

[22] Atsushi Sakurai, Koji Matsubara, Kenji Takakuwa, and Ryo Kanbayashi. Radiation effects on mixed turbulent natural and forced convection in a horizontal channel using direct numerical simulation. International Journal of Heat and Mass Transfer, 55(9-10):2539–2548, 2012. ISSN 00179310. doi: 10.1016/j.ijheatmasstransfer.2012.01.006. URL http://dx.doi.org/10.1016/j.ijheatmasstransfer.2012.01.006.

[23] Uttiya Sengupta. Fully compressible Direct Numerical Simulations of carbon dioxide close to the vapour-liquid critical point. PhD thesis, TU Delft, 2019.

[24] S. Silvestri. Turbulence radiation interactions in fully developed channel flow. PhD thesis, Delft University of Technology, 2016.

[25] S. Silvestri and R Pecnik. A fast GPU Monte Carlo radiative heat transfer implementation for coupling with direct numerical simulation. Journal of Computational Physics: X, 3, 2019. ISSN 25900552. doi: 10.1016/j.jcpx.2019.100032.

[26] S. Silvestri, A. Patel, D. J.E.M. Roekaerts, and R. Pecnik. Turbulence radiation interaction in channel flow with various optical depths. Journal of Fluid Mechanics, 834:359–384, 2018. ISSN 14697645. doi: 10.1017/jfm.2017.738.

[27] S. Silvestri, D. J.E.M. Roekaerts, and R. Pecnik. Assessing turbulence-radiation interactions in turbulent flows of non-gray media. Journal of Quantitative Spectroscopy and Radiative Transfer, 233:134–148, 2019. ISSN 00224073. doi: 10.1016/j.jqsrt.2019.05.018. URL https://doi.org/10.1016/j.jqsrt.2019.05.018.

[28] Lionel Tessé, Francis Dupoirieux, and Jean Taine. Monte Carlo modeling of radiative transfer in a turbulent sooty flame. International Journal of Heat and Mass Transfer, 47(3):555–572, 2004. ISSN 00179310. doi: 10.1016/j.ijheatmasstransfer.2003.06.003.

[29] V. Vesovic, W. A. Wakeham, G. A. Olchowy, J. V. Sengers, J. T. R. Watson, J. Millat, and ARTICLES. The transport properties of carbon dioxide. Journal of Physical and Chemical Reference Data 19 (3), pages 763–808, 1990. doi: https://doi.org/10.1063/1.555875.

[30] R. Vicquelin, Y. F. Zhang, O. Gicquel, and J. Taine. Effects of radiation in turbulent channel flow: Analysis of coupled direct numerical simulations. Journal of Fluid Mechanics, 753(4):360–401, 2014. ISSN 14697645. doi: 10.1017/jfm.2014.368.

[31] Y. Wu, D. C. Haworth, M. F. Modest, and B. Cuenot. Direct numerical simulation of turbulence/radiation interaction in premixed combustion systems. Proceedings of the Combustion Institute, 30(1):639–646, 2005. ISSN 15407489. doi: 10.1016/j.proci.2004.08.138.

[32] Y. F. Zhang, R. Vicquelin, O. Gicquel, and J. Taine. Physical study of radiation effects on the boundary layer structure in a turbulent channel flow. International Journal of Heat and Mass Transfer, 61(1):654–666, 2013. ISSN 00179310. doi: 10.1016/j.ijheatmasstransfer.2013.02.041. URL http://dx.doi.org/10.1016/j.ijheatmasstransfer.2013.02.041.